2D Soft Robotics Modeling for Small Body Environments and Granular Electroadhesion Characterization

by

Jesse Tambornini

B.S., California Polytechnic State University, 2017

A thesis submitted to the

Faculty of the Graduate School of the

University of Colorado in partial fulfillment

of the requirements for the degree of

Master of Science

Department of Aerospace Engineering

2020

This thesis entitled:
2D Soft Robotics Modeling for Small Body Environments and Granular Electroadhesion Characterization
written by Jesse Tambornini
has been approved for the Department of Aerospace Engineering

Prof. Jay McMahon

Prof. Hanspeter Schaub

Prof. Christoph Keplinger

Date

The final copy of this thesis has been examined by the signatories, and we find that both the content and the form meet acceptable presentation standards of scholarly work in the above mentioned discipline.

Tambornini, Jesse (M.S., Aerospace Engineering Sciences)

2D Soft Robotics Modeling for Small Body Environments and Granular Electroadhesion Characterization

Thesis directed by Prof. Jay McMahon

Near Earth Asteroids provide an interesting and unique promise for scientific understanding and resource utilization, while also providing some of the greatest danger of serious planetary impact. One potential mission architecture, utilizing a digging hub and soft elastomer limbs for locomotion and adhesion, could provide solutions to all these opportunities and problems. One current obstacle in the design of this concept is the lack of characterization and understanding of the interactions between the lander robot and the asteroid surface. This interaction takes two forms: the contact between the robot structure and the asteroid surface, and any passive or active adhesion forces attracting the robot to the surface. This thesis examines these interactions through the creation of rigid link approximation models for a single arm of the robot, as well as a planar approximation for the full robot moment in a single direction along the ground. This is accomplished with simulations of the interactions between the robot and the surface, along with other external forces. In examining attractions to the surface, active attraction in the form of electroadhesion is selected as the primary focus. The preliminary stages of granular electroadhesion are thus characterized, with the construction of a test fixture, development of a test procedure, and some data taken for a variety of materials, including four granular ones. With these two contributions, this work should help advance the progress of soft robotic modeling, granular electroadhesion, and the soft robotic lander mission concept.

Acknowledgements

First and foremost, I would like to thank Dr. Jay McMahon, both for taking me into the ORCCA lab as one of his students and helping walk me through this research for the past two years. Your thoughtful approach to advising and leadership are something I hope to be able to emulate going into the future. To all the other members of the ORCCA lab, thank you for being such a great group of people to work with inside the lab and have fun outside of it. Special thanks to Don, who got me started on this line of research a semester into my degree when I knew even less than I do now. For my committee, I wanted to let you know how much I have appreciapted your patience as we've taken the long road to this defense. Finally, thank you to my friends and family for supporting me through these last two years, and putting up with an unreasonable amount of space robot related conversations.

Contents

Chapter

Tables

Table

Figures

Figure

Chapter 1

Background and Motivation

1.1 Introduction

Near Earth Asteroids, or NEAs, pose both danger and opportunity. As some of our nearest planetary neighbors, they can provide clues as to the formation of Earth and the rest of the solar system. This proximity also provides an opportunity for asteroid mining, since these asteroids could provide easy to reach refueling stations for spacecraft leaving the planet. In addition to the potential of NEAs for science and In situ resource utilization (ISRU) missions, these asteroids also are some of the biggest risks for planetary impact. With the goal of solving these challenges, the Area of Effect Softbot (AoES) was proposed by Dr. McMahon [20]. In this solution, a number of smaller soft robots, the AoES, are deployed to an asteroid surface, while a mothership orbits a safe distance from the surface. The defining feature of these robots is the large elastomer arms, which provide anchoring to the asteroid and a propulsion to the surface, acting as a solar sail. For this class of asteroids, soft robotics provides a unique solution to some of the main challenges of working on an rubble pile asteroid, which are landing on an uncertain, rough environment, and sticking to the surface once there. With many near earth asteroids possessing small gravitational attraction and high spin rates, the effective gravity at the surface can sometimes even be negative [2].

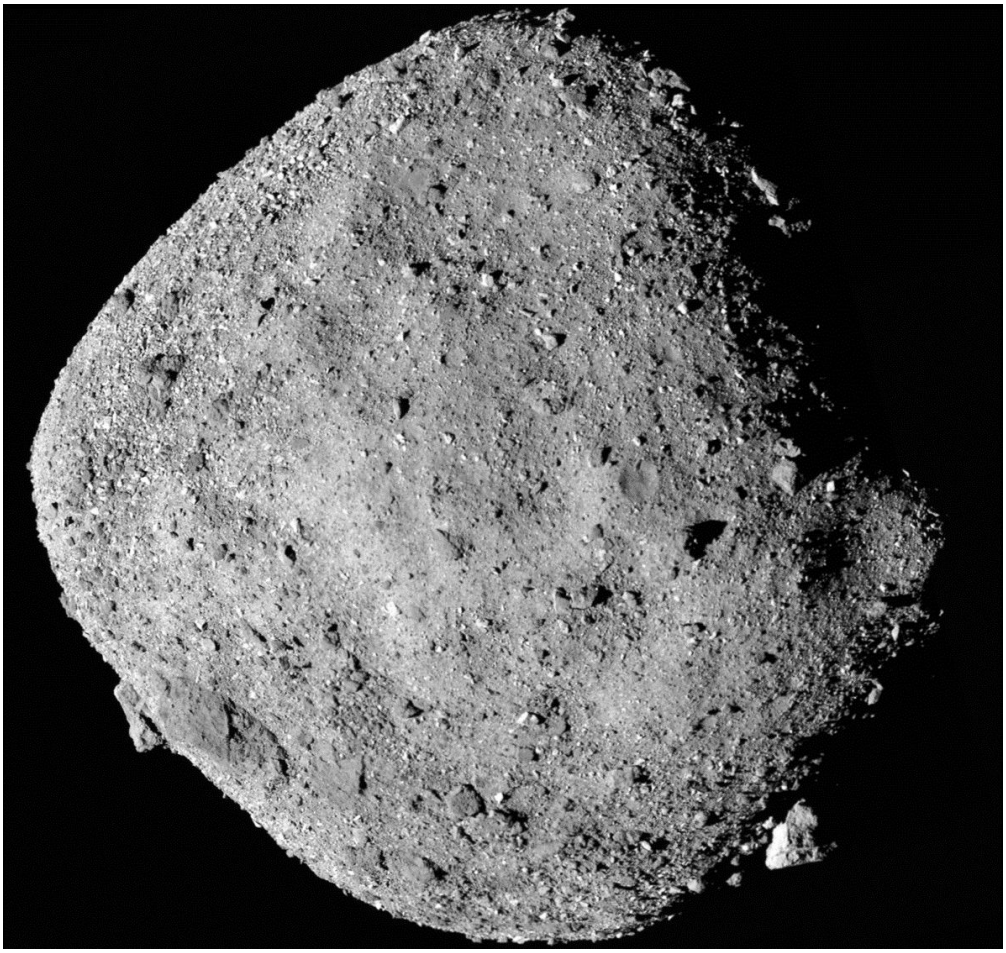

Figure 1.1: Images of the surface of the rubble pile asteroid 101955 Bennu, as taken by the OSIRIS-REx mission. The rough surface will add difficulty to future missions on the surface.

However, since the asteroids remain together, some other force must be holding the asteroid together, and the most likely candidate is internal cohesion. Using a large surface area of a soft material, the AoES can anchor itself with adhesive forces to maneuver around the asteroid and dig. Additionally, the large surface area can be used to leverage solar radiation pressure (SRP) to maneuver down to the surface and land, eliminating the need for other on-board propulsion. Beyond the mission risk advantages of using the AoES mission architecture, this novel concept lends itself well to novel science objectives, as most state of the art spacecraft cannot sample an asteroid subsurface, while the AoES could dig arbitrarily deep if regolith conditions allow. For planetary protection, a team of AoES on the surface could loft material to change the orbit of the

body, as investigated by D. Brack [2]. Given the potential benefits of an AoES mission to NEAs, it is worth building a model to evaluate the surface operations viability of the concept, especially since there area number of challenges associated with using soft robotics in a space environment. Thankfully, some of these challenges are addressed by the use of HASEL actuators, developed by Acome et al [1] in the Keplinger Research Group (KRG). These electronically controlled soft actuators are self contained and contain no air, meaning it does not expand like pneumatic soft robots, nor does it need an external pump or motor, which add significant weight and cost to a space mission. These actuators work by charging flexible electrodes on opposite sides of a dielectric fluid filled bag, which by compressing the bag, change the shape of the bag, creating some displacement and exerting some force. The type of force and displacement depends on the shape of the dielectric fluid bag and electrodes.

A number of works have analyzed various other aspects of a potential AoES mission, including the solar radiation pressure based landing control by Oguri and McMahon [21], and the digging mechanics of the hub by a CU Boulder graduate projects team. This leaves a gap, however, in any modeling of the AoES after it has landed but before it begins digging. The motivation for this project is to develop an effective method of analyzing the behavior of the AoES as it interacts with the surface of an asteroid. This will allow the viability of an AoES mission to be established, especially since a number of challenges still need to be addressed.

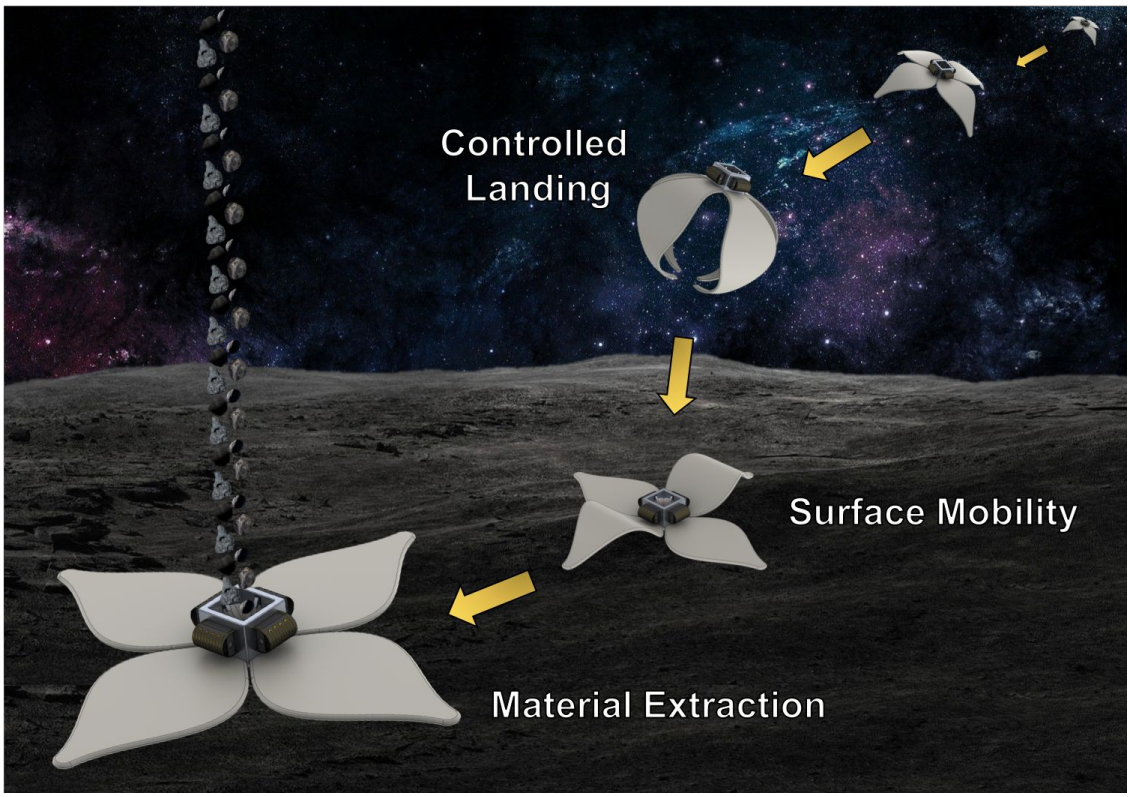

Figure 1.2: Concept of operations for the AoES. The focus of this thesis is largely on the surface mobility aspect, which has yet to be investigated. Image credit to McMahon et al, [20]

One challenge of using soft robotics in this context is the extreme flexibility while maneuvering to the asteroid. Since a very high area to mass ratio is critical for the effective use of SRP forces in propulsion, the thickness of these arms is on the order of a few centimeters for a 1 meter arm. Movement of the hub relative to the arms will primarily happen during landing, when the AoES is changing its attitude to get the desired magnitude and direction of SRP forces. Since the arms will still be very flexible in bending, rapid changes in attitude could lead to large vibrations in the arms, and adverse performance if this was unexpected by the controller. Additionally, it is unknown what combination of parameters of a limb will be required for the AoES to be able to crawl on the surface, including potential active adhesion. Since limb thickness, length, shape, and material are all potential variables, an ideal model will be able to vary all those parameters while remaining computationally efficient. Furthermore, the model should be able to predict how the passive effects

of the softness of the limb will affect controllability, both on the surface and traveling to it. Finally, experimental verification and characterization of the limb and active adhesion methods would need to be performed to ensure that the model accurately represents a true interaction between the AoES and the asteroid surface.

1.2 Soft Robotic Modeling

Soft robots, as discussed above, refer to any robot design which leverages the compliant nature of the materials in its construction for the its movement or material handling. While a number of works have examined soft robotic modeling, this problem poses some unique challenges not directly addressed by previous work. Analyzing soft structures is typically challenging, as many traditional structural analysis software is designed primarily for rigid structures, and may have assumptions made for speed which make large displacement results inaccurate. Additionally, many are not designed to simulate the same time-variant forces found in soft robotics, since most dynamic analysis of rigid structures is in the form of vibration tests, which are fundamentally different than applying control to a soft structure. Some soft robots even utilize a combination of rigid and soft elements [7], potentially further complicating the results. Some work has been done in the creating soft robot specific modeling tools, including a multi-limb modeling by Huang et al [17], and a reduced-order cable actuated limb modeling method by Chenevier et al [5], both of which provide computationally efficient hyper-elastic models. However, both of these models have limitation in the implementation: the Huang model assumes slender limbs and the Chenevier model is restricted to pull-cable control. One of the most general models built available, which can analyze arbitrary structures with variable external or control forces by Faure et al [9], Largilliere et al [18], and Duriez [8], whose work has culminated in the SOFA modeling toolkit. While this model is useful in a variety of situations, its computational cost and general complexity of implementation mean it could be less than ideal for the initial design of a soft robot and its control algorithms. For this preliminary ideation phase, a computationally faster model would be ideal, and, particularly for the AoES, one that was built with the particular forces relevant to the NEA environment.

1.3 Granular Electroadhesion

Electroadhesion, a potential source of active adhesion to the asteroid surface mentioned above, is an active form of electrostatic attraction which, through interdigitated electrodes, selectively polarizes a surface, as seen in figure 1.3. The driving mechanism for this phenomenon has been established to be the interaction of the fringe field between the oppositely charged electrodes interacting with natural or induced dipoles in non-conductive materials, or directly with electrons for conductive ones, to create electrostatic attraction. This effect needs high voltage in order to be effective in many materials, especially non-conductive ones.

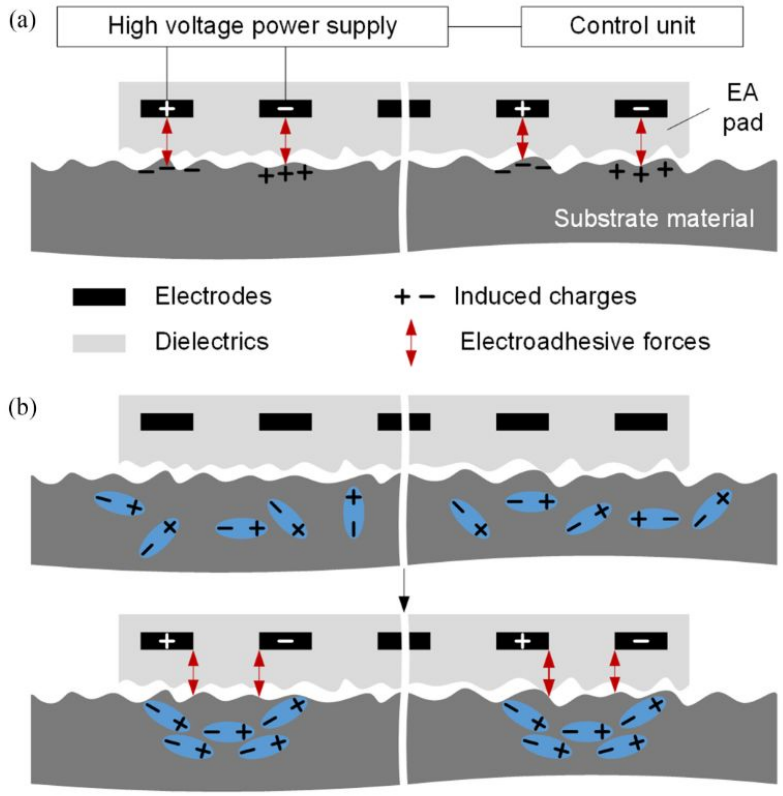

Figure 1.3: Illustration of the mechanism behind the attraction of electroadhesion. For the conductive materials shown in (a), the electron movement is the driving factor, while for non-conductive ones shown in (b), dipole realignment is the driving factor. "+" denotes positive voltage while "-" denotes negative or ground. Image credit to Guo et al, [16]

Electroadhesion is a growing field with a variety of new bodies of work, many of which are outlined and summarized by Guo et al [16]. In that work, the authors also outline the unanswered questions within the field, of which a primary one is the examination of granular electroadhesion, either in terms of theoretical modeling or experimental verification. While works by Guo et al [15] and Téllez et al [23] have tested electroadhesion on a variety of materials, including followup work by Guo et al on the optimization of pad width and spacing for conductive and non-conductive materials [14], all these materials tested are relatively flat, even if a few, like the concrete tested by Tellez, are somewhat rough. Even many works which examine practical uses of electroadhesion in grippers, like Cacuccio [4], and Shintake [22], examine the use of these devices on a variety of shapes, but none shown are rough or porous like some common natural materials such as tree bark or volcanic rock. Additionally, work done to produce crawling robots, like the soft robot of Gu [13], or the more traditional designs found in Wang [24] and de Rivaz [7], is tailored for human environments with many flat surfaces, but may not be able to perform well in natural environments, or the rocky ones found on rubble-pile asteroids. Even the work done by Germann [12], where the authors constructed and characterized a flexible electroadhesive pad, only looked at the interaction of the pad with flat test substrates. Given that rough, porous, and granular materials are common outside man-made environments, if electroadhesion is to be useful beyond these, techniques to characterize and specialize electroadhesion for these situations is required. This is especially pertinent on asteroids, where only estimations of the surface texture and type are possible before reaching the asteroid for the first time with a spacecraft, so electroadhesive pads which are robust to many types of surface environment would be needed to guarantee functionality. This work begins to examine electroadhesion on rough and granular materials to begin to fill this gap in knowledge for this field.

1.4 Thesis contributions

Given the gaps in low-level soft robotics modeling and granular electroadhesion, both of which are critical to developing the next stage of the AoES mission, this work seeks to help further

the understanding of these areas as well as provide practical solutions for the furtherance of the development of the AoES mission concept. This is done by creating two rigid link approximation models, one for the AoES limb alone and one for the a planar approximation of the AoES, as well as develop a test procedure for granular electroadhesion and begin to characterize granular materials.

The models demonstrated by this work begin to accomplish these goals, as will be shown, though more work needs to be done before an AoES mission can be considered ready to fly. Through the creation of a variable-accuracy model with the ability to discritize arbitrary limb shapes, this model supports the exploration of the design space for the AoES. Additionally, a test fixture and procedure are developed for testing electroadhesive attraction on granular media, and some preliminary data is presented for granular and non-granular test substrates.

Chapter 2

Limb Dynamics Model

2.1 Derivation

2.1.1 Unforced Dynamics

To model this system, the flexible arm is approximated as a series of rigid links, connected with a pin joint. At each pin, a torsional spring and damper account for material effects, while the mass and mass location of each link depend on the mass location depends on the limb shape at that link. These assumptions create a simplified, planar case for the limb simulation, which is what will be examined in this work. This model uses a trapezoidal approximation of each link, using the link width at each end of the link. An example of this can be seen in the figure 2.1.

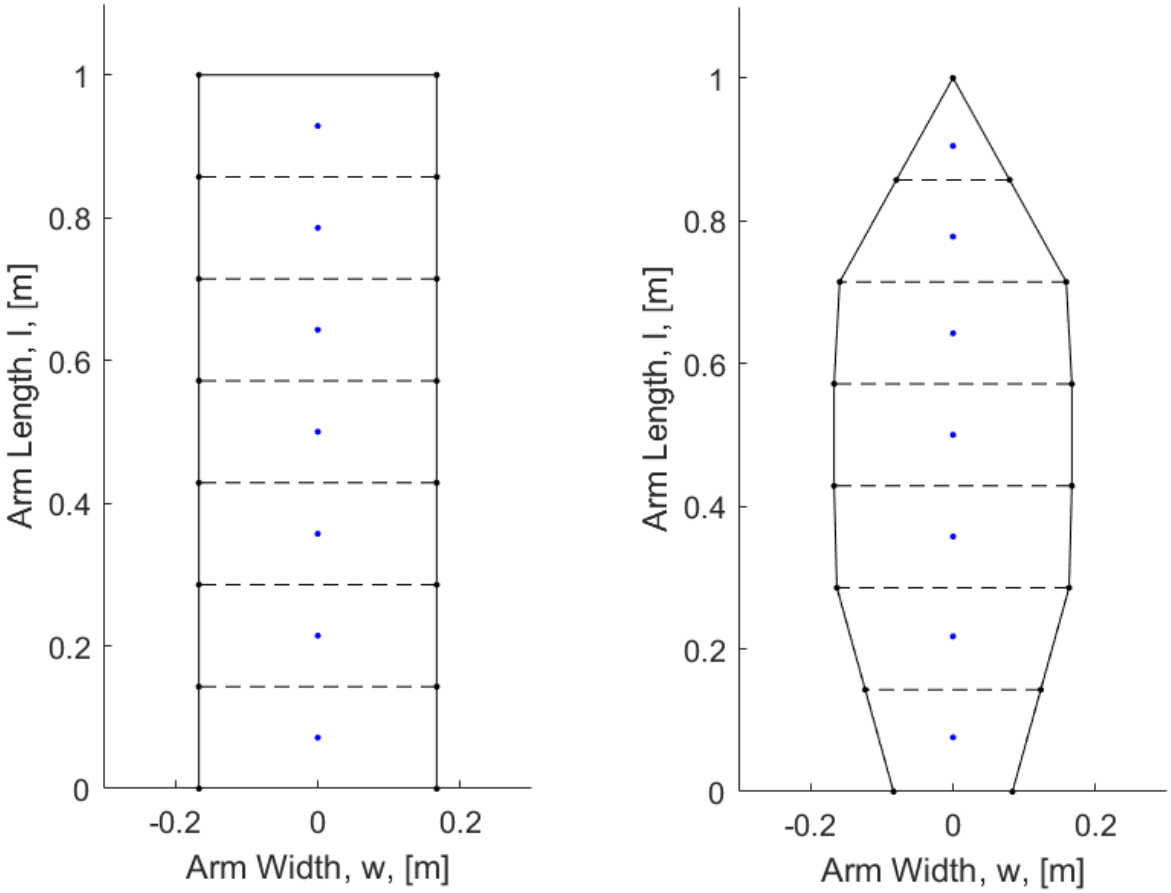

Figure 2.1: Examples of a seven section limb discretization for both the rectangular limb on the left and a piece-wise diamond-shaped one on the right. Black dots are the points which form the vertices of the trapezoids, and blue ones are the centroids of the trapezoidal elements. Solid lines show the outside of the limb, with the dashed lines completing the individual link trapezoids.

To solve these equations for a variety of initial conditions and external forces, a numerical integration approach is used, allowing for the easy inclusion of external forces and control. The equations of motion for this simplified, planar limb are derived using a Lagrangian approach,

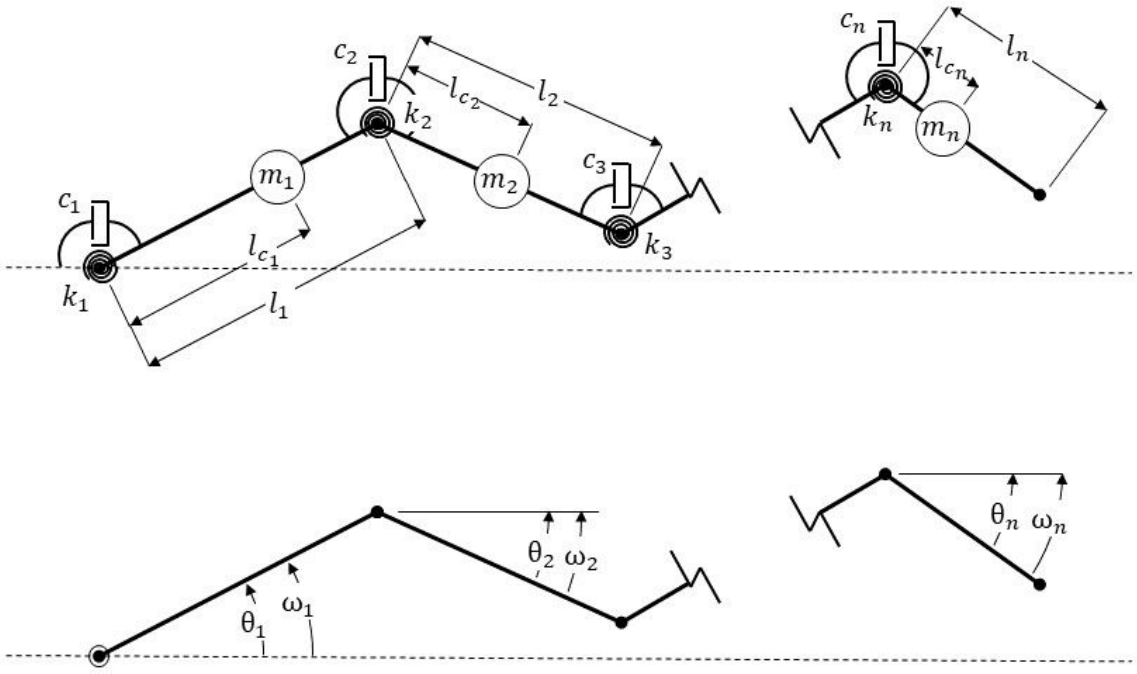

Figure 2.2: Diagram illustrating the model parameters (top), and model states (bottom) for the limb-only model. In the upper plot l_i is the link length, $l_{c,i}$ is the position of the mass along the link, m_i indicates the link masses, k_i is the joint torsional stiffness, and c_i is the angular damping. The lower plot shows the generalized coordinates, θ_i, and corresponding coordinate rates $\dot{\theta}_i$, with arrows corresponding to the positive direction of the angle, regardless of the sign of the angle depicted. In this case, all angles and rates are defined as positive for a right-handed rotation about an out of the page axis.

outlined below.

$$T = \sum_{i=1}^{n} \frac{1}{2} m_i v_i^2 + \frac{1}{2} I_i \dot{\theta}_i^2 \tag{2.1}$$

$$V = \sum_{i=1}^{n} \frac{1}{2} k_i (\theta_i - \theta_{i-1})^2 \tag{2.2}$$

For the above equations, m_i is the mass of link i, v_i is the velocity of that mass, I_i is the moment of inertia about the center of mass of that link, and $\dot{\theta}_i$ is the angular velocity of each link, relative to the inertial frame. For the potential energy, k_i is the spring rate of the spring at the base of link i, and θ_i is the angle of each link relative to the horizontal. θ_0 is zero. For the generalized coordinates, the absolute link angles were selected, such that $q_i = \theta_i$, and $\dot{q}_i = \dot{\theta}_i$. In addition to the kinetic and potential energies, a damping function, D, is defined to account for energy losses resulting from the bending at the joints. This derivation assumes linear angular damping, proportional to the relative rate at each joint. For this type of system, the damping function would be as follows

$$D = \sum_{i=1}^{n} \frac{1}{2} c_i (\dot{\theta}_i + \dot{\theta}_{i-1})^2 \tag{2.3}$$

In this equation, c_i is the damping constant at the i^{th} joint. Similar to the potential energy equation, $\dot{\theta}_0$ is assumed to be always zero. Finding the equations of motion requires taking various partials with respect to the energies, as defined in equation 2.4.

$$-\frac{\mathrm{d}}{\mathrm{d}t}\frac{\partial T}{\partial \dot{q}_s} + \frac{\partial T}{\partial q_s} - \frac{\partial V}{\partial q_s} - \frac{\partial D}{\partial \dot{q}_s} = -Q_s \tag{2.4}$$

This derivation will start with the partials with respect to V, since they are among the easiest to evaluate. For the potential energy, only spring forces are initially considered. Assuming each joint has a known, constant spring rate at its base, k_i, and assuming $\theta_0 = 0$, $k_{n+1} = 0$ and take the partial with respect to θ_s,

$$\frac{\partial V}{\partial \theta_s} = k_s\theta_s - k_s\theta_{s-1} + k_{s+1}\theta_s - k_{s+1}\theta_{s+1}$$

We can thus represent the full partial of the potential energy with respect to all the generalized coordinates as the matrix equation

$$\frac{\partial V}{\partial \mathbf{q}} = K\mathbf{q}$$

Where the stiffness matrix, K, is defined below

$$K = \begin{bmatrix} k_1 + k_2 & -k_2 & 0 & ... & 0 \\ -k_2 & k_2 + k_3 & -k_3 & ... & 0 \\ \vdots & \vdots & \ddots & & \vdots \\ 0 & 0 & ... & k_{n-1} + k_n & -k_n \\ 0 & 0 & ... & -k_n & k_n \end{bmatrix} \tag{2.5}$$

To include damping, the approach is similar to the potential energy. Assuming each joint has a known, constant damping coefficient at its base joint, c_i, the damping function can be constructed

$$D = \frac{1}{2} \sum_{i=1}^{n} c_i (\dot{q}_i - \dot{q}_{i-1})^2$$

Assuming $\dot{q}_0 = 0$, $c_{n+1} = 0$ and take the partial with respect to $\dot{q}_s$, obtaining

$$\frac{\partial D}{\partial \dot{q}_s} = c_s \dot{q}_s - c_s \dot{q}_{s-1} + c_{s+1} \dot{q}_s - c_{s+1} \dot{q}_{s+1}$$

With a similar matrix equation definition as with the stiffness matrix above,

$$\frac{\partial V}{\partial \dot{\mathbf{q}}} = C_D \dot{\mathbf{q}}$$

With the definition of the the damping matrix, C_D, as

$$C_D = \begin{bmatrix} c_1 + c_2 & -c_2 & 0 & ... & 0 \\ -c_2 & c_2 + c_3 & -c_3 & ... & 0 \\ \vdots & \vdots & \ddots & & \vdots \\ 0 & 0 & ... & c_{n-1} + c_n & -c_n \\ 0 & 0 & ... & -c_n & c_n \end{bmatrix} \tag{2.6}$$

Now with the potential energy and damping function partials out of the way, Moving on to the kinetic energy partials. The definition of the velocity of the mass on the i^{th} limb is defined below:

$$\boldsymbol{v_i} = -\Big(l_{c_i} \dot{\theta}_i \sin(\theta_i) + \sum_{j=1}^{i-1} l_j \dot{\theta}_j \sin(\theta_j)\Big)\hat{\imath} + \Big(l_{c_i} \dot{\theta}_i \cos(\theta_i) + \sum_{j=1}^{i-1} l_j \dot{\theta}_j \cos(\theta_j)\Big)\hat{\jmath} \tag{2.7}$$

With the velocity of each mass defined in terms of the generalized coordinates, beginning with the partials relative to the generalized rates.

$$\frac{\partial T}{\partial \dot{\theta}_s} = \sum_{i=1}^{n} m_i \mathbf{v}_i \cdot \frac{\partial \mathbf{v}_i}{\partial \dot{\theta}_s} + I_i \dot{\theta}_i \frac{\partial \dot{\theta}_i}{\partial \dot{\theta}_s}$$

For the angular rates, this partial is easy, with a result of zero unless $i = s$, in which case the result is one. For the velocities, the result can be one of three cases, outlined below

$$\frac{\partial \mathbf{v}_i}{\partial \dot{\theta}_s} = \begin{cases} 0 & s > i \\ -l_{c_s} \sin(\theta_s)\hat{\imath} + l_{c_s} \cos(\theta_s)\hat{\jmath} & s = i \\ -l_s \sin(\theta_s)\hat{\imath} + l_s \cos(\theta_s)\hat{\jmath} & s < i \end{cases} \tag{2.8}$$

Plugging this in and evaluating the dot product between the velocity and velocity partial gives the equation below,

$$\begin{aligned} \frac{\partial T}{\partial \dot{\theta}_s} &= I_i \dot{\theta}_s + m_s \mathbf{v}_s \big(- l_{c_s} \sin(\theta_s)\hat{\imath} + l_{c_s} \cos(\theta_s)\hat{\jmath} \big) + \sum_{i=s+1}^{n} m_i \mathbf{v}_i \cdot \big(- l_s \sin(\theta_s)\hat{\imath} + l_s \cos(\theta_s)\hat{\jmath} \big) \\ &= I_i \dot{\theta}_s + m_s \Big(l_{c_s}^2 \dot{\theta}_s + l_{c_s} \sum_{i=1}^{s-1} [l_i \cos(\theta_i - \theta_s)\dot{\theta}_i] \Big) \\ &\quad + l_s \sum_{i=s+1}^{n} \Big[m_i \big(l_{c_i} \cos(\theta_i - \theta_s)\dot{\theta}_i + \sum_{j=1}^{i-1} [l_j \cos(\theta_j - \theta_s)\dot{\theta}_j] \big) \Big] \\ &= I_i \dot{\theta}_s + m_s l_{c_s}^2 \dot{\theta}_s + \Big(l_{c_s} m_s + l_s \sum_{i=s+1}^{n} [m_i] \Big) \sum_{i=1}^{s-1} [l_i \cos(\theta_i - \theta_s)\dot{\theta}_i] \\ &\quad + l_s \sum_{i=s+1}^{n} \Big[\big(l_{c_i} m_i + l_i \sum_{j=i+1}^{n} [m_j] \big) \cos(\theta_i - \theta_s)\dot{\theta}_i \Big] \end{aligned}$$

Now, evaluating the time derivative on this term, obtaining

$$\begin{aligned} \frac{\mathrm{d}}{\mathrm{d}t} \frac{\partial T}{\partial \dot{\theta}_s} = (I_s + m_s l_{c_s}^2)\ddot{\theta}_s &+ \Big(l_{c_s} m_s + l_s \sum_{i=s+1}^{n} [m_i] \Big) \sum_{i=1}^{s-1} [l_i \cos(\theta_i - \theta_s)\ddot{\theta}_i] \\ &+ l_s \sum_{i=s+1}^{n} \Big[\big(l_{c_i} m_i + l_i \sum_{j=i+1}^{n} [m_j] \big) \cos(\theta_i - \theta_s)\ddot{\theta}_i \Big] \\ &- \Big(l_{c_s} m_s + l_s \sum_{i=s+1}^{n} [m_i] \Big) \sum_{i=1}^{s-1} [l_i \sin(\theta_i - \theta_s)(\dot{\theta}_i - \dot{\theta}_s)\dot{\theta}_i] \\ &- l_s \sum_{i=s+1}^{n} \Big[\big(l_{c_i} m_i + l_i \sum_{j=i+1}^{n} [m_j] \big) \sin(\theta_i - \theta_s)(\dot{\theta}_i - \dot{\theta}_s)\dot{\theta}_i \Big] \end{aligned} \tag{2.9}$$

In the above equation, there are terms proportional to angular accelerations, which will form the mass matrix, M and terms which are proportional to angular rates, which will form a damping-like rate matrix, $C_{m,1}$ to form a matrix equation for this partial, like with stiffness and true damping. $C_{m,1}$ is referred to as damping like because while it contains elements proportional to the generalized rates, it does not extract energy from the system.

$$\frac{\mathrm{d}}{\mathrm{d}t}\frac{\partial T}{\partial \dot{\theta}_s} = M\ddot{\mathbf{q}} + C_{m,1}\dot{\mathbf{q}} \tag{2.10}$$

Like before, the terms above are written into matrices, given the regular pattern or terms which, in addition to the variable number of links, lends itself to this format. For the system mass matrix, the coefficient $a_i = \left(l_{c_i} m_i + l_i \sum_{j=i+1}^{n} [m_j]\right)$ is used to make the matrix fit on the page.

$$M = \begin{bmatrix} (I_1 + m_1 l_{c_1}^2) & a_2 l_1 \cos(\theta_2 - \theta_1) & ... & a_n l_1 \cos(\theta_n - \theta_1) \\ a_2 l_1 \cos(\theta_2 - \theta_1) & (I_2 + m_2 l_{c_2}^2) & ... & a_n l_2 \cos(\theta_n - \theta_2) \\ \vdots & \vdots & \ddots & \vdots \\ a_{n-1} l_1 \cos(\theta_{n-1} - \theta_1) & a_{n-1} l_2 \cos(\theta_{n-1} - \theta_2) & ... & a_n l_{n-1} \cos(\theta_n - \theta_{n-1}) \\ a_n l_1 \cos(\theta_n - \theta_1) & a_n l_2 \cos(\theta_n - \theta_2) & ... & (I_n + m_n l_{c_n}^2) \end{bmatrix} \tag{2.11}$$

Since the size of the terms make it difficult to display the matrix visually, it is instead summarized in the equation below

$$C_{m,1}(i,j) = \begin{cases} a_j l_i \sin(\theta_j - \theta_i)(\dot{\theta}_j - \dot{\theta}_i), & i < j \\ 0, & i = j \\ a_i l_j \sin(\theta_j - \theta_i)(\dot{\theta}_j - \dot{\theta}_i), & i > j \end{cases} \tag{2.12}$$

We will revisit this equation after evaluating the final partials Turning our attention to the partial of kinetic energy with respect to the positions,

$$\frac{\partial T}{\partial \theta_s} = \sum_{i=1}^{n} m_i \mathbf{v}_i \cdot \frac{\partial \mathbf{v}_i}{\partial \theta_s}$$

Given the angular rates are independent of the positions, those partials are zero, leaving only the

partial of the mass velocity of some link i with respect to an arbitrary link angle θ_s.

$$\frac{\partial \mathbf{v}_i}{\partial \theta_s} = \begin{cases} 0 & s > i \\ -l_{c_s}\cos(\theta_s)\dot{\theta}_s\hat{\imath} - l_{c_s}\sin(\theta_s)\dot{\theta}_s\hat{\jmath} & s = i \\ -l_s\cos(\theta_s)\dot{\theta}_s\hat{\imath} - l_s\sin(\theta_s)\dot{\theta}_s\hat{\jmath} & s < i \end{cases} \tag{2.13}$$

Evaluating the dot product,

$$\begin{aligned} \frac{\partial T}{\partial \theta_s} &= \left[l_{c_s} m_s \sum_{j=1}^{s-1} \Big[l_j \dot{\theta}_j \sin(\theta_j - \theta_s) \Big] + l_s \sum_{i=s+1}^{n} \Big[m_i \Big(l_{c_i} \sin(\theta_i - \theta_s) \sum_{j=1}^{i-1} \big[l_j \dot{\theta}_j \sin(\theta_j - \theta_s) \big] \Big) \Big] \right] \dot{\theta}_s \\ &= \left[\Big(l_{c_s} m_s + l_s \sum_{i=s+1}^{n} m_i \Big) \Big(\sum_{j=1}^{s-1} l_j \dot{\theta}_j \sin(\theta_s - \theta_j) \Big) + l_s \Big(\sum_{i=s+1}^{n} m_i l_{c_i} \dot{\theta}_i \sin(\theta_s - \theta_i) \right. \\ &\qquad \left. + \sum_{i=s+2}^{n} \big[m_i \sum_{j=s+1}^{i-1} l_j \dot{\theta}_j \sin(\theta_s - \theta_j) \big] \Big) \right] \dot{\theta}_s \end{aligned}$$

These terms, proportional to velocity, will form a second mass-based damping-type matrix, $C_{m,2}$, which follows the form

$$\begin{aligned} C_{m,2}(s,s) = \Big(l_{c_s} m_s + l_s \sum_{i=s+1}^{n} m_i \Big) \Big(\sum_{j=1}^{s-1} l_j \dot{\theta}_j \sin(\theta_s - \theta_j) \Big) \\ + l_s \Big(\sum_{i=s+1}^{n} m_i l_{c_i} \dot{\theta}_i \sin(\theta_s - \theta_i) + \sum_{i=s+2}^{n} \big[m_i \sum_{j=s+1}^{i-1} l_j \dot{\theta}_j \sin(\theta_s - \theta_j) \big] \Big) \end{aligned} \tag{2.14}$$

where the only populated terms are the diagonal, and all off diagonals are zero. Additionally, by combining these two matrices into one damping matrix $C_M = C_{m,1} + C_{m,2}$, which simplifies the expression and adds the only-diagonal terms of $C_{m,2}$ and the off diagonals of $C_{m,1}$. Substituting these matrix equations into the Lagrangian equation 2.4 above, obtaining the matrix equations of motion (EOM) below

$$M\ddot{\mathbf{q}} + (C_M + C_D)\dot{\mathbf{q}} + K\mathbf{q} = \mathbf{Q} \tag{2.15}$$

To integrate these dynamics, the approach outlined in Mechanical Vibrations by Géradin [11] is used, where for a second order differential equation of the form above in eqn. 2.15, the state vector becomes $\mathbf{r} = [\mathbf{q}^T\ \dot{\mathbf{q}}^T]^T$, and thus the first order differential equation can be written as

$$B\dot{\mathbf{r}} + A\mathbf{r} = \mathbf{p}$$

Where A and B are matrices defined as

$$A = \begin{bmatrix} K & 0 \\ 0 & -M \end{bmatrix}$$

$$B = \begin{bmatrix} C & M \\ M & 0 \end{bmatrix}$$

and the forcing vector, $\mathbf{p} = [\mathbf{Q}^T \; 0]^T$. It can be seen that this provides the initial matrix equation 2.15 for the upper block, and a unity equation of $M\dot{\mathbf{q}} - M\dot{\mathbf{q}} = 0$ for the lower block. Rearranging this for numerical integration yields the differential equation below

$$\dot{\mathbf{r}} = B^{-1}(p - A\mathbf{r}) \tag{2.16}$$

For any general forcing, this equation now contains all the information needed to propagate free dynamics of this system. Further sections will address how the external forcing term is used to incorporate gravitational forces, normal forces, and controller torques.

2.1.2 Gravitational Forces

To add gravitational forces into the dynamics, the partial of the gravitational potential energy with respect to the generalized coordinates is taken, with the negative of the result being the generalized gravity force, $Q_{s_{\text{grav}}}$.

$$V_{\text{grav}} = \sum_{i=1}^{n} m_i y_{m_i} g$$

$$\frac{\partial V_{\text{grav}}}{\partial \theta_s} = g \sum_{i=1}^{n} m_i \frac{y_{m_i}}{\partial \theta_s}$$

$$y_{m_i} = l_{c_i} \sin(\theta_i) + \sum_{j=1}^{i-1} l_j \sin(\theta_j)$$

$$\frac{\partial y_{m_i}}{\partial \theta_s} = \begin{cases} 0 & s > i \\ l_{c_s} \cos(\theta_s) & s = i \\ l_s \cos(\theta_s) & s < i \end{cases}$$

$$\frac{\partial V_{\text{grav}}}{\partial \theta_s} = g\big(m_i l_{c_s} \cos(\theta_s) + \sum_{i=s+1}^{n} m_i l_s \cos(\theta_s)\big)$$

$$Q_{s_{\text{grav}}} = -g\big(l_{c_s} m_s + l_s\Big(\sum_{i=s+1}^{n} m_i\Big)\big) \cos(\theta_s)$$

2.1.3 Contact Forces

Adding contact forces is more difficult than gravitational forces, as contact forces are non-conservative, regardless of the elasticity of the collision. To account for this, the simulation includes checks to determine if a joint is in contact and if it will remain in contact for the next time step. It does this by monitoring the y-position of the links, calculating contact forces once they are within a certain bound of zero. Once in contact, the contact force is calculated to be the required force to keep the y-velocity of the joint at zero given the natural dynamics and other external forces. To prevent joints from becoming stuck to the surface, if the required force is negative, that joint is removed and solver iterates to find the forces for the other joints in contact. The first step in finding which joints are in contact. This can be achieved by comparing the the calculated y position to a

ground threshold value. The y position and velocity for the end of the i^{th} joint are defined below

$$y_i = \sum_{j=1}^{i} l_j \sin(\theta_j)$$
$$\dot{y}_i = \sum_{j=1}^{i} l_j \dot{\theta}_j \cos(\theta_j)$$

Since the equation for the effect of the forces on the state is nonlinear in the state, with an additional objective function which is also nonlinear in the state, an iterative Newton-Raphson solver is used to find the required forces. Using the matrix form

$$\mathbf{x}_k = \mathbf{x}_{k-1} - J(\mathbf{x}_{k-1})^{-1}\mathbf{f}(\mathbf{x}_{k-1}) \tag{2.17}$$

where J is the partial of the objective function with respect to the search variable, $\frac{\partial \mathbf{f}}{\partial \mathbf{x}}$. For our case, the objective function is the y velocity of joints in contact, $\dot{y}_i$, and the search variable is the normal force at that joint, N_i. So if an arbitrary m joints indices $\mathbf{i}_c = [i_{c,1}\ i_{c,2},\ ...,\ i_{c,m}]$ in contact, the objective function would be $\mathbf{f} = [\dot{y}_{i_{c,1}}\ \dot{y}_{i_{c,2}},\ ...,\ \dot{y}_{i_{c,m}}]^T$, and the search variable is $\mathbf{x} = [N_{i_{c,1}},\ N_{i_{c,2}},\ ...,\ N_{i_{c,m}}]^T$. With the necessary terms defined, the Jacobian, J, can be found. Starting from the the y velocity of a random joint s, the effect of a normal force on joint i can be determined from a potential function, like for the gravitational forces, though this one will be discontinuous. The potential function for normal forces is defined below

$$V_{\text{N}} = -\sum_{i=1}^{n} \begin{cases} N_i y_i, & y_i \leq 0,\ \&\ N_i > 0 \\ 0, & \text{else} \end{cases} \tag{2.18}$$

Taking the partial with respect to the generalized coordinates,

$$\frac{\partial V_{\mathrm{N}}}{\partial \theta_s} = \sum_{i=\mathbf{i}_c} N_i \frac{y_i}{\partial \theta_s}$$

$$\frac{\partial y_i}{\partial \theta_s} = \begin{cases} 0 & s > i \\ l_s \cos(\theta_s) & s \leq i \end{cases}$$

$$\frac{\partial V_{\mathrm{N}}}{\partial \theta_s} = -l_s \cos(\theta_s) \sum_{i=\mathbf{i}_c \geq s} N_i$$

$$Q_{N_s} = l_s \cos(\theta_s) \sum_{i=\mathbf{i}_c \geq s} N_i$$

For an arbitrary time step k, our objective is to find the force setting the y component of velocity to zero at the next time step, $\dot{y}_{i_{c,a},k} = 0$. Taking the partial with respect to $N_{i_{c,b}}$,

$$\frac{\partial \dot{y}_{i_{c,a},k}}{\partial N_{i_{c,b}}} = \sum_{j=1}^{i_{c,a}} \big[l_j \big(\frac{\partial \dot{\theta}_{j,k+1}}{\partial N_{i_{c,b}}} \cos(\theta_{j,k+1}) - \dot{\theta}_{j,k+1} \sin(\theta_{j,k+1}) \frac{\partial \theta_{j,k+1}}{\partial N_{i_{c,b}}} \big) \big]$$

To find the partial of the states at time $k+1$, the dynamics definition from equation 2.16, the effect of the normal force on the state at the next time step using an Euler approximation, $\mathbf{r}_{k+1} = \mathbf{r}_k + B_k^{-1}(\mathbf{p} - A_k \mathbf{r}_k)\mathrm{d}t$. Using this definition, and starting with the partial with respect to the full state, since θ and $\dot{\theta}$ are linear transformations of the full state, the form for the required partials above is shown below.

$$\frac{\partial r_{k+1}}{\partial N_{i_{c,b}}} = B_k^{-1} \frac{\partial \mathbf{p}}{\partial N_{i_{c,b}}} \mathrm{d}t$$

$$\frac{\partial \mathbf{p}}{\partial N_{i_{c,b}}} = [l_1 \cos(\theta_1),\ l_2 \cos(\theta_2),\ ...,\ l_{i_{c,b}} \cos(\theta_{i_{c,b}}),\ 0,\ ...,\ 0]^T$$

Since the A and B matrices are dependent of the state at the previous time step, they are independent of the normal force, making these partials relatively simple. Assembling these terms shows that each term of the Jacobian can be written with the matrix equation

$$J(a,b) = [-l_1 \dot{\theta}_1 \sin(\theta_1),\ ...,\ -l_a \dot{\theta}_a \sin(\theta_a),\ 0, ...,\ l_1 \cos(\theta_1),\ ...,\ l_a \cos(\theta_a),\ 0, ...,\ 0] B_k^{-1} \frac{\partial \mathbf{p}}{\partial N_{i_{c,b}}} \mathrm{d}t \tag{2.19}$$

2.1.4 Frictional Forces

Frictional forces are incorporated using the Coulomb friction model, where friction is proportional to the normal force by some constant coefficient of friction, μ. This creates a new potential function

$$V_{\mathrm{f}} = -\sum_{i=1}^{n} \begin{cases} N_i y_i - |\int_{x_i} f_i dx|, & y_i \leq 0, \ \& \ N_i > 0 \\ 0, & \text{else} \end{cases} \tag{2.20}$$

Since this force acts in the x direction, the x position and velocity of each joint are defined below

$$x_i = \sum_{j=1}^{i} l_j \cos(\theta_j)$$

$$\dot{x}_i = -\sum_{j=1}^{i} l_j \dot{q}_j \sin(\theta_j)$$

In equation 2.20, the integral is defined as the force integrated over the total distance traveled, which can also be parameterized in time, making the upcoming partials more clear. Additionally, the relationship to the normal force is made more clear, such that there is only one force variable.

$$V_{\mathrm{f}} = -\sum_{i=1}^{n} \begin{cases} N_i y_i - |\int_{t_o}^{t_f} \mu N_i(t) \dot{x}_i \mathrm{d}t|, & y_i \leq 0, \ \& \ N_i > 0 \\ 0, & \text{else} \end{cases}$$

To find the generalized force, the partial is taken with respect to the state, as with the above two forces. This results in the generalized force as a function of the normal force shown below

$$Q_{s_{\mathrm{f}}} = l_s \sum_{i=\mathbf{i}_c \geq s} \left[\big(\cos(\theta_s) - sign(\dot{x}) \mu \sin(\theta_s) \big) N_i \right] \tag{2.21}$$

Now that the equation for the generalized friction force has been found, repeating the process for the combined normal and friction forces as with normal alone in the previous section finds a new Jacobian. Conveniently, the only change is to the partial of the force vector $\mathbf{p}$ with respect to the normal, which now becomes

$$\frac{\partial \mathbf{p}_{\mathrm{f}}}{\partial N_{i_{c,b}}} = [l_1(\cos(\theta_1) - sign(\dot{x}_{i_{c,b}})\mu \sin(\theta_1)), \ l_2(\cos(\theta_2) - sign(\dot{x}_{i_{c,b}})\mu \sin(\theta_2)), \ ...,$$

$$l_{i_{c,b}}(\cos(\theta_{i_{c,b}}) - sign(\dot{x}_{i_{c,b}})\mu \sin(\theta_{i_{c,b}})), \ 0, \ ..., \ 0]^T$$

2.1.5 Control

The final piece of the limb-only model is the implementation of control to begin testing crawl control schemes. Moment forcing is assumed at specific joints, which is consistent with the output of angular HASEL actuators developed by KRG [1]. Finding the effect of a joint moment on the states, requires creating a potential function for the moment from an actuator at an arbitrary joint i.

$$V_{\text{ctrl}} = -M_i(\theta_i - \theta_{i-1}) \tag{2.22}$$

While it might not be immediately apparent that the potential should be of the relative angle, simple examination shows that if the relative angle remains constant, the joint actuator would not have moved, and thus has done no work. The generalized forces due to control are thus

$$\frac{\partial V_{\text{ctrl}}}{\partial \theta_s} = -M_i + M_{i+1}$$

$$Q_{ctrl_s} = M_i - M_{i+1}$$

assuming that all links are actuated. Any non-actuated links could would have that moment as always zero.

Now that there is an implementation for control torques in the model, it is time to start working on building a controller. The first step is finding a reference path to control around. For the purposes of this work, reference paths were manually built for the 3 and 4 link cases, so future work is needed to determine an optimal crawling trajectory. For both of these manually constructed trajectories, the last link was kept flat against the ground and the other link angles were calculated to maintain flat ground contact of that link. To account for the extra degree of freedom posed by the 4 link case, the reference angle for the second link was also zero. For these cases, all links except the final were actuated, so the passive dynamics played a comparatively small role. More work needs to be done in determining effective control schemes for cases where the passive dynamics play a larger role.

Two methods were used for determining controller gains. The first was to use gains proportional

to the angle and rate errors separated at each joint to determine the control torque at that joint, that is, $M_i = K_{p,i}(\theta_i - \theta_{r,i}) + K_{d,i}(\dot{\theta}_i - \dot{\theta}_{r,i})$, where $\theta_{r,i}$ and $\dot{\theta}_{r,i}$ are the reference positions and rates, respectively. The second approach was to use an LQR controller to produce a full-state gain matrix. Since A and B matrices have a slightly different meaning in [11] than most standard formulations, an alternate notation is used, outlined below.

$$\dot{\mathbf{r}} = F\mathbf{r} + G\mathbf{p} \tag{2.23}$$

Though F and G are normally reserved for discrete time state space formulations, since no discrete time analysis is done in this work, seems like a reasonable way to avoid confusion. In reference to the A and B matrices defined above, F and G are thus determined to be

$$F = B^{-1}A \tag{2.24}$$

$$G = B^{-1} \tag{2.25}$$

Using the F and G matrices and solving the matrix Ricatti equation finds the optimal gain for some controller cost function. As is typical with designing an LQR controller, the Q and R matrices were tuned to provide an adequate but stable response.

2.2 Results

To verify that the dynamics are correct, the energy of the links is calculated for each time step of the simulation, along with the energy dissipated by the dampers, to be sure that any mechanical energy lost by the system is accounted for with energy dissipated by the dampers or friction. With contact forces, since a perfectly inelastic collision is assumed, the total energy should have a step decrease upon each impact. Plots of the states and energies for a few test cases are shown below. Most plots are shown with 3 links for simplicity, however, a more complicated arm can be simulated, and results from such a test are shown in the last subsection. In addition to producing the state and energy plots shown, the script also can produce animations of the links for a given simulation, which can be easier to interpret for reasonableness. An example of a frame of this animation is

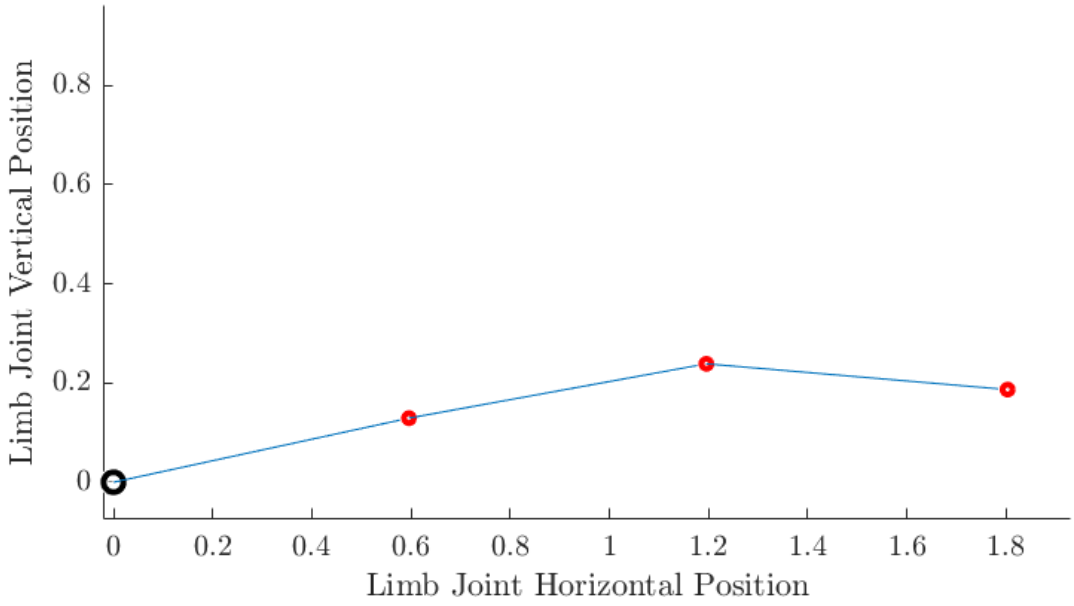

Figure 2.3: Frame capture of the animation of the 3-link contact case. Blue lines are the links, red circles are the joints, and the larger black circle at the base is the root joint.

shown in figure 2.3 To decrease the number of variables, all limbs shown in results use the petal shape shown in the images of the AoES, have a total length of $1.8m$, thickness of $2.54x10^{-3}$m, an elastic modulus of 4.36Mpa, and limb density of $1000\frac{\text{kg}}{\text{m}^3}$. Unless otherwise noted, the time step for these simulations is 0.01s, with the simulation time varying depending on the phenomenon being observed.

2.2.1 Unforced

To show that the model performs with only internal forces, the unforced dynamics case is shown here. As expected, the system oscillates about angles of zero for each link, and the energy rate is clearly only numerical errors, and is centered on zero, confirming the unforced dynamics.

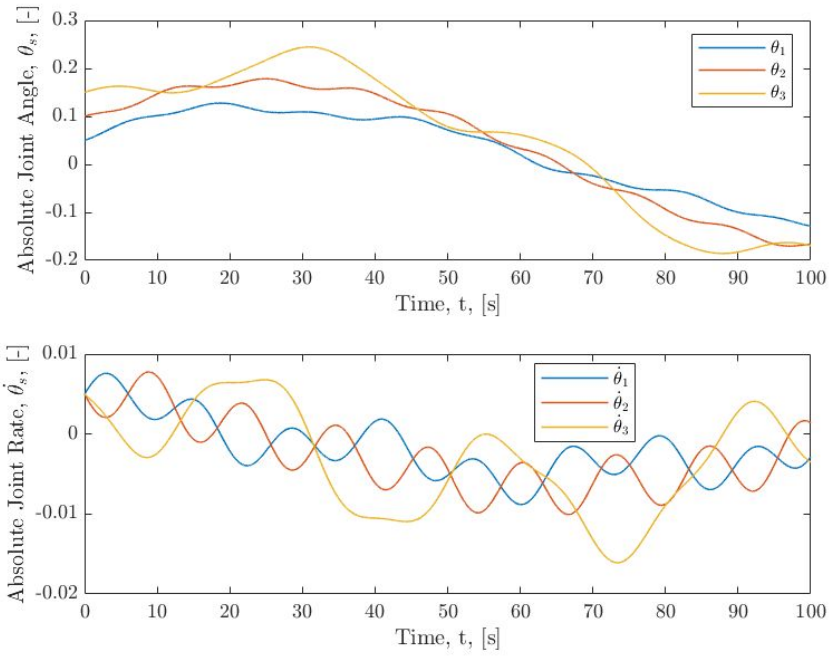

Figure 2.4: This plot of the system states, with angles on the upper subplot and angular rates on the lower, shows the system behavior over a 100 second simulation. the limb oscillates due to the restoring force from the springs

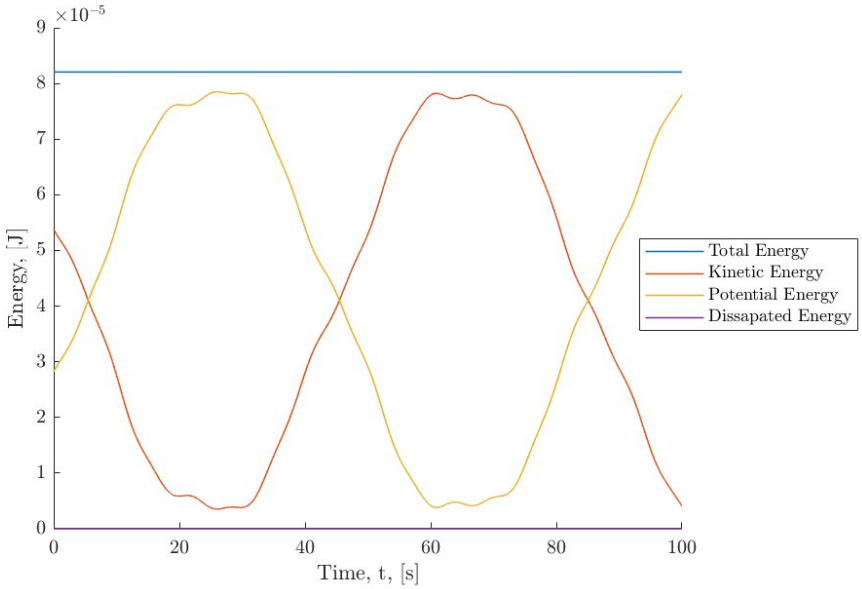

Figure 2.5: Plot of the system energies over a 100 second simulation. Over this period, energy passes between kinetic an potential, as expected, since these is no form of dissipation.

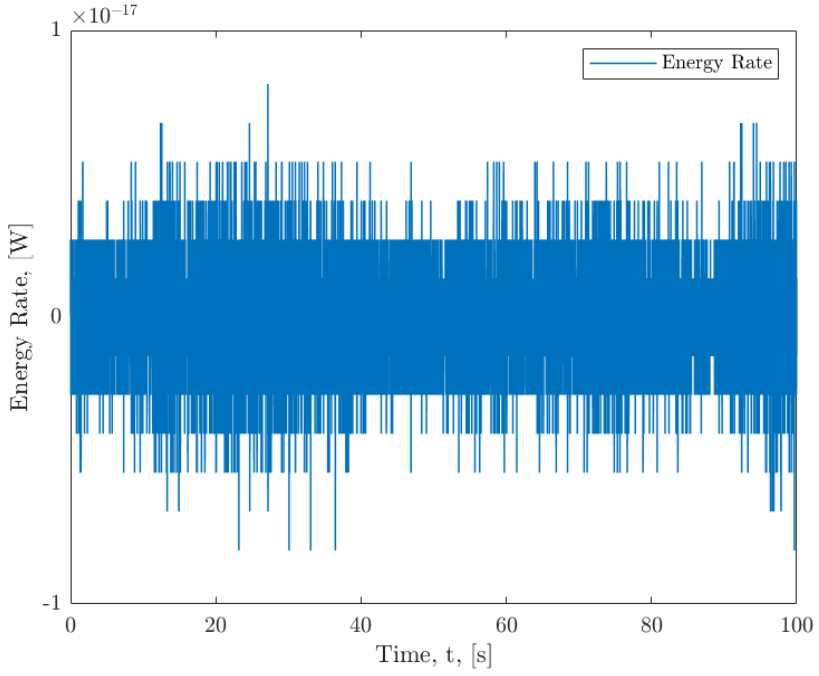

Figure 2.6: Energy rate plot over a 100 second simulation. Over this period, energy rates are clearly numerical errors.

2.2.2 Gravitational Forcing, No Damping

For the most simple forcing case, the simulation produces results as seen in figures 2.7, 2.8, and 2.9. For these simulations, the gravitational acceleration used is $0.001\frac{\mathrm{m}}{\mathrm{s}^2}$, which was chosen because it produced a reasonably sized response for the limb parameters selected. The simulation performs as expected, with link angular decreasing from their initial nonzero values as the limb is pulled by gravity. Because of the positive initial rates, the angles initially increase, but start decreasing shortly, only rebounding from the spring forces at the end of the simulation time. Without damping, this system would oscillate indefinitely. The only point of interest in these plots is the smooth nature of the energy variations seen in fig. 2.11. Investigating this discrepancy found that these variations are unchanging in shape for a certain initial condition, and that the value at a given time are exactly proportional to the size of the time step, which indicates it is related to a simulation, rather than the underlying dynamics. The most likely explanation is that this results from the way that the forcing is implemented. All forces are calculated at the beginning of each time step, and the numerical values are then fed to the dynamics equation, where the state is propagated with a fourth order Runge-Kutta. Since each sub step of the integration updates the state, and the value of the generalized force of gravity is position dependent, this leads to small errors that would not be present if that force were recalculated at each sub step This idea seems supported by the fact that the maxima of the kinetic energy and energy rate change occurring at similar times, which would be the point when the angles are changing the fastest. While the error seems to be sufficiently small, it could be worth looking into solving the issue by adding gravity separately from other forces in a way that allows it to update with the state.

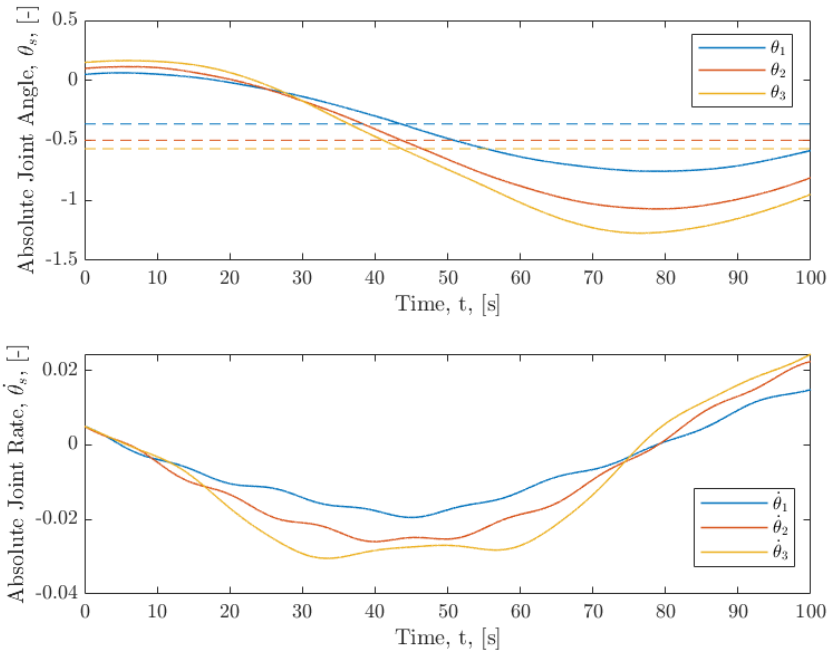

Figure 2.7: This plot of the system states, with angles on the upper subplot and angular rates on the lower, shows system behavior over a 100 second simulation. Dashed lines show the steady-state angle for each link

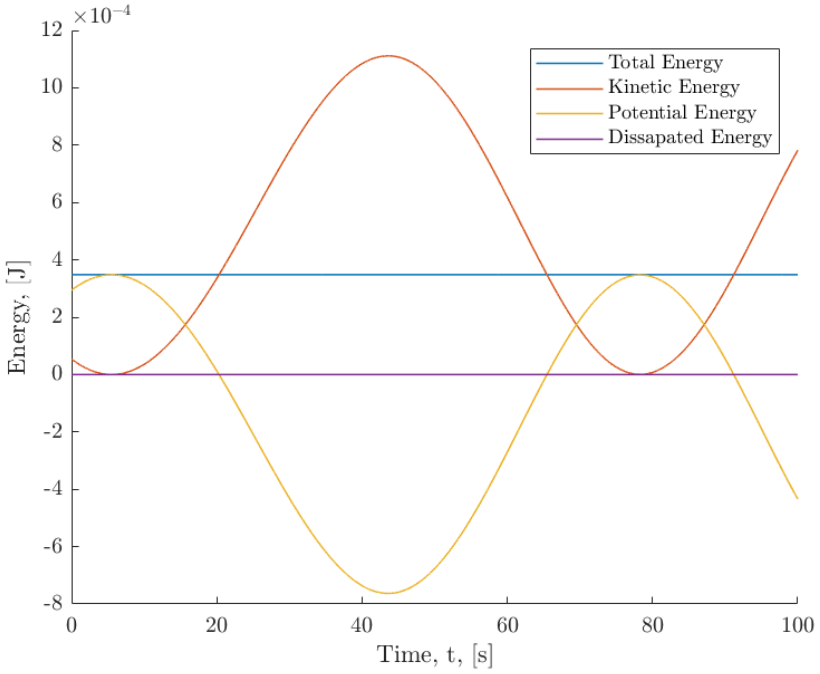

Figure 2.8: Energy plot of the gravitational forcing simulation, which shows that the total energy remains constant, which is expected, as no energy is entering or exiting the system, and dissipated energy remains zero, since there is no internal damping.

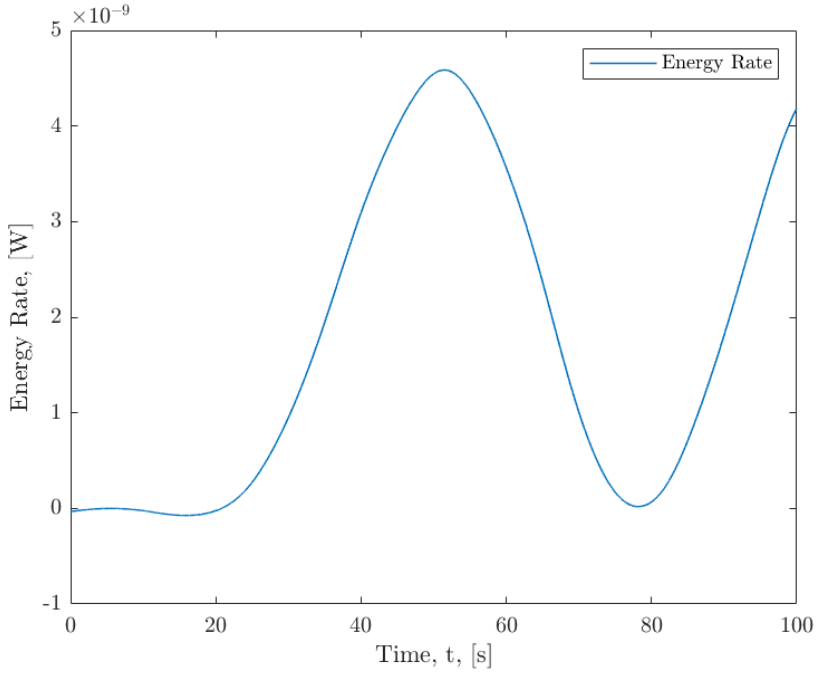

Figure 2.9: In the energy rate plot, the energy changes are over five orders of magnitude below the scale of the energy, small enough to be safely written off as numerical error. The smoothness of the plot is likely a result of the way the nonlinear gravitational force was calculated, potentially leading to a position based error. Investigating and potentially fixing, thus further reducing the magnitude of the energy rate, will be the subject of future inquiry.

2.2.3 Gravitational Forcing, With Damping

Including viscous damping the internal forces yields the simulation results as seen in figures 2.10, 2.11, and 2.12. For these simulations, the damping ratio at each joint was set to 0.4, and the time step was increased to 0.1s to account for the extra simulation time needed to reach steady state. The gravitational acceleration remains the same as above to maintain as much similarity as possible with the undamped case. While helping to verify the compatibility of viscous damping terms with the gravitational forcing, as well as ensure the system would eventually reach a steady state. As can be seen in figure 2.10, all the limb angles converge to their expected steady state values, confirming the gravitational force values. Additionally, the hypothesis for the cause of the

energy rate discrepancy is further supported, since the magnitude is approximately scaled by the time step increase and all the local maxima correspond reasonably well with a local maximum in the kinetic energy plot.

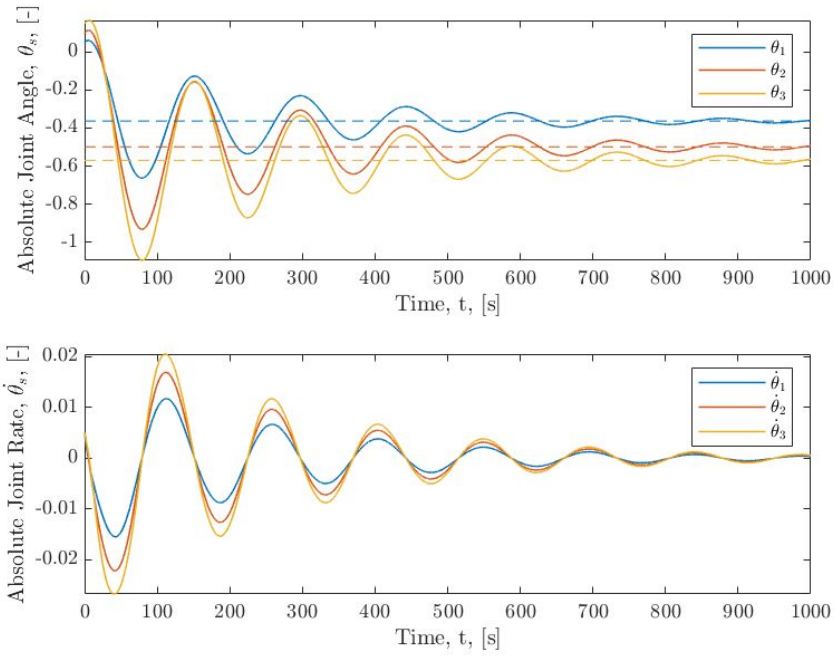

Figure 2.10: In this plot of the system states, now with damping, all states approach their predicted steady state values with time, helping to verify the accuracy of the forcing function. While the first 100 seconds fairly closely resemble the no-damping case, it is clear and the simulation progresses that energy is being extracted from the system.

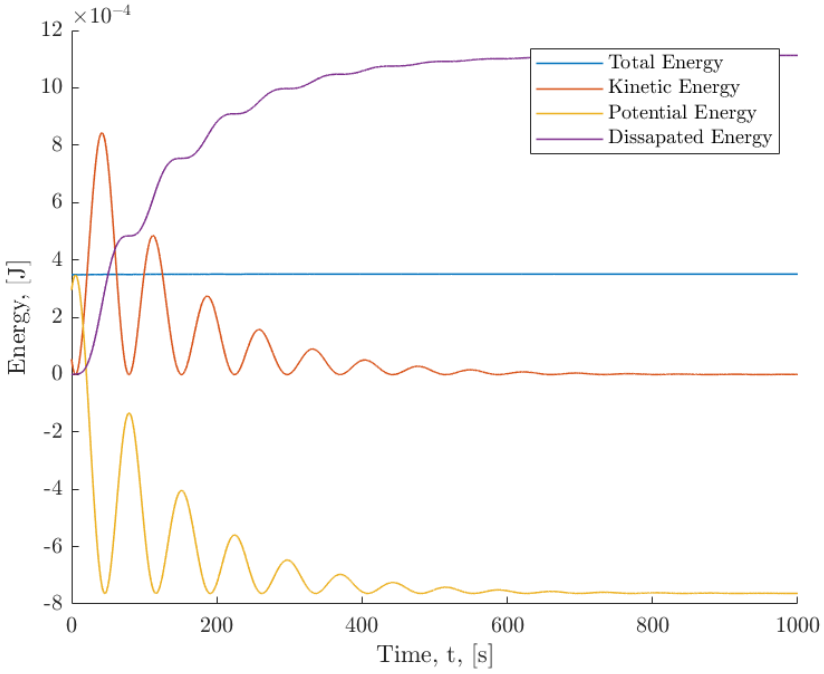

Figure 2.11: The total energy, defined as mechanical plus dissipated energy remains constant, which is due to the fact that it is a summation of the kinetic, potential, and dissipated energies, as a means of verifying the accuracy of damping forces in the simulation. As is expected, kinetic energy goes to zero while the potential settles at a negative value, since zero potential energy is defined as level with the root node.

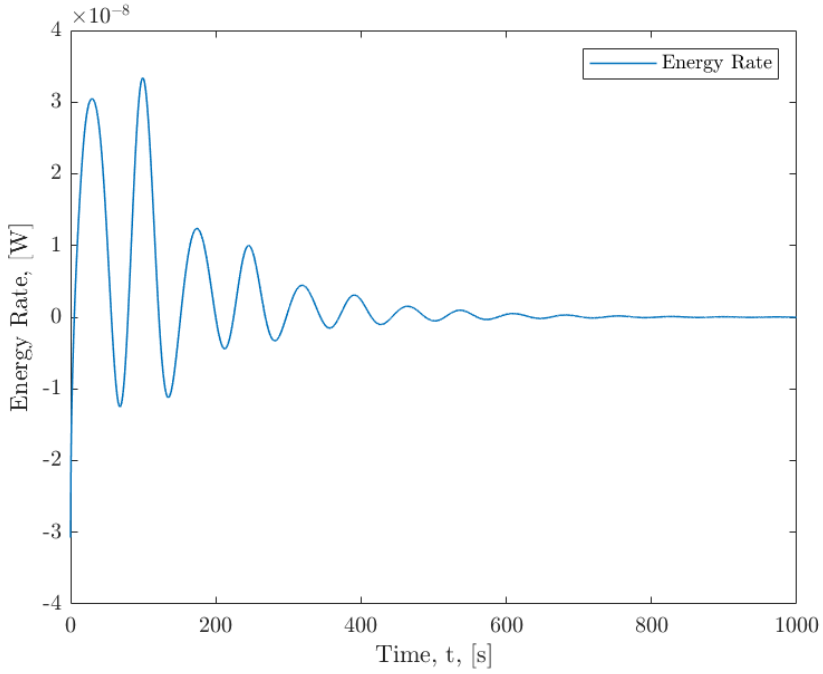

Figure 2.12: The energy changes are four orders of magnitude below the scale of the energy, which, while closer than before, are a result of increasing the size of the time step to account for the increase in simulation time. This time step size dependence further supports the idea that this error is numerical in nature.

2.2.4 Contact Forces, No Damping

Including contact forces creates the results seen in figures 2.13 and 2.14. It is important to note that there is no joint damping for these simulations, meaning all the mechanical energy lost is because of the impacts with the ground. These figures show an initially down curved limb drawn down by restoring forces and gravity before impacting, first on the second joint, followed by the first and third. Impacts appear as discontinuities in the plot of total energy, where it can be seen that further impacts occur past the first three initial mentioned, as an impact from a joint nearer to the end can cause another, earlier joint to be forced off the ground. This phenomenon clearly happens in this case, as there are six impacts but only 3 links.

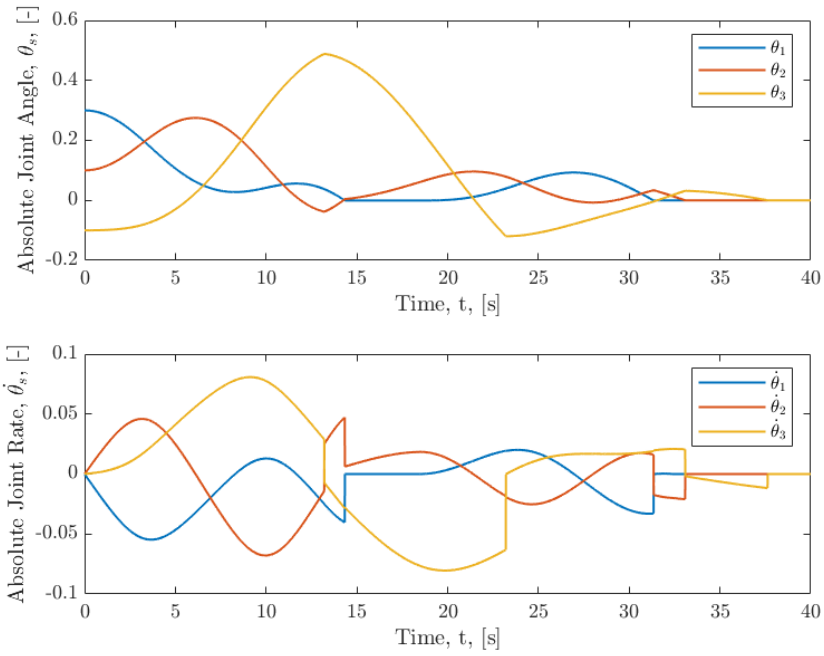

Figure 2.13: The state plot after adding contact forces shows a new, angular behavior associated with the introduction of contact forces. As joints come into contact with the ground, impulses create step changes in the velocity, and after the initial contact, normal forces prevent any joint from moving downward. By the end of the 40 second simulation, all the links have come to rest.

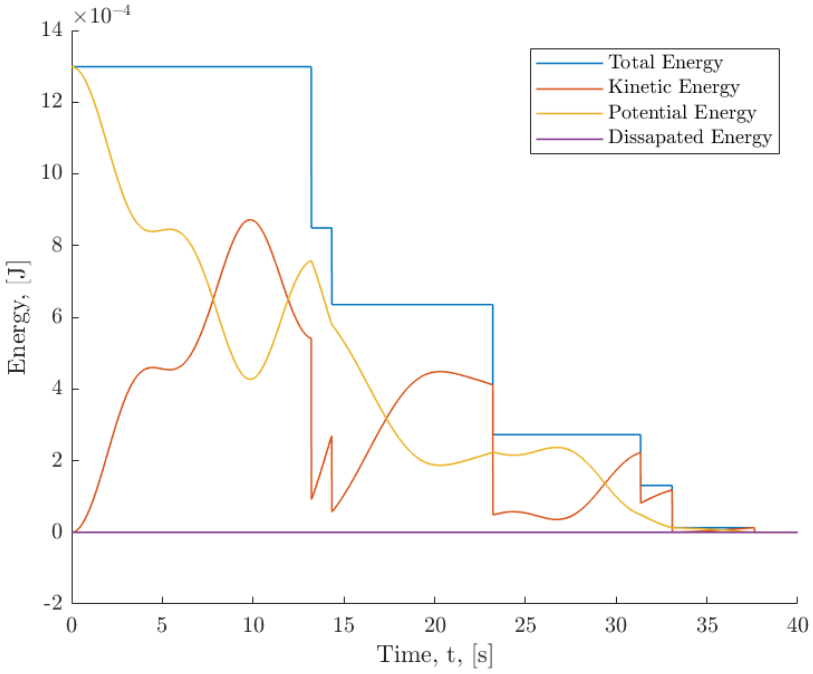

Figure 2.14: The normal force energy plot shows that the total energy remains constant between impacts, and experiences step decreases at each impact, which is expected, as energy is not conserved in inelastic collisions. Kinetic and potential energy are smooth between impacts, and only kinetic energy experiences significant step changes. this is expected, as only rates experiences step changes in the state plot, and potential energy is only a function of position.

2.2.5 Friction forces, no damping

Adding friction forces to the contact produces the figures seen below. There is nothing particularly of note in the state plot, though in the energy plot accounting for the energy dissipated by sliding friction causes the same step-wise behavior to the energy seen in the friction-less case above. The plots below also represent results where the material had no stiffness, this is because the variability in contact force when the joint springs are present obfuscates the role of friction.

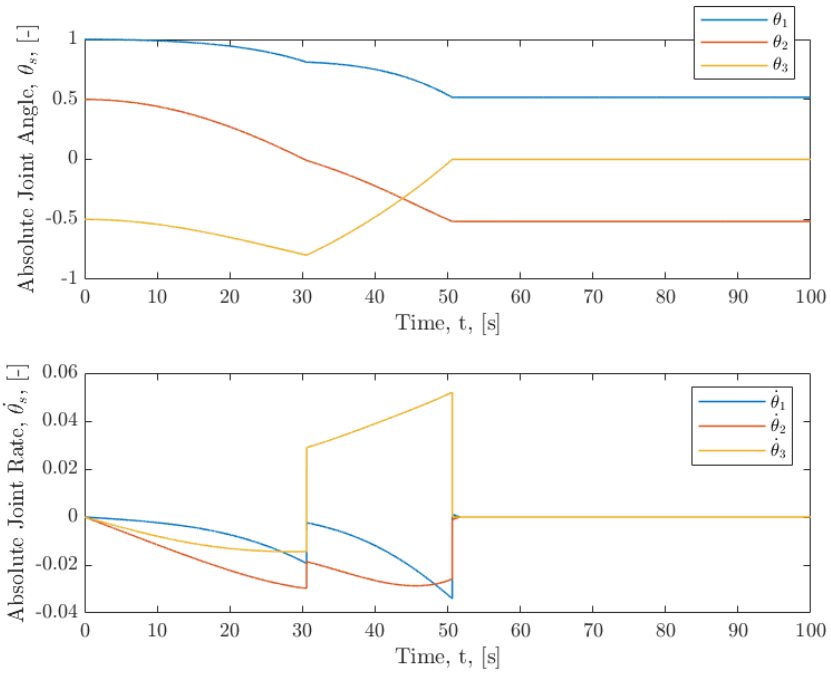

Figure 2.15: This plot of the system states shows similar behavior to the contact case, but with a slower response than without friction.

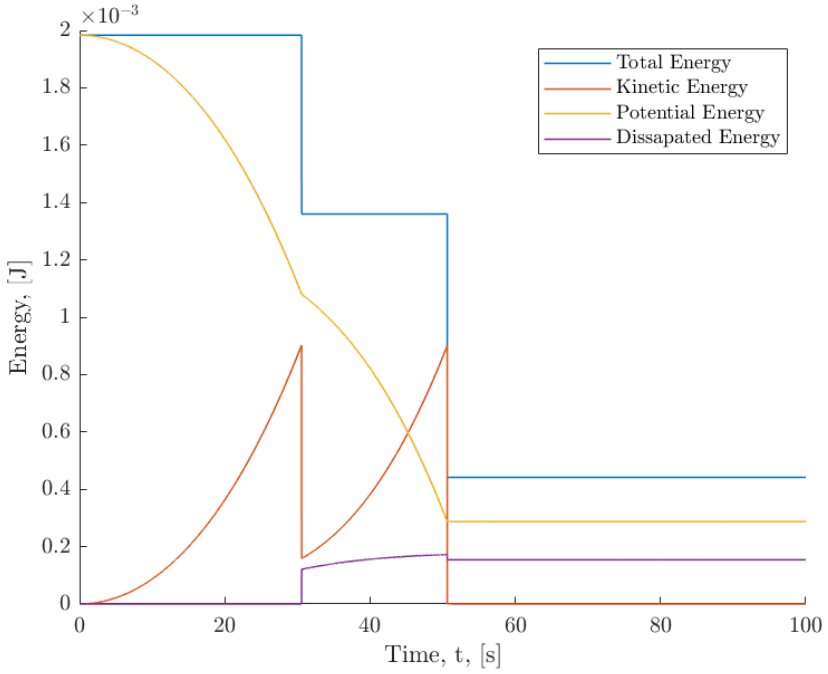

Figure 2.16: Total energy remains constant between impacts, when the energy lost from sliding friction forces are accounted for in the dissipated energy

2.2.6 Control

Controlling a limb for a specified path with all the forces shown above leads to the plots shown below. The controller gains here were found with an LQR method, where the gains were calculated around angles and rates of zero, and no penalty was applied to angle or rate errors of the final, uncontrolled link. Figure 2.18 shows that the most significant errors occur when a joint makes contact, since the controller does not take this nonlinearity into account. Overall, the controller behaves promisingly, especially given the disturbances posed by the final link and ground contact. An energy plot was not included here, since all other forces are confirmed to behave as expected and the actuators add energy to the system.

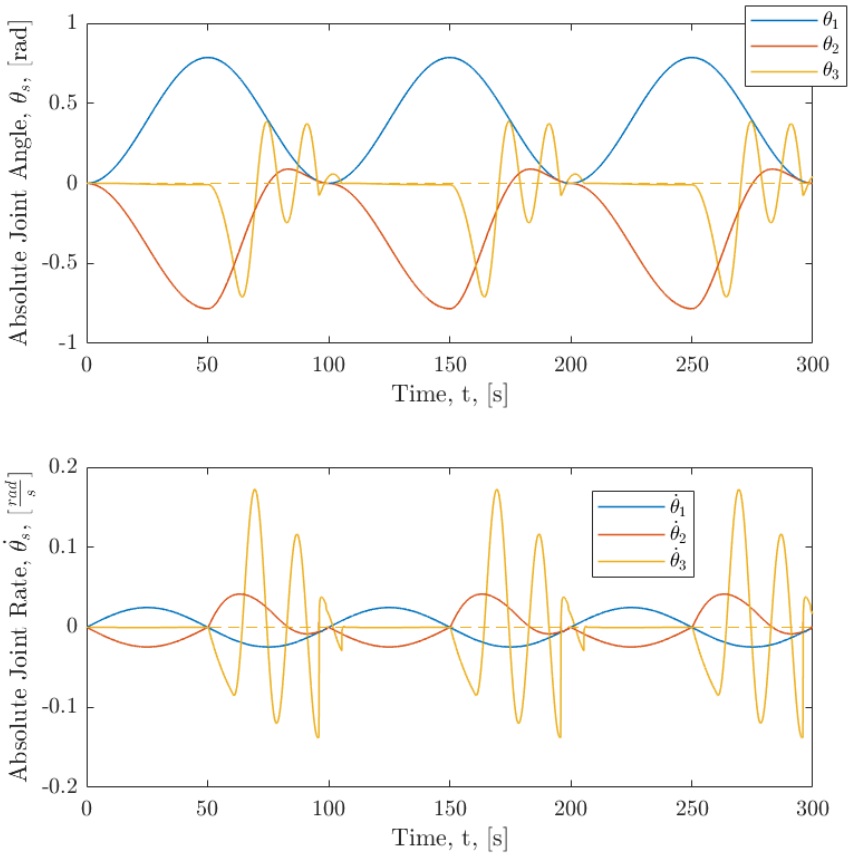

Figure 2.17: Plot of the system states, showing the controller doing a reasonable job of tracking the states for 3 cycles.

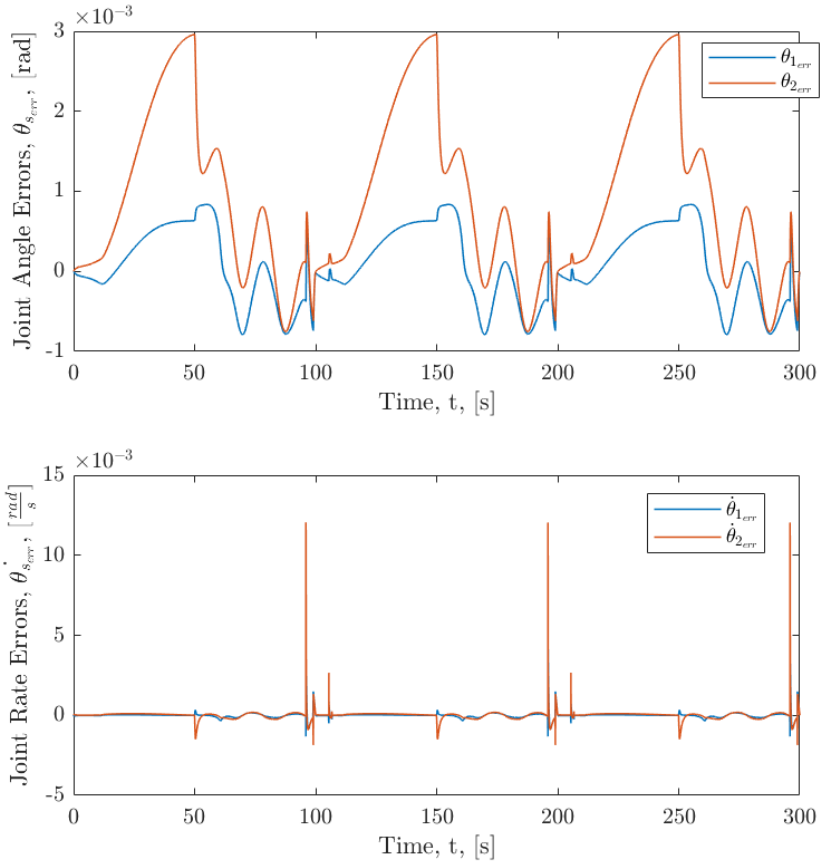

Figure 2.18: In this plot of the controlled state errors, the controller reasonably tracks reference states for 3 cycles, which is not unexpected, since the actuators are not torque limited like a real HASEL actuator would be.

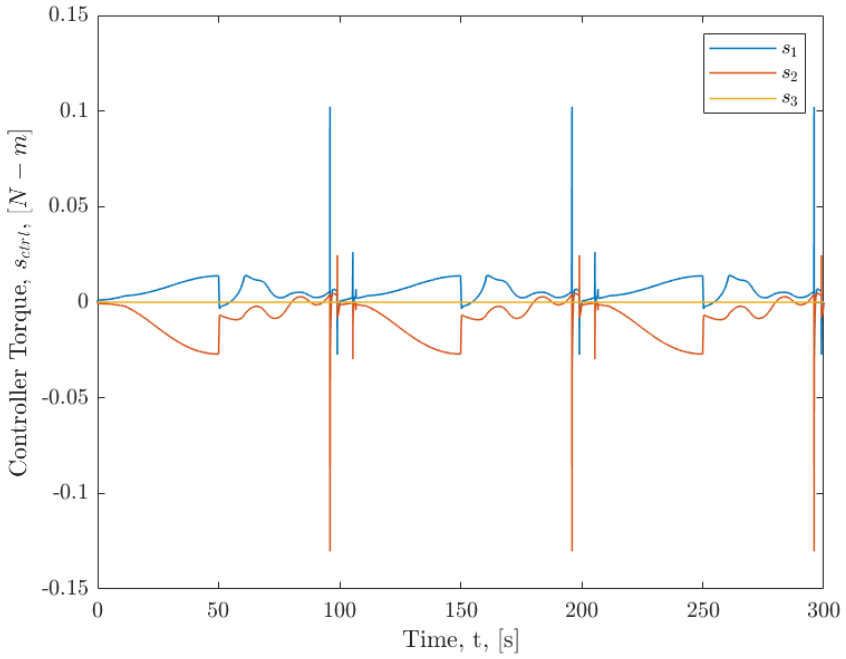

Figure 2.19: This torque plot shows the controller torques used to maintain the reference path tracking shown above

2.2.7 10 Link case

This case is meant to show the versatility of the model in easily increasing the number of links. Control is not shown here, though all other forces are. One of the primary benefits of this aspect of the model would be with control, in creating an under actuated system to get a sense for how a control law will react to the passive dynamics between actuators.

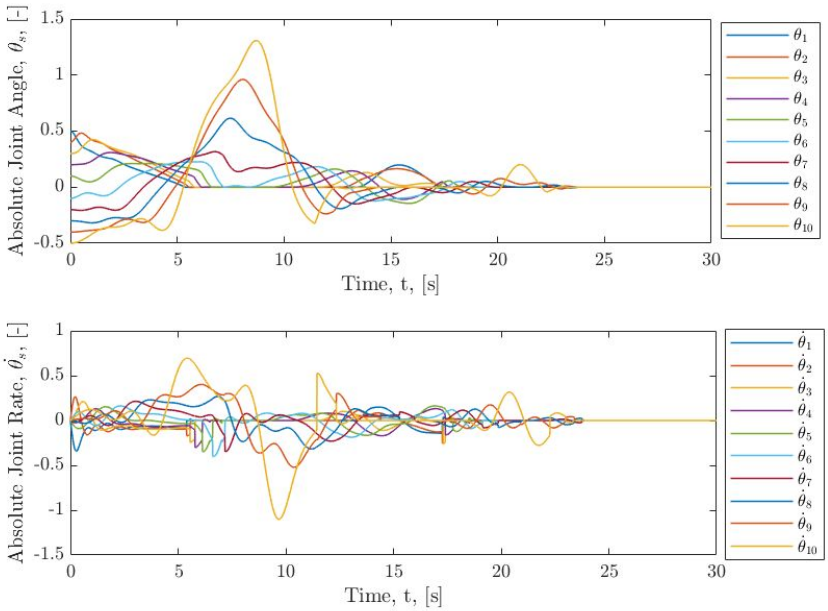

Figure 2.20: This plot of the system states shows that these high link-count simulations are difficult to interpret, which is why the animations are very useful here.

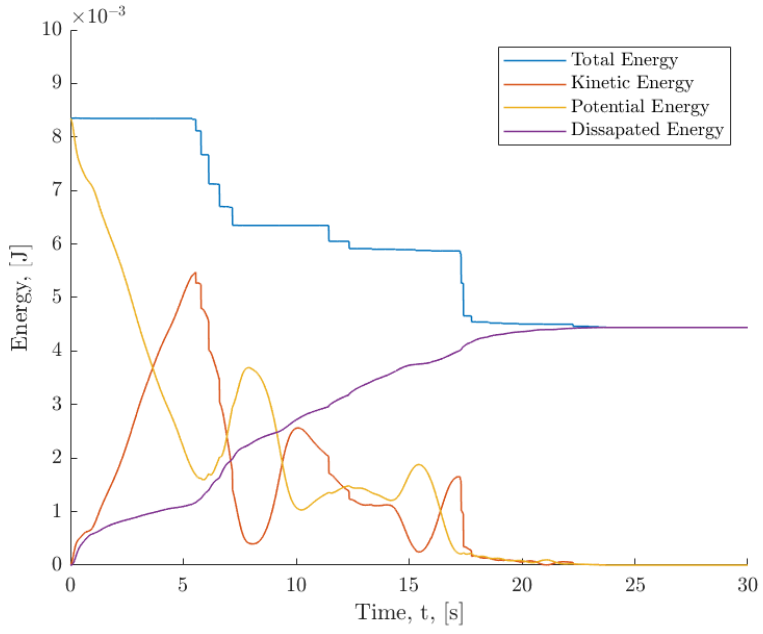

Figure 2.21: In this energy plot, total energy remains constant between impacts, confirming the model with 10 links.

Chapter 3

Full Robot Dynamics Model

3.1 Derivation

3.1.1 Unforced Dynamics

This section outlines the dynamics derivation for the Full AoES model, including the modified solution setup, as well as the modifications to the external force derivations. The new model diagram can be seen in figure 3.1. On either side of a hub link, there are mirrored limbs, one left and one right. The link number relates to the distance from the hub, so the first left and first right links are directly connected to the hub, until the n^{th} link at the end of each limb. The hub link varies from the other two links in that the hub mass can have some height above the hub link, to account for the y height of the hub on the real AoES. Unlike the limb model, no part of these links are fixed, so the model is free to move in the the x and y directions, which will be critical for determining if a given control sequence will cause the AoES to crawl. Definitions for the model parameters are outlined in the diagram figure caption.

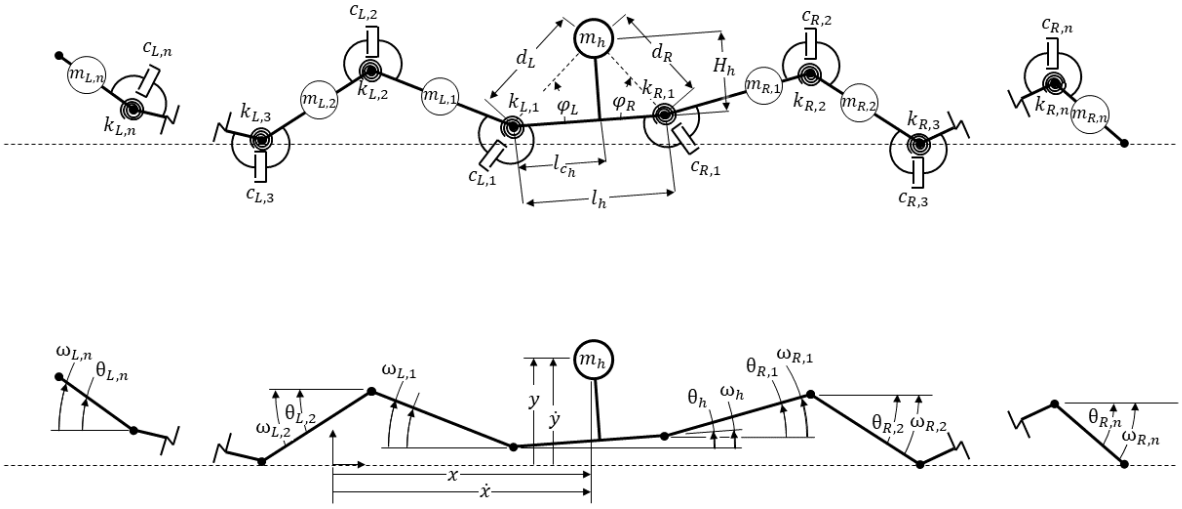

Figure 3.1: Diagram of the model parameters for the full AoES model (top), and states (bottom). Parameters maintain the definitions from the limb-only model in fig. 2.2, with the addition of an L or R to indicate if it is for the left or right-hand limb, respectively. The limb length and mass positions are left off this diagram given the many terms on this diagram already, but follow the same convention as the limb-only model. Additionally, d_L and d_R are used as simplification terms for the distance from the hub mass to the left and right joints, as the hub link length or limb mass position terms never appear alone. ϕ_L and ϕ_R function similarly, completing the description of the mass position. On the bottom plot, the states are illustrated, with arrows indicating positive direction. For this model, the right hand limb, as well as the hub, follow the sign convention that right handed rotation about an axis out of the page is positive, while the left-handed limb is defined such that right handed rotations about an axis into the page are positive.

Using the same Lagrangian solution approach as for the limb, but with new kinetic and potential energy equations to account for the new links and lack of a fixed base. Since a Lagrangian approach is used, a set of generalized coordinated must be defined. For this set of connected rigid

links, the natural set of coordinates which completely and minimally define the full range of system motion are the angles of each link, so $q = [\theta_1,\ \theta_2, ...,\ \theta_n]^T$. The state vector for the resulting equations of motion are thus $r = [q\ \ \dot{q}]^T$ or $r = [\theta_1, ...,\ \theta_n,\ \dot{\theta}_1, ...,\ \dot{\theta}_n]^T$. Building off of the limb-only plot, the complete unfixed model illustrated in figure 3.1, contains two mirrored examples of the limb only model fixed to a hub link. The hub, unlike the limb links, has a vertical offset for the mass to account for the substantial height of the hub. The generalized coordinated for this model are now more complex, since the robot is no longer constrained at any of the joints. For this model, the hub mass x and y positions are the tracked Cartesian coordinates, giving the set of generalized coordinated to be $q = [\theta_{L,n}, ...,\ \theta_{L,1},\ x,\ y,\ \theta_1,\ \theta_{R,1}, ...,\ \theta_{R,n}]^T$. The state vector remains defined as $r = [q\ \ \dot{q}]^T$. Now that the system states and parameters have all been defined, the system derivation can begin. We start with the kinetic and potential energies, as defined below

$$T = \frac{1}{2}\Big(m_h \mathbf{v}_h \cdot \mathbf{v}_h + I_h \dot{\theta}_h^2 + \sum_{i=1}^{n} \left[m_{L,i} \mathbf{v}_{L,i} \cdot \mathbf{v}_{L,i} + I_{L,i} \dot{\theta}_{L,i}^2 + m_{R,i} \mathbf{v}_{R,i} \cdot \mathbf{v}_{R,i} + I_{R,i} \dot{\theta}_{R,i}^2\right]\Big)$$

$$V = \frac{1}{2}\Big(k_{L,1}(\theta_{L,1} + \theta_h)^2 + k_{R,1}(\theta_{R,1} - \theta_h)^2 + \sum_{i=2}^{n} \left[k_{L,i}(\theta_{L,i} - \theta_{L,i-1})^2 + k_{R,i}(\theta_{R,i} - \theta_{R,i-1})^2\right]\Big)$$

In addition, since most materials dissipate energy during movement, represented by the torsional dampers in the model, a dissipation function must also be considered. For the linear torsional dampers modeled, this is given by the equation below

$$D = \frac{1}{2}\Big(c_{L,1}(\dot{\theta}_{L,1} + \dot{\theta}_h)^2 + c_{R,1}(\dot{\theta}_{R,1} - \dot{\theta}_h)^2 + \sum_{i=2}^{n} \left[c_{L,i}(\dot{\theta}_{L,i} - \dot{\theta}_{L,i-1})^2 + c_{R,i}(\dot{\theta}_{R,i} - \dot{\theta}_{R,i-1})^2\right]\Big)$$

Where L and R denote the left and right hand limbs, respectively. These definitions can be use when applying the Lagrange equation below to find the equations of motion for an arbitrary coordinate q_s. Starting with the partial for the potential energy with respect to the generalized positions, the

process of which for the various coordinates is outlined below

$$\begin{aligned}
\frac{\partial V}{\partial x} &= 0 \\
\frac{\partial V}{\partial y} &= 0 \\
\frac{\partial V}{\partial \theta_h} &= k_{L,1}(\theta_{L,1} + \theta_h) - k_{R,1}(\theta_{R,1} - \theta_h) \\
&= (k_{L,1} + k_{R,1})\theta_h + k_{L,1}\theta_{L,1} - k_{R,1}\theta_{R,1} \\
\frac{\partial V}{\partial \theta_{L,1}} &= k_{L,1}(\theta_{L,1} + \theta_h) - k_{L,2}(\theta_{L,2} - \theta_{L,1}) \\
&= (k_{L,2} + k_{L,1})\theta_{L,1} + k_{L,1}\theta_h - k_{L,2}\theta_{L,2} \\
\frac{\partial V}{\partial \theta_{L,s}} &= k_{L,s}(\theta_{L,s} - \theta_{L,s-1}) - k_{L,s+1}(\theta_{L,s+1} - \theta_{L,s}), 1 < s < n \\
&= (k_{L,s+1} + k_{L,s})\theta_{L,s} - k_{L,s}\theta_{L,s-1} - k_{L,s+1}\theta_{L,s+1}, 1 < s < n \\
\frac{\partial V}{\partial \theta_{L,n}} &= k_{L,n}(\theta_{L,n} - \theta_{L,n-1}) \\
&= k_{L,n}\theta_{L,n} - k_{L,n}\theta_{L,n-1} \\
\frac{\partial V}{\partial \theta_{R,1}} &= k_{R,1}(\theta_{R,1} - \theta_h) - k_{R,2}(\theta_{R,2} - \theta_{R,1}) \\
&= (k_{R,2} + k_{R,1})\theta_{R,1} - k_{R,1}\theta_h - k_{R,2}\theta_{R,2} \\
\frac{\partial V}{\partial \theta_{R,s}} &= k_{R,s}(\theta_{R,s} - \theta_{R,s-1}) - k_{R,s+1}(\theta_{R,s+1} - \theta_{R,s}), 1 < s < n \\
&= (k_{R,s+1} + k_{R,s})\theta_{R,s} - k_{R,s}\theta_{R,s-1} - k_{R,s+1}\theta_{R,s+1}, 1 < s < n \\
\frac{\partial V}{\partial \theta_{R,n}} &= k_{R,n}(\theta_{R,n} - \theta_{R,n-1}) \\
&= k_{R,n}\theta_{R,n} - k_{R,n}\theta_{R,n-1}
\end{aligned}$$

Using the same matrix formulation as for the limb model

$$\frac{\partial V}{\partial \mathbf{q}} = K\mathbf{q}$$

Where the stiffness matrix, K, is defined as a block matrix below, with the sub matrix definitions

following

$$K = \begin{bmatrix} K_L & 0_{nx2} & K_{L,h}^T & 0_{nxn} \\ 0_{2xn} & 0_{2x2} & 0 & 0_{2xn} \\ K_{L,h} & 0_{1x2} & (k_{L,1} + k_{R,1}) & K_{R,h} \\ 0_{nxn} & 0_{nx2} & K_{R,h}^T & K_R \end{bmatrix}$$

K_L and K_R are of size nxn, while $K_{L,h}$ and $K_{R,h}$ are $1xn$.

$$K_L = \begin{bmatrix} k_{L,n} & -k_{L,n} & 0 & ... & 0 \\ -k_{L,n} & k_{L,n} + k_{L,n-1} & -k_{L,n-1} & ... & 0 \\ \vdots & \vdots & \ddots & & \vdots \\ 0 & 0 & ... & k_{L,3} + k_{L,2} & -k_{L,2} \\ 0 & 0 & ... & -k_{L,2} & k_{L,2} + k_{L,1} \end{bmatrix}$$

$$K_{L,h} = \begin{bmatrix} 0 & ... & 0 & k_{L,1} \end{bmatrix}$$

$$K_R = \begin{bmatrix} k_{R,1} + k_{R,2} & -k_{R,2} & 0 & ... & 0 \\ -k_{R,2} & k_{R,2} + k_{R,3} & -k_{R,3} & ... & 0 \\ \vdots & \vdots & \ddots & & \vdots \\ 0 & 0 & ... & k_{R,n-1} + k_{R,n} & -k_{R,n} \\ 0 & 0 & ... & -k_{R,n} & k_{R,n} \end{bmatrix}$$

$$K_{R,h} = \begin{bmatrix} -k_{R,1} & 0 & ... & 0 \end{bmatrix}$$

A similar set of partials is taken for the damping function with respect to the generalized rates,

$$\begin{aligned}
\frac{\partial D}{\partial \dot{x}} &= 0 \\
\frac{\partial D}{\partial \dot{y}} &= 0 \\
\frac{\partial D}{\partial \dot{\theta}_h} &= c_{L,1}(\dot{\theta}_{L,1} + \dot{\theta}_h) - c_{R,1}(\dot{\theta}_{R,1} - \dot{\theta}_h) \\
&= (c_{L,1} + c_{R,1})\dot{\theta}_h + c_{L,1}\dot{\theta}_{L,1} - c_{R,1}\dot{\theta}_{R,1} \\
\frac{\partial D}{\partial \dot{\theta}_{L,1}} &= c_{L,1}(\dot{\theta}_{L,1} + \dot{\theta}_h) - c_{L,2}(\dot{\theta}_{L,2} - \dot{\theta}_{L,1}) \\
&= (c_{L,2} + c_{L,1})\dot{\theta}_{L,1} + c_{L,1}\dot{\theta}_h - c_{L,2}\dot{\theta}_{L,2} \\
\frac{\partial D}{\partial \dot{\theta}_{L,s}} &= c_{L,s}(\dot{\theta}_{L,s} - \dot{\theta}_{L,s-1}) - c_{L,s+1}(\dot{\theta}_{L,s+1} - \dot{\theta}_{L,s}), 1 < s < n \\
&= (c_{L,s+1} + c_{L,s})\dot{\theta}_{L,s} - c_{L,s}\dot{\theta}_{L,s-1} - c_{L,s+1}\dot{\theta}_{L,s+1}, 1 < s < n \\
\frac{\partial D}{\partial \dot{\theta}_{L,n}} &= c_{L,n}(\dot{\theta}_{L,n} - \dot{\theta}_{L,n-1}) \\
&= c_{L,n}\dot{\theta}_{L,n} - c_{L,n}\dot{\theta}_{L,n-1} \\
\frac{\partial D}{\partial \dot{\theta}_{R,1}} &= c_{R,1}(\dot{\theta}_{R,1} - \dot{\theta}_h) - c_{R,2}(\dot{\theta}_{R,2} - \dot{\theta}_{R,1}) \\
&= (c_{R,2} + c_{R,1})\dot{\theta}_{R,1} - c_{R,1}\dot{\theta}_h - c_{R,2}\dot{\theta}_{R,2} \\
\frac{\partial D}{\partial \dot{\theta}_{R,s}} &= c_{R,s}(\dot{\theta}_{R,s} - \dot{\theta}_{R,s-1}) - c_{R,s+1}(\dot{\theta}_{R,s+1} - \dot{\theta}_{R,s}), 1 < s < n \\
&= (c_{R,s+1} + c_{R,s})\dot{\theta}_{R,s} - c_{R,s}\dot{\theta}_{R,s-1} - c_{R,s+1}\dot{\theta}_{R,s+1}, 1 < s < n \\
\frac{\partial D}{\partial \dot{\theta}_{R,n}} &= c_{R,n}(\dot{\theta}_{R,n} - \dot{\theta}_{R,n-1}) \\
&= c_{R,n}\dot{\theta}_{R,n} - c_{R,n}\dot{\theta}_{R,n-1}
\end{aligned}$$

Using the same matrix formulation as for the limb model

$$\frac{\partial D}{\partial \mathbf{q}} = C_D\mathbf{q}$$

Where the stiffness matrix, C_D, is defined as a block matrix below, with the sub matrix definitions

following

$$C_D = \begin{bmatrix} C_{D_L} & 0_{nx2} & C_{D_{L,h}}^T & 0_{nxn} \\ 0_{2xn} & 0_{2x2} & 0 & 0_{2xn} \\ C_{D_{L,h}} & 0_{1x2} & (c_{L,1} + c_{R,1}) & C_{D_{R,h}} \\ 0_{nxn} & 0_{nx2} & C_{D_{R,h}}^T & C_{D_R} \end{bmatrix}$$

C_{D_L} and C_{D_R} are of size nxn, while $C_{D_{L,h}}$ and $C_{D_{R,h}}$ are $1xn$.

$$C_{D_L} = \begin{bmatrix} c_{L,n} & -c_{L,n} & 0 & ... & 0 \\ -c_{L,n} & c_{L,n} + c_{L,n-1} & -c_{L,n-1} & ... & 0 \\ \vdots & \vdots & \ddots & & \vdots \\ 0 & 0 & ... & c_{L,3} + c_{L,2} & -c_{L,2} \\ 0 & 0 & ... & -c_{L,2} & c_{L,2} + c_{L,1} \end{bmatrix}$$

$$C_{D_{L,h}} = \begin{bmatrix} 0 & ... & 0 & c_{L,1} \end{bmatrix}$$

$$C_{D_R} = \begin{bmatrix} c_{R,1} + c_{R,2} & -c_{R,2} & 0 & ... & 0 \\ -c_{R,2} & c_{R,2} + c_{R,3} & -c_{R,3} & ... & 0 \\ \vdots & \vdots & \ddots & & \vdots \\ 0 & 0 & ... & c_{R,n-1} + c_{R,n} & -c_{R,n} \\ 0 & 0 & ... & -c_{R,n} & c_{R,n} \end{bmatrix}$$

$$C_{D_{R,h}} = \begin{bmatrix} -c_{R,1} & 0 & ... & 0 \end{bmatrix}$$

Now that the potential and damping function are complete, the next step is the kinetic energy partials. To do this, new velocities is defined for the kinetic energy equation in terms of the states. The hub mass velocities, from which all others build, is defined below.

$$\boldsymbol{v_h} = (\dot{x})\hat{\imath} + (\dot{y})\hat{\jmath}$$

The left link i^{th} velocity is defined as follows. For the $i = 1$ case, the summation is ignored

$$\boldsymbol{v_{L,i}} = \big(\dot{x} + d_L\dot{\theta}_h \sin(\theta_h + \phi_L) + l_{c_{L,i}}\dot{\theta}_{L,i}\sin(\theta_{L,i}) + \sum_{j=1}^{i-1} l_{L,j}\dot{\theta}_{L,j}\sin(\theta_{L,j})\big)\hat{\imath} \\ + \big(\dot{y} - d_L\dot{\theta}_h\cos(\theta_h + \phi_L) + l_{c_{L,i}}\dot{\theta}_{L,i}\cos(\theta_{L,i}) + \sum_{j=1}^{i-1} l_{L,j}\dot{\theta}_{L,j}\cos(\theta_{L,j})\big)\hat{\jmath}$$

The right link i^{th} velocity is defined as follows. As with the left link, the summation is ignored when $i = 1$.

$$\boldsymbol{v_{R,i}} = \big(\dot{x} - d_R\dot{\theta}_h \sin(\theta_h - \phi_R) - l_{c_{R,i}}\dot{\theta}_{R,i}\sin(\theta_{R,i}) - \sum_{j=1}^{i-1} l_{L,j}\dot{\theta}_{R,j}\sin(\theta_{R,j})\big)\hat{\imath} \\ + \big(\dot{y} + d_R\dot{\theta}_h\cos(\theta_h - \phi_R) + l_{c_{R,i}}\dot{\theta}_{R,i}\cos(\theta_{R,i}) + \sum_{j=1}^{i-1} l_{R,j}\dot{\theta}_{R,j}\cos(\theta_{R,j})\big)\hat{\jmath}$$

Starting with the derivative with respect to the generalized rates it follows that for any of the rates, the trend must follow the form below.

$$\frac{\partial T}{\partial \dot{q}_s} = \Big(m_h\mathbf{v}_h \cdot \frac{\partial \mathbf{v}_h}{\dot{q}_s} + I_h\dot{\theta}_h \cdot \frac{\partial\dot{\theta}_h}{\dot{q}_s} + \sum_{i=1}^{n}\big[m_{L,i}\mathbf{v}_{L,i}\cdot\frac{\partial\mathbf{v}_{L,i}}{\dot{q}_s} + I_{L,i}\dot{\theta}_{L,i}\cdot\frac{\partial\dot{\theta}_{L,i}}{\dot{q}_s} \\ + m_{R,i}\mathbf{v}_{R,i}\cdot\frac{\partial\mathbf{v}_{R,i}}{\dot{q}_s} + I_{R,i}\dot{\theta}_{R,i}\cdot\frac{\partial\dot{\theta}_{R,i}}{\dot{q}_s}\big]\Big) \quad (3.1)$$

For the partials of the angular rates, it is easy to see that they are zero for all cases except when the generalized rate is that angular rate. The velocity partials are less obvious, so starting with the hub velocity

$$\frac{\partial\mathbf{v}_h}{\partial\dot{x}} = 1\hat{\imath}$$
$$\frac{\partial\mathbf{v}_h}{\partial\dot{y}} = 1\hat{\jmath}$$
$$\frac{\partial\mathbf{v}_h}{\partial\dot{\theta}_h} = 0$$
$$\frac{\partial\mathbf{v}_h}{\partial\theta_{L,s}} = 0,\ \forall\ s$$
$$\frac{\partial\mathbf{v}_h}{\partial\dot{\theta}_{R,s}} = 0,\ \forall\ s$$

For the left link velocities,

$$\frac{\partial \mathbf{v}_{L,i}}{\partial \dot{x}} = 1\hat{\imath},\ \forall\ i$$
$$\frac{\partial \mathbf{v}_{L,i}}{\partial \dot{y}} = 1\hat{\jmath},\ \forall\ i$$
$$\frac{\partial \mathbf{v}_{L,i}}{\partial \dot{\theta}_h} = \big(d_L \sin(\theta_h + \phi_L)\big)\hat{\imath} - \big(d_L \cos(\theta_h + \phi_L)\big)\hat{\jmath}$$
$$\frac{\partial \mathbf{v}_{L,i}}{\partial \dot{\theta}_{L,s}} = \begin{cases} 0 & s > i \\ (l_{c_{L,s}} \sin(\theta_{L,s}))\hat{\imath} + (l_{c_{L,s}} \cos(\theta_{L,s}))\hat{\jmath} & s = i \\ (l_{L,s} \sin(\theta_{L,s}))\hat{\imath} + (l_{L,s} \cos(\theta_{L,s}))\hat{\jmath} & s < i \end{cases}$$
$$\frac{\partial \mathbf{v}_{L,i}}{\partial \dot{\theta}_{R,s}} = 0,\ \forall\ i,\ s$$

and the same for the right velocities

$$\frac{\partial \mathbf{v}_{L,i}}{\partial \dot{x}} = 1\hat{\imath},\ \forall\ i$$
$$\frac{\partial \mathbf{v}_{L,i}}{\partial \dot{y}} = 1\hat{\jmath},\ \forall\ i$$
$$\frac{\partial \mathbf{v}_{L,i}}{\partial \dot{\theta}_h} = -\big(d_R \sin(\theta_h - \phi_R)\big)\hat{\imath} + \big(d_R \cos(\theta_h - \phi_R)\big)\hat{\jmath}$$
$$\frac{\partial \mathbf{v}_{R,i}}{\partial \dot{\theta}_{L,s}} = 0,\ \forall\ i,\ s$$
$$\frac{\partial \mathbf{v}_{R,i}}{\partial \dot{\theta}_{R,s}} = \begin{cases} 0 & s > i \\ -(l_{c_{R,s}} \sin(\theta_{R,s}))\hat{\imath} + (l_{c_{R,s}} \cos(\theta_{R,s}))\hat{\jmath} & s = i \\ -(l_{R,s} \sin(\theta_{R,s}))\hat{\imath} + (l_{R,s} \cos(\theta_{R,s}))\hat{\jmath} & s < i \end{cases}$$

Plugging in these partials for each generalized rate and evaluating any dot products, and obtaining the solutions below. Starting with the x velocity,

$$\frac{\partial T}{\partial \dot{x}} = m_h \mathbf{v}_h \cdot (1\hat{\imath}) + \sum_{i=1}^{n} \left[m_{L,i} \mathbf{v}_{L,i} \cdot (1\hat{\imath}) + m_{R,i} \mathbf{v}_{R,i} \cdot (1\hat{\imath}) \right]$$

$$= m_h\dot{x} + \sum_{i=1}^{n}\Big[m_{L,i}\Big(\dot{x} + d_L\dot{\theta}_h\sin(\theta_h+\phi_L) + l_{c_{L,i}}\dot{\theta}_{L,i}\sin(\theta_{L,i}) + \sum_{j=1}^{i-1}\big[l_{L,j}\dot{\theta}_{L,j}\sin(\theta_{L,j})\big]\Big)$$
$$+ m_{R,i}\Big(\dot{x} - d_R\dot{\theta}_h\sin(\theta_h-\phi_R) - l_{c_{R,i}}\dot{\theta}_{R,i}\sin(\theta_{R,i}) - \sum_{j=1}^{i-1}\big[l_{L,j}\dot{\theta}_{R,j}\sin(\theta_{R,j})\big]\Big)\Big]$$

$$= \Big(m_h + \sum_{i=1}^{n}[m_{L,i}+m_{R,i}]\Big)\dot{x} + \Big(d_L\sin(\theta_h+\phi_L)sum_{i=1}^{n}[m_{L,i}] - d_R\sin(\theta_h-\phi_R)\sum_{i=1}^{n}[m_{R,i}]\Big)\dot{\theta}_h$$
$$+ \sum_{i=1}^{n}\Big[\sin(\theta_{L,i})\Big(l_{c_{L,i}}m_{L,i} + l_{L,i}\sum_{j=i+1}^{n}[m_{L,j}]\Big)\dot{\theta}_{L,i} - \sin(\theta_{R,i})\Big(l_{c_{R,i}}m_{R,i} + l_{R,i}\sum_{j=i+1}^{n}[m_{R,j}]\Big)\dot{\theta}_{R,i}\Big] \tag{3.2}$$

Now with the partial with respect to the x velocity, taking the time derivative yields the equation below.

$$\frac{\mathrm{d}}{\mathrm{d}t}\frac{\partial T}{\partial\dot{x}} = \Big(m_h + \sum_{i=1}^{n}[m_{L,i}+m_{R,i}]\Big)\ddot{x}$$
$$+ \Big(d_L\sin(\theta_h+\phi_L)sum_{i=1}^{n}[m_{L,i}] - d_R\sin(\theta_h-\phi_R)\sum_{i=1}^{n}[m_{R,i}]\Big)\ddot{\theta}_h$$
$$+ \sum_{i=1}^{n}\Big[\sin(\theta_{L,i})\Big(l_{c_{L,i}}m_{L,i} + l_{L,i}\sum_{j=i+1}^{n}[m_{L,j}]\Big)\ddot{\theta}_{L,i} - \sin(\theta_{R,i})\Big(l_{c_{R,i}}m_{R,i} + l_{R,i}\sum_{j=i+1}^{n}[m_{R,j}]\Big)\ddot{\theta}_{R,i}\Big]$$
$$+ \Big(d_L\cos(\theta_h+\phi_L)sum_{i=1}^{n}[m_{L,i}] - d_R\cos(\theta_h-\phi_R)\sum_{i=1}^{n}[m_{R,i}]\Big)\dot{\theta}_h^2$$
$$+ \sum_{i=1}^{n}\Big[\cos(\theta_{L,i})\Big(l_{c_{L,i}}m_{L,i} + l_{L,i}\sum_{j=i+1}^{n}[m_{L,j}]\Big)\dot{\theta}_{L,i}^2 - \cos(\theta_{R,i})\Big(l_{c_{R,i}}m_{R,i} + l_{R,i}\sum_{j=i+1}^{n}[m_{R,j}]\Big)\dot{\theta}_{R,i}^2\Big] \tag{3.3}$$

Following the same process for the y velocity,

$$\frac{\partial T}{\partial\dot{y}} = m_h\mathbf{v}_h\cdot(1\hat{j}) + \sum_{i=1}^{n}\big[m_{L,i}\mathbf{v}_{L,i}\cdot(1\hat{j}) + m_{R,i}\mathbf{v}_{R,i}\cdot(1\hat{j})\big]$$

$$= \Big(m_h + \sum_{i=1}^{n}[m_{L,i}+m_{R,i}]\Big)\dot{y} + \Big(-d_L\cos(\theta_h+\phi_L)\sum_{i=1}^{n}[m_{L,i}] + d_R\cos(\theta_h-\phi_R)\sum_{i=1}^{n}[m_{R,i}]\Big)\dot{\theta}_h$$
$$+ \sum_{i=1}^{n}\Big[\cos(\theta_{L,i})\Big(l_{c_{L,i}}m_{L,i} + l_{L,i}\sum_{j=i+1}^{n}[m_{L,j}]\Big)\dot{\theta}_{L,i} + \cos(\theta_{R,i})\Big(l_{c_{R,i}}m_{R,i} + l_{R,i}\sum_{j=i+1}^{n}[m_{R,j}]\Big)\dot{\theta}_{R,i}\Big] \tag{3.4}$$

Applying the time derivative,

$$\begin{aligned}\frac{\mathrm{d}}{\mathrm{d}t}\frac{\partial T}{\partial \dot{y}} = &\Big(m_h + \sum_{i=1}^{n}[m_{L,i} + m_{R,i}]\Big)\ddot{y} \\ &+ \Big(- d_L\cos(\theta_h + \phi_L)\sum_{i=1}^{n}[m_{L,i}] + d_R\cos(\theta_h - \phi_R)\sum_{i=1}^{n}[m_{R,i}]\Big)\ddot{\theta}_h \\ + \sum_{i=1}^{n}\Big[&\cos(\theta_{L,i})\Big(l_{c_{L,i}}m_{L,i} + l_{L,i}\sum_{j=i+1}^{n}[m_{L,j}]\Big)\ddot{\theta}_{L,i} + \cos(\theta_{R,i})\Big(l_{c_{R,i}}m_{R,i} + l_{R,i}\sum_{j=i+1}^{n}[m_{R,j}]\Big)\ddot{\theta}_{R,i}\Big] \\ &+ \Big(d_L\sin(\theta_h + \phi_L)\sum_{i=1}^{n}[m_{L,i}] - d_R\sin(\theta_h - \phi_R)\sum_{i=1}^{n}[m_{R,i}]\Big)\dot{\theta}_h^2 \\ - \sum_{i=1}^{n}\Big[&\cos(\theta_{L,i})\Big(l_{c_{L,i}}m_{L,i} + l_{L,i}\sum_{j=i+1}^{n}[m_{L,j}]\Big)\dot{\theta}_{L,i}^2 + \cos(\theta_{R,i})\Big(l_{c_{R,i}}m_{R,i} + l_{R,i}\sum_{j=i+1}^{n}[m_{R,j}]\Big)\dot{\theta}_{R,i}^2\Big]\end{aligned} \tag{3.5}$$

Moving on to the hub rate, $\dot{\theta}_h$,

$$\begin{aligned}\frac{\partial T}{\partial \dot{\theta}_h} &= I_h\dot{\theta}_h + \sum_{i=1}^{n}\Big[m_{L,i}\mathbf{v}_{L,i}\cdot\big[\big(d_L\sin(\theta_h + \phi_L)\big)\hat{\imath} - \big(d_L\cos(\theta_h + \phi_L)\big)\hat{\jmath}\big] \\ &\qquad + m_{R,i}\mathbf{v}_{R,i}\cdot\big[-\big(d_R\sin(\theta_h - \phi_R)\big)\hat{\imath} + \big(d_R\cos(\theta_h - \phi_R)\big)\hat{\jmath}\big]\Big] \\ &= I_h\dot{\theta}_h + \sum_{i=1}^{n}\Big[m_{L,i}\mathbf{v}_{L,i}\cdot\big[\big(d_L\sin(\theta_h + \phi_L)\big)\hat{\imath} - \big(d_L\cos(\theta_h + \phi_L)\big)\hat{\jmath}\big] \\ &\qquad + m_{R,i}\mathbf{v}_{R,i}\cdot\big[-\big(d_R\sin(\theta_h - \phi_R)\big)\hat{\imath} + \big(d_R\cos(\theta_h - \phi_R)\big)\hat{\jmath}\big]\Big] \\ &= \Big(I_h + \sum_{i=1}^{n}[m_{L,i}]d_L^2 + \sum_{i=1}^{n}[m_{R,i}]d_R^2\Big)\dot{\theta}_h + \sum_{i=1}^{n}\Big[m_{L,i}d_L\big[\big(\dot{x}\sin(\theta_h + \phi_L) - \dot{y}\cos(\theta_h + \phi_L) \\ &\qquad + l_{c_{L,i}}\cos(\theta_h + \theta_{L,i} + \phi_L)\dot{\theta}_{L,i} + \sum_{j=1}^{i-1}[l_{L,j}\cos(\theta_h + \theta_{L,j} + \phi_L)\dot{\theta}_{L,j}]\big)\big] \\ &\qquad + m_{R,i}d_R\big[\big(-\dot{x}\sin(\theta_h - \phi_R) + \dot{y}\cos(\theta_h - \phi_R) \\ &\qquad + l_{c_{R,i}}\cos(\theta_h - \theta_{R,i} - \phi_R)\dot{\theta}_{R,i} + \sum_{j=1}^{i-1}[l_{R,j}\cos(\theta_h - \theta_{R,j} - \phi_R)\dot{\theta}_{R,j}]\big)\big]\Big]\end{aligned}$$

Taking the time derivative,

$$\begin{aligned}\frac{\mathrm{d}}{\mathrm{d}t}\frac{\partial T}{\partial \dot{\theta}_h} = &\Big(I_h+\sum_{i=1}^{n}[m_{L,i}]d_L^2+\sum_{i=1}^{n}[m_{R,i}]d_R^2\Big)\ddot{\theta}_h+\Big(\sum_{i=1}^{n}[m_{L,i}]d_L\sin(\theta_h+\phi_L)-\sum_{i=1}^{n}[m_{R,i}]d_R\sin(\theta_h-\phi_R)\Big)\ddot{x}\\
&+\Big(-\sum_{i=1}^{n}[m_{L,i}]d_L\cos(\theta_h+\phi_L)+\sum_{i=1}^{n}[m_{R,i}]d_R\cos(\theta_h-\phi_R)\Big)\ddot{y}\\
&+\sum_{i=1}^{n}\Big[d_L\Big(l_{c_{L,i}}m_{L,i}+l_{L,i}\sum_{j=i+1}^{n}[m_{L,j}]\Big)\cos(\theta_h+\theta_{L,i}+\phi_L)\ddot{\theta}_{L,i}\\
&+d_R\Big(l_{c_{R,i}}m_{R,i}+l_{R,i}\sum_{j=i+1}^{n}[m_{R,j}]\Big)\cos(\theta_h-\theta_{R,i}-\phi_R)\ddot{\theta}_{R,i}\Big]\\
&+\Big(\sum_{i=1}^{n}[m_{L,i}]d_L\cos(\theta_h+\phi_L)-\sum_{i=1}^{n}[m_{R,i}]d_R\cos(\theta_h-\phi_R)\Big)\dot{x}\dot{\theta}_h\\
&+\Big(\sum_{i=1}^{n}[m_{L,i}]d_L\sin(\theta_h+\phi_L)-\sum_{i=1}^{n}[m_{R,i}]d_R\sin(\theta_h-\phi_R)\Big)\dot{y}\dot{\theta}_h\\
&-\sum_{i=1}^{n}\Big[d_L\Big(l_{c_{L,i}}m_{L,i}+l_{L,i}\sum_{j=i+1}^{n}[m_{L,j}]\Big)\sin(\theta_h+\theta_{L,i}+\phi_L)(\dot{\theta}_h+\dot{\theta}_{L,i})\dot{\theta}_{L,i}\\
&+d_R\Big(l_{c_{R,i}}m_{R,i}+l_{R,i}\sum_{j=i+1}^{n}[m_{R,j}]\Big)\sin(\theta_h-\theta_{R,i}-\phi_R)(\dot{\theta}_h-\dot{\theta}_{R,i})\dot{\theta}_{R,i}\Big] \quad (3.6)\end{aligned}$$

The process for the left link angular rates is similar to the hub rate, as shown below

$$\begin{aligned}\frac{\partial T}{\partial \dot{\theta}_{L,s}} &= I_{L,s}\dot{\theta}_{L,s}+m_{L,s}\mathbf{v}_{L,s}\cdot\big[\big(l_{c_{L,s}}\sin(\theta_{L,s})\big)\hat{\imath}+\big(l_{c_{L,s}}\cos(\theta_{L,s})\big)\hat{\jmath}\big]\\
&\quad+\sum_{i=s+1}^{n}\Big[m_{L,i}\mathbf{v}_{L,i}\cdot\big[\big(l_{L,s}\sin(\theta_{L,s})\big)\hat{\imath}+\big(l_{L,s}\cos(\theta_{L,s})\big)\hat{\jmath}\big]\Big]\end{aligned}$$

$$\begin{aligned}&= I_i\dot{\theta}_{L,s}+m_{L,s}\Big(l_{c_{L,s}}^2\dot{\theta}_{L,s}+l_{c_{L,s}}\big(\dot{x}\sin(\theta_{L,s})+\dot{y}\cos(\theta_{L,s})+d_L cos(\theta_h+\theta_{L,s}+\phi_L)\dot{\theta}_h\\
&\quad+\sum_{i=1}^{s-1}[l_i\cos(\theta_i-\theta_{L,s})\dot{\theta}_i]\big)\Big)+l_{L,s}\Big(\dot{x}\sin(\theta_{L,s})+\dot{y}\cos(\theta_{L,s})+d_L cos(\theta_h+\theta_{L,s}+\phi_L)\dot{\theta}_h\\
&\quad+\sum_{i=s+1}^{n}\Big[m_i\big(l_{c_i}\cos(\theta_i-\theta_{L,s})\dot{\theta}_i+\sum_{j=1}^{i-1}[l_j\cos(\theta_j-\theta_{L,s})\dot{\theta}_j]\big)\Big]\Big)\end{aligned}$$

$$\begin{aligned}&= I_i\dot{\theta}_{L,s}+m_{L,s}l_{c_{L,s}}^2\dot{\theta}_{L,s}+\Big(l_{c_{L,s}}m_{L,s}+l_{L,s}\sum_{i=s+1}^{n}[m_i]\Big)\Big(\dot{x}\sin(\theta_{L,s})+\dot{y}\cos(\theta_{L,s})+d_L cos(\theta_h+\theta_{L,s}+\phi_L)\dot{\theta}_h\\
&\quad+\sum_{i=1}^{s-1}[l_i\cos(\theta_i-\theta_{L,s})\dot{\theta}_i]\Big)+l_{L,s}\sum_{i=s+1}^{n}\Big[\big(l_{c_i}m_i+l_i\sum_{j=i+1}^{n}[m_j]\big)\cos(\theta_i-\theta_{L,s})\dot{\theta}_i\Big]\end{aligned}$$

Now, evaluating the time derivative on this term, thus obtaining

$$\frac{\mathrm{d}}{\mathrm{d}t}\frac{\partial T}{\partial \dot{\theta}_{L,s}} = (I_{L,s} + m_{L,s}l_{c_{L,s}}^2)\ddot{\theta}_{L,s} + \Big(l_{c_{L,s}}m_{L,s} + l_{L,s}\sum_{i=s+1}^{n}[m_i]\Big)\Big(\ddot{x}\sin(\theta_{L,s}) + \ddot{y}\cos(\theta_{L,s})$$
$$+ d_L cos(\theta_h + \theta_{L,s} + \phi_L)\ddot{\theta}_h + \sum_{i=1}^{s-1}[l_i\cos(\theta_i - \theta_{L,s})\ddot{\theta}_i]\Big) + l_{L,s}\sum_{i=s+1}^{n}\Big[\Big(l_{c_i}m_i + l_i\sum_{j=i+1}^{n}[m_j]\Big)\cos(\theta_i - \theta_{L,s})\ddot{\theta}_i\Big]$$
$$- \Big(l_{c_{L,s}}m_{L,s} + l_{L,s}\sum_{i=s+1}^{n}[m_i]\Big)\Big(\dot{x}\dot{\theta}_{L,s}\cos(\theta_{L,s}) + \dot{y}\dot{\theta}_{L,s}\sin(\theta_{L,s}) + d_L\sin(\theta_h + \theta_{L,s} + \phi_L)(\dot{\theta}_h + \dot{\theta}_{L,s})\dot{\theta}_h$$
$$+ \sum_{i=1}^{s-1}[l_i\sin(\theta_i - \theta_{L,s})(\dot{\theta}_i - \dot{\theta}_{L,s})\dot{\theta}_i]\Big) - l_{L,s}\sum_{i=s+1}^{n}\Big[\Big(l_{c_i}m_i + l_i\sum_{j=i+1}^{n}[m_j]\Big)\sin(\theta_i - \theta_{L,s})(\dot{\theta}_i - \dot{\theta}_{L,s})\dot{\theta}_i\Big] \tag{3.7}$$

Finally, for the right hand links,

$$\frac{\mathrm{d}}{\mathrm{d}t}\frac{\partial T}{\partial \dot{\theta}_{R,s}} = (I_{R,s} + m_{R,s}l_{c_{R,s}}^2)\ddot{\theta}_{R,s} + \Big(l_{c_{R,s}}m_{R,s} + l_{R,s}\sum_{i=s+1}^{n}[m_i]\Big)\Big(\ddot{x}\sin(\theta_{R,s}) + \ddot{y}\cos(\theta_{R,s})$$
$$+ d_R cos(\theta_h + \theta_{R,s} + \phi_R)\ddot{\theta}_h + \sum_{i=1}^{s-1}[l_i\cos(\theta_i - \theta_{R,s})\ddot{\theta}_i]\Big) + l_{R,s}\sum_{i=s+1}^{n}\Big[\Big(l_{c_i}m_i + l_i\sum_{j=i+1}^{n}[m_j]\Big)\cos(\theta_i - \theta_{R,s})\ddot{\theta}_i\Big]$$
$$- \Big(l_{c_{R,s}}m_{R,s} + l_{R,s}\sum_{i=s+1}^{n}[m_i]\Big)\Big(\dot{x}\dot{\theta}_{R,s}\cos(\theta_{R,s}) + \dot{y}\dot{\theta}_{R,s}\sin(\theta_{R,s}) + d_R\sin(\theta_h + \theta_{R,s} + \phi_R)(\dot{\theta}_h + \dot{\theta}_{R,s})\dot{\theta}_h$$
$$+ \sum_{i=1}^{s-1}[l_i\sin(\theta_i - \theta_{R,s})(\dot{\theta}_i - \dot{\theta}_{R,s})\dot{\theta}_i]\Big) - l_{R,s}\sum_{i=s+1}^{n}\Big[\Big(l_{c_i}m_i + l_i\sum_{j=i+1}^{n}[m_j]\Big)\sin(\theta_i - \theta_{R,s})(\dot{\theta}_i - \dot{\theta}_{R,s})\dot{\theta}_i\Big] \tag{3.8}$$

Like in the limb only model, these terms can now be grouped into a matrix form, such that

$$\frac{\mathrm{d}}{\mathrm{d}t}\frac{\partial T}{\partial \dot{\mathbf{q}}} = M\ddot{\mathbf{q}} + C_{m,1}\dot{\mathbf{q}} \tag{3.9}$$

Given the number of and complexity of terms in these matrices, a general block form is shown, then the equations for individual terms are shown in an element-wise equation format. The block mass matrix is as follows,

$$M = \begin{bmatrix} M_L & M_{L,h}^T & 0_{nxn} \\ M_{L,h} & M_h & M_{R,h} \\ 0_{nxn} & M_{R,h}^T & M_R \end{bmatrix}$$

M_L and M_R are of size nxn, $M_{L,h}$ and $M_{R,h}$ are $3xn$, and M_h is $3x3$. The mass damping matrix is constructed similarly,

$$C_{m,1} = \begin{bmatrix} C_{m,1_L} & C^T_{m,1_{L,h}} & 0_{nxn} \\ C_{m,1_{L,h}} & C_{m,1_h} & C_{m,1_{R,h}} \\ 0_{nxn} & C^T_{m,1_{R,h}} & C_{m,1_R} \end{bmatrix}$$

$C_{m,1_L}$ and $C_{m,1_R}$ are of size nxn, $C_{m,1_{L,h}}$ and $C_{m,1_{R,h}}$ are $3xn$, and $C_{m,1_h}$ is $3x3$. Using the same process as above for the generalized rates, the most generic form of the kinetic energy equation with respect to an arbitrary generalized coordinate, q_s, is expressed below.

$$\frac{\partial T}{\partial q_s} = m_h v_h \frac{\partial v_h}{\partial q_s} + I_h \dot{\theta}_h \frac{\partial \dot{\theta}_h}{\partial q_s} + \sum_{i=1}^{n} m_{L,i} v_{L,i} \frac{\partial v_{L,i}}{\partial q_s} + I_{L,i} \dot{\theta}_{L,i} \frac{\partial \dot{\theta}_{L,i}}{\partial q_s} + m_{R,i} v_{R,i} \frac{\partial v_{R,i}}{\partial q_s} + I_{R,i} \dot{\theta}_{R,i} \frac{\partial \dot{\theta}_{R,i}}{\partial q_s}$$

Simplifying the earlier equation for the partial of kinetic energy with respect to the positions. All angular rate terms, as well as the hub mass velocity, can be ignored, since those terms do not contain any of the generalized coordinates, leaving only the left and right limb mass velocities.

$$\frac{\partial T}{\partial q_s} = \sum_{i=1}^{n} m_{L,i} \mathbf{v}_{L,i} \cdot \frac{\partial \mathbf{v}_{L,i}}{\partial q_s} + m_{R,i} \mathbf{v}_{R,i} \cdot \frac{\partial \mathbf{v}_{R,i}}{\partial q_s}$$

The partials of the i^{th} left limb velocity for each of generalized coordinates are shown below.

$$\frac{\partial \mathbf{v}_{L,i}}{\partial x} = 0, \ \forall \ i$$

$$\frac{\partial \mathbf{v}_{L,i}}{\partial y} = 0, \ \forall \ i$$

$$\frac{\partial \mathbf{v}_{L,i}}{\partial \theta_h} = \big(d_L \dot{\theta}_h \cos(\theta_h + \phi_L)\big)\hat{\imath} + \big(d_L \dot{\theta}_h \sin(\theta_h + \phi_L)\big)\hat{\jmath}$$

$$\frac{\partial \mathbf{v}_{L,i}}{\partial \theta_{L,s}} = \begin{cases} 0 & s > i \\ (l_{c_{L,s}} \dot{\theta}_{L,s} \cos(\theta_{L,s}))\hat{\imath} - (l_{c_{L,s}} \dot{\theta}_{L,s} \sin(\theta_{L,s}))\hat{\jmath} & s = i \\ (l_{L,s} \dot{\theta}_{L,s} \cos(\theta_{L,s}))\hat{\imath} - (l_{L,s} \dot{\theta}_{L,s} \sin(\theta_{L,s}))\hat{\jmath} & s < i \end{cases}$$

$$\frac{\partial \mathbf{v}_{L,i}}{\partial \theta_{R,s}} = 0, \ \forall \ i, \ s$$

Similarly for the right hand limb velocities,

$$\frac{\partial \mathbf{v}_{R,i}}{\partial x} = 0, \ \forall \ i$$
$$\frac{\partial \mathbf{v}_{R,i}}{\partial y} = 0, \ \forall \ i$$
$$\frac{\partial \mathbf{v}_{R,i}}{\partial \theta_h} = -(d_R \dot{\theta}_h \cos(\theta_h - \phi_R))\hat{\imath} - (d_R \dot{\theta}_h \sin(\theta_h - \phi_R))\hat{\jmath}$$
$$\frac{\partial \mathbf{v}_{R,i}}{\partial \theta_{L,s}} = 0, \ \forall \ i, \ s$$
$$\frac{\partial \mathbf{v}_{R,i}}{\partial \theta_{R,s}} = \begin{cases} 0 & s > i \\ -(l_{c_{R,s}} \dot{\theta}_{R,s} \cos(\theta_{R,s}))\hat{\imath} - (l_{c_{R,s}} \dot{\theta}_{R,s} \sin(\theta_{R,s}))\hat{\jmath} & s = i \\ -(l_{R,s} \dot{\theta}_{R,s} \cos(\theta_{R,s}))\hat{\imath} - (l_{R,s} \dot{\theta}_{R,s} \sin(\theta_{R,s}))\hat{\jmath} & s < i \end{cases}$$

Assembling this for the partial with respect to an arbitrary link angle $\theta_{L,s}$ leads to the term below.

$$\frac{\partial T}{\partial \theta_{L,s}} = \sum_{i=s}^{n} m_{L,i} \mathbf{v}_{L,i} \frac{\partial \mathbf{v}_{L,i}}{\partial \theta_{L,s}}$$

$$= m_{L,s} \mathbf{v}_{L,s} \cdot \left[(l_{c_{L,s}} \dot{\theta}_{L,s} \cos(\theta_{L,s}))\hat{\imath} - (l_{c_{L,s}} \dot{\theta}_{L,s} \sin(\theta_{L,s}))\hat{\jmath} \right] + \sum_{i=s+1}^{n} m_{L,i} v_{L,i} \cdot \left[(l_{L,s} \dot{\theta}_{L,s} \cos(\theta_{L,s}))\hat{\imath} - (l_{L,s} \dot{\theta}_{L,s} \sin(\theta_{L,s}))\hat{\jmath} \right]$$

$$= m_{L,s} l_{c_{L,s}} \dot{\theta}_{L,s} \left[\dot{x} \cos(\theta_{L,s}) - \dot{y} \sin(\theta_{L,s}) + d_L \dot{\theta}_h \sin(\theta_{L,s} + \theta_h + \phi_L) + \sum_{j=1}^{s-1} l_{L,j} \dot{\theta}_{L,j} \sin(\theta_{L,j} - \theta_{L,s}) \right]$$
$$+ \sum_{i=s+1}^{n} \Big[m_{L,i} l_{L,s} \dot{\theta}_{L,s} \Big(\dot{x} \cos(\theta_{L,s}) - \dot{y} \sin(\theta_{L,s}) + d_L \dot{\theta}_h \sin(\theta_{L,s} + \theta_h + \phi_L) + l_{c_{L,i}} \dot{\theta}_{L,i} \sin(\theta_{L,i} - \theta_{L,s}) + \sum_{j=1, j \neq s}^{i-1} l_{L,j} \dot{\theta}_{L,j} \sin(\theta_{L,j} - \theta_{L,s}) \Big) \Big]$$

This results in the equation below

$$= \Bigg[\Big(l_{c_{L,s}} m_{L,s} + l_{L,s} \sum_{i=s+1}^{n} m_{L,i} \Big) \Big(\dot{x} \cos(\theta_{L,s}) - \dot{y} \sin(\theta_{L,s}) + d_L \dot{\theta}_h \sin(\theta_{L,s} + \theta_h + \phi_L) + \sum_{j=1}^{s-1} l_{L,j} \dot{\theta}_{L,j} \sin(\theta_{L,j} - \theta_{L,s}) \Big) + l_{L,s} \Big(\sum_{i=s+1}^{n} m_{L,i} l_{c_{L,i}} \dot{\theta}_{L,i} \sin(\theta_{L,i} - \theta_{L,s}) + \sum_{i=s+2}^{n} \big[m_{L,i} \sum_{j=s+1}^{i-1} \big[l_{L,j} \dot{\theta}_{L,j} \sin(\theta_{L,j} - \theta_{L,s}) \big] \Big) \Bigg] \dot{\theta}_{L,s} \tag{3.10}$$

Similarly for an arbitrary right link angle, $\theta_{R,s}$

$$\frac{\partial T}{\partial \theta_{R,s}} = \sum_{i=s}^{n} m_{R,i} \mathbf{v}_{R,i} \frac{\partial \mathbf{v}_{R,i}}{\partial \theta_{R,s}}$$

$$= \Big(l_{c_{R,s}} m_{R,s} + l_{R,s} \sum_{i=s+1}^{n} m_{R,i} \Big) \Big(\dot{x} \cos(\theta_{R,s}) + \dot{y} \sin(\theta_{R,s}) + d_R \dot{\theta}_h \sin(\theta_{R,s} - \theta_h + \phi_R) + \sum_{j=1}^{s-1} l_{R,j} \dot{\theta}_{R,j} \sin(\theta_{R,s} - \theta_{R,j}) \Big) \dot{\theta}_{R,s} + l_{R,s} \Big(\sum_{i=s+1}^{n} m_{R,i} l_{c_{R,i}} \dot{\theta}_{R,i} \sin(\theta_{R,s} - \theta_{R,i}) + \sum_{i=s+2}^{n} \big[m_{R,i} \sum_{j=s+1}^{i-1} l_{R,j} \dot{\theta}_{R,j} \sin(\theta_{R,s} - \theta_{R,j}) \big] \Big) \dot{\theta}_{R,s} \tag{3.11}$$

Representing these terms in a matrix form as above, such that

$$\frac{\partial T}{\partial \mathbf{q}} = C_{m,2} \dot{\mathbf{q}} \tag{3.12}$$

Where $C_{m,2}$ is defined below.

$$C_{m,2} = \begin{bmatrix} C_{m,2_L} & 0_{nx3} & 0_{nxn} \\ 0_{3xn} & C_{m,2_h} & 0_{3xn} \\ 0_{nxn} & 0_{nx3} & C_{m,2_R} \end{bmatrix}$$

$C_{m,2_L}$ and $C_{m,2_R}$ are of size nxn, and $C_{m,3_h}$ is $3x3$. With these equations, the unforced dynamics for this new system are now fully defined, deriving the various forces present in the model can begin.

3.1.2 Gravitational Forces

To add gravitational forces into the dynamics, the partial of the gravitational potential energy with respect to the generalized coordinates is taken, with the negative of the result being the generalized gravity force, $Q_{s_{\text{grav}}}$. Like with the limb model, a simplistic constant-acceleration gravity model is used here, but more complex models could be added with this same approach.

$$V_{\text{grav}} = \Big(m_h y + \sum_{i=1}^{n} [m_{L,i} y_{m_{L,i}} + m_{R,i} y_{m_{R,i}}]\Big) g$$

For the above equation, $y_{m_{L,i}}$ and $y_{m_{r,i}}$ are defined below

$$y_{m_{L,i}} = y - d_L \sin(\theta_h + \phi_L) + l_{c_{L,i}} \sin(\theta_{L,i}) + \sum_{j=1}^{i-1} l_{L,j} \sin(\theta_{L,j}) \tag{3.13}$$

$$y_{m_{R,i}} = y + d_R \sin(\theta_h - \phi_R) + l_{c_{R,i}} \sin(\theta_{R,i}) + \sum_{j=1}^{i-1} l_{R,j} \sin(\theta_{R,j}) \tag{3.14}$$

Now taking the partials of the potential function

$$\begin{aligned}
\frac{\partial V_{\text{grav}}}{\partial x} &= 0 \\
\frac{\partial V_{\text{grav}}}{\partial y} &= Big(m_h + \sum_{i=1}^{n} [m_{L,i} + m_{R,i}]\Big) \\
\frac{\partial V_{\text{grav}}}{\partial \theta_h} &= g \sum_{i=1}^{n} \Big[m_{L,i} \frac{y_{m_{L,i}}}{\partial \theta_h} + m_{R,i} \frac{y_{m_{R,i}}}{\partial \theta_h}\Big] \\
\frac{\partial V_{\text{grav}}}{\partial \theta_{L,s}} &= g \sum_{i=1}^{n} m_{L,i} \frac{y_{m_{L,i}}}{\partial \theta_{L,s}} \\
\frac{\partial V_{\text{grav}}}{\partial \theta_{R,s}} &= g \sum_{i=1}^{n} m_{R,i} \frac{y_{m_{R,i}}}{\partial \theta_{R,s}}
\end{aligned}$$

expanding the mass position partials,

$$\frac{\partial y_{m_{L,i}}}{\partial \theta_h} = -d_L \cos(\theta_h + \phi_L)$$

$$\frac{\partial y_{m_{L,i}}}{\partial \theta_{L,s}} = \begin{cases} 0 & s > i \\ l_{c_{L,s}} \cos(\theta_{L,s}) & s = i \\ l_{L,s} \cos(\theta_{L,s}) & s < i \end{cases}$$

$$\frac{\partial y_{m_{R,i}}}{\partial \theta_h} = d_R \cos(\theta_h - \phi_R)$$

$$\frac{\partial y_{m_{R,i}}}{\partial \theta_{R,s}} = \begin{cases} 0 & s > i \\ l_{c_{R,s}} \cos(\theta_{R,s}) & s = i \\ l_{R,s} \cos(\theta_{R,s}) & s < i \end{cases}$$

Substituting these partials, the generalized force equations are shown below

$$Q_{x_{\text{grav}}} = 0$$

$$Q_{y_{\text{grav}}} = -g\big(m_h + \sum_{i=1}^{n}[m_{L,i} + m_{R,i}]\big)$$

$$Q_{h_{\text{grav}}} = -g\big(- d_L \cos(\theta_h + \phi_L) \sum_{i=s+1}^{n} [m_{L,i}] + d_R \cos(\theta_h - \phi_R) \sum_{i=s+1}^{n} [m_{R,i}]\big)$$

$$Q_{L,s_{\text{grav}}} = -g\big(l_{c_{L,s}} m_{L,s} + l_{L,s} \sum_{i=s+1}^{n} [m_{L,i}]\big) \cos(\theta_{L,s})$$

$$Q_{R,s_{\text{grav}}} = -g\big(l_{c_{R,s}} m_{R,s} + l_{R,s} \sum_{i=s+1}^{n} [m_{R,i}]\big) \cos(\theta_{R,s})$$

3.1.3 Contact Forces

Adding contact forces is done in a similar way to the limb only model. At every time step, the contact force function monitors the y-position of the links, calculating contact forces once they are within a certain bound of zero. Once in contact, the contact force is calculated to be the required force to keep the y-velocity of the joint at zero given the natural dynamics and other external

forces. To prevent joints from becoming "stuck" to the surface, if the required force is negative, that joint is removed and solver iterates to find the forces for the other joints in contact. The first step in finding which joints are in contact. This can be achieved by comparing the the calculated y position to a ground threshold value. The y position and velocity for the end of the i^{th} joint are defined below

$$y_{L,i} = y - d_L \sin(\theta_h + \phi_L) + \sum_{j=1}^{i} l_{L,j} \sin(\theta_{L,j})$$

$$y_{R,i} = y + d_R \sin(\theta_h - \phi_R) + \sum_{j=1}^{i} l_{R,j} \sin(\theta_{R,j})$$

$$\dot{y}_{L,i} = \dot{y} - d_L \dot{\theta}_h \cos(\theta_h + \phi_L) + \sum_{j=1}^{i} l_{L,j} \dot{\theta}_{L,j} \cos(\theta_{L,j})$$

$$\dot{y}_{R,i} = \dot{y} + d_R \dot{\theta}_h \cos(\theta_h - \phi_R) + \sum_{j=1}^{i} l_{R,j} \dot{\theta}_{R,j} \cos(\theta_{R,j})$$

Since the equation for the effect of the forces on the state is nonlinear in the state, with an additional objective function which is also nonlinear in the state, an iterative Newton-Raphson solver is used to find the required forces, like with the limb model, using the formulation in equation 2.17. For the full model case, the objective function is the y velocity of joints in contact, $\dot{y}_{X,i}$, and the search variable is the normal force at that joint, $N_{X,i}$. For those previous two variables, X is a placeholder for left, L, or right, R. So if an arbitrary u joints indices $\mathbf{i}_c = [i_{c,1} i_{c,2}, ..., i_{c,u}]$ in contact, the objective function would be $\mathbf{f} = [\dot{y}_{i_{c,1}}\ \dot{y}_{i_{c,2}},\ ...,\ \dot{y}_{i_{c,u}}]^T$, and the search variable is $\mathbf{x} = [N_{i_{c,1}},\ N_{i_{c,2}},\ ...,\ N_{i_{c,u}}]^T$. For the full model, these contact indices are the index within the generalized position vector for the link in question, rather than the link-based indices used throughout the rest of this work. The hub uses all three indices from its states to monitor the joints connected to each limb as well as the hub mass, in the case where the AoES becomes inverted. With the necessary terms defined, the last piece required to perform the calculations, the Jacobian, can be found. Starting from the the y velocity of a random joint s, the effect of a normal force on joint i can be determined from a potential function, like for the gravitational forces, though this one is discontinuous. The potential

function for normal forces is defined below

$$V_{\mathrm{N}} = a(N_h, y)N_h y - \sum_{i=0}^{n}[a(N_{L,i}, y_{L,i})N_{L,i}y_{L,i} + a(N_{R,i}, y_{R,i})N_{R,i}y_{R,i}] \tag{3.15}$$

where the coefficient, $a(N, y)$ replaces the piece wise function in the limb model potential function with its own definition

$$a(N, y) = \begin{cases} 1, & y \leq 0 \ \& \ N > 0 \\ 0, & \text{else} \end{cases}$$

For the equation above, the $i = 0$ case refers to the joint at the root of the first link on that side, or, equivalently, the corresponding side of the hub link. In the following equations, i_s, which comes from $\mathbf{i}_c$, is a single index that loops through all generalized coordinates, rather than the left-right-hub notation used elsewhere. Taking the partial with respect to the generalized coordinates,

$$\frac{\partial V_{\mathrm{N}}}{\partial q_s} = \sum_{i_s=\mathbf{i}_c} N_{i_s} \frac{y_{i_s}}{\partial q_s}$$

$$\frac{\partial y_{i_s}}{\partial x} = 0$$

$$\frac{\partial y_{i_s}}{\partial y} = 1$$

$$\frac{\partial y_{i_s}}{\partial \theta_h} = \begin{cases} 0 & \text{Hub mass contact} \\ -d_L \cos(\theta_h + \phi_L) & \text{Left contact} \\ d_R \cos(\theta_h - \phi_R) & \text{Right contact} \end{cases}$$

$$\frac{\partial y_{i_s}}{\partial \theta_{L,s}} = \begin{cases} 0 & s > i \\ l_{L,s} \cos(\theta_{L,s}) & s \leq i \end{cases}$$

$$\frac{\partial y_{i_s}}{\partial \theta_{R,s}} = \begin{cases} 0 & s > i \\ l_{R,s} \cos(\theta_{R,s}) & s \leq i \end{cases}$$

$$\frac{\partial V_{\mathrm{N}}}{\partial q_s} = -l_s \cos(q_s) \sum_{i=\mathbf{i}_c \geq s} N_i$$

$$Q_{N_s} = l_s \cos(q_s) \sum_{i=\mathbf{i}_c \geq s} N_i$$

$$
\begin{aligned}
Q_{x_{\mathrm{N}}} &= 0 \\
Q_{y_{\mathrm{N}}} &= \sum_{i=\mathbf{i}_c} N_i \\
Q_{h_{\mathrm{N}}} &= (d_L \cos(\theta_h + \phi_L) - d_R \cos(\theta_h - \phi_R)) \sum_{i=\mathbf{i}_c \geq s} N_i \\
Q_{L,s_{\mathrm{N}}} &= l_{L,s} \cos(\theta_{L,s}) \sum_{i=\mathbf{i}_c \geq s} N_i \\
Q_{R,s_{\mathrm{N}}} &= l_{R,s} \cos(\theta_{R,s}) \sum_{i=\mathbf{i}_c \geq s} N_i
\end{aligned}
$$

For an arbitrary time step k, our objective is to find the force setting the y component of velocity to zero at the next time step, $\dot{y}_{i_{c,a},k} = 0$. Taking the partial with respect to $N_{i_{c,b}}$, obtaining

$$
\frac{\partial \dot{y}_{i_{c,a},k}}{\partial N_{i_{c,b}}} = \sum_{j=1}^{i_{c,a}} \left[l_{X,j} \left(\frac{\partial \dot{\theta}_{X,j,k+1}}{\partial N_{i_{c,b}}} \cos(\theta_{X,j,k+1}) - \dot{\theta}_{X,j,k+1} \sin(\theta_{X,j,k+1}) \frac{\partial \theta_{X,j,k+1}}{\partial N_{i_{c,b}}} \right) \right]
$$

Where X corresponds to either the left or right side, depending on where the contact has occurred. To find the partial of the states at time $k+1$, the dynamics definition from equation 2.16 is used in finding the effect of the normal force on the state at the next time step using an Euler approximation, $\mathbf{r}_{k+1} = \mathbf{r}_k + B_k^{-1}(\mathbf{p} - A_k \mathbf{r}_k)\mathrm{d}t$. Using this definition, and starting with the partial with respect to the full state, since any particular state is just a linear transformations of the full

state

$$\frac{\partial r_{k+1}}{\partial N_{i_{c,b}}} = B_k^{-1}\frac{\partial \mathbf{p}}{\partial N_{i_{c,b}}}\mathrm{d}t$$

$$\frac{\partial \mathbf{p}}{\partial N_{i_{c,b}}} = \Big[\frac{\partial Q_{L,n_\mathrm{N}}}{\partial N_{i_{c,b}}},\ ...,\ \frac{\partial Q_{L,1_\mathrm{N}}}{\partial N_{i_{c,b}}}, \frac{\partial Q_{x_\mathrm{N}}}{\partial N_{i_{c,b}}},\ \frac{\partial Q_{y_\mathrm{N}}}{\partial N_{i_{c,b}}},\ \frac{\partial Q_{h_\mathrm{N}}}{\partial N_{i_{c,b}}},\ \frac{\partial Q_{R,1_\mathrm{N}}}{\partial N_{i_{c,b}}},\ ...,\ \frac{\partial Q_{R,n_\mathrm{N}}}{\partial N_{i_{c,b}}}\Big]^T$$

$$\frac{\partial Q_{x_\mathrm{N}}}{\partial N_{i_{c,b}}} = 0$$

$$\frac{\partial Q_{y_\mathrm{N}}}{\partial N_{i_{c,b}}} = 1$$

$$\frac{\partial Q_{h_\mathrm{N}}}{\partial N_{i_{c,b}}} = \begin{cases} d_L\cos(\theta_h + \phi_L), & \text{if } i_{c,b} \text{ refers to a left hand joint} \\ d_R\cos(\theta_h - \phi_R), & \text{if } i_{c,b} \text{ refers to a right hand joint} \end{cases}$$

$$\frac{\partial Q_{L,s_\mathrm{N}}}{\partial N_{i_{c,b}}} = \begin{cases} l_{L,s}\cos(\theta_{L,s}), & \text{if } i_{c,b} \text{ refers to a left hand joint} \\ 0, & \text{if } i_{c,b} \text{ refers to a right hand joint or is closer to the hub than } s \end{cases}$$

$$\frac{\partial Q_{R,s_\mathrm{N}}}{\partial N_{i_{c,b}}} = \begin{cases} 0, & \text{if } i_{c,b} \text{ refers to a left hand joint or is closer to the hub than } s \\ l_{R,s}\cos(\theta_{R,s}), & \text{if } i_{c,b} \text{ refers to a right hand joint} \end{cases}$$

Since the A and B matrices are dependent of the state at the previous time step, they are independent of the normal force, making these partials relatively simple. Assembling these terms allows each term of the Jacobian to be written with the matrix equation

$$J(a,b) = \Psi(a)B_k^{-1}\frac{\partial \mathbf{p}}{\partial N_{i_{c,b}}}\mathrm{d}t \tag{3.16}$$

Where Ψ is a matrix whose value depends on the velocity of the joint at $i_{c,a}$, an arbitrary joint in contact, as outlined below.

$$\Psi(a) = \Big[\psi_{L,n}(a),\ ...,\ \psi_{L,1}(a), \psi_x(a),\ \psi_y(a),\ \psi_h(a),\ \psi_{R,1}(a),\ ...,\ \psi_{R,n}(a),\ \psi_{\dot{L},n}(a),\ ...,$$
$$\psi_{\dot{L},1}(a), \psi_{\dot{x}}(a),\ \psi_{\dot{y}}(a),\ \psi_{\dot{h}}(a),\ \psi_{\dot{R},1}(a),\ ...,\ \psi_{\dot{R},n}(a)\Big]^T$$

$$\psi_x(a) = 0$$

$$\psi_y(a) = 0$$

$$\psi_h(a) = \begin{cases} -d_L \sin(\theta_h + \phi_L)\dot{\theta}_h, & \text{if } i_{c,a} \text{ refers to a left hand joint} \\ -d_R \sin(\theta_h - \phi_R)\dot{\theta}_h, & \text{if } i_{c,a} \text{ refers to a right hand joint} \end{cases}$$

$$\psi_{L,s}(a) = \begin{cases} -l_{L,s} \sin(\theta_{L,s})\dot{\theta}_{L,s}, & \text{if } i_{c,a} \text{ refers to a left hand joint} \\ 0, & \text{if } i_{c,a} \text{ refers to a right hand joint or is closer to the hub than } s \end{cases}$$

$$\psi_{R,s}(a) = \begin{cases} 0, & \text{if } i_{c,a} \text{ refers to a left hand joint or is closer to the hub than } s \\ -l_{R,s} \sin(\theta_{R,s})\dot{\theta}_{R,s}, & \text{if } i_{c,a} \text{ refers to a right hand joint} \end{cases}$$

$$\psi_{\dot{x}}(a) = 0$$

$$\psi_{\dot{y}}(a) = 1$$

$$\psi_{\dot{h}}(a) = \begin{cases} d_L \cos(\theta_h + \phi_L), & \text{if } i_{c,a} \text{ refers to a left hand joint} \\ d_R \cos(\theta_h - \phi_R), & \text{if } i_{c,a} \text{ refers to a right hand joint} \end{cases}$$

$$\psi_{\dot{L},s}(a) = \begin{cases} l_{L,s} \cos(\theta_{L,s}), & \text{if } i_{c,a} \text{ refers to a left hand joint} \\ 0, & \text{if } i_{c,a} \text{ refers to a right hand joint or is closer to the hub than } s \end{cases}$$

$$\psi_{\dot{R},s}(a) = \begin{cases} 0, & \text{if } i_{c,a} \text{ refers to a left hand joint or is closer to the hub than } s \\ l_{R,s} \cos(\theta_{R,s}), & \text{if } i_{c,a} \text{ refers to a right hand joint} \end{cases}$$

3.1.4 Frictional Forces

Frictional forces are incorporated using the Coulomb friction model, where friction is proportional to the normal force by some constant coefficient of friction, μ. This creates a new potential

function

$$V_{\mathrm{f}} = -a(N_{L,i}, y_{L,i})(N_{L,i}y_{L,i} - |\int_{x_{L,i}} f_{L,i}dx|) - \sum_{i=1}^{n}[a(N_{L,i}, y_{L,i})(N_{L,i}y_{L,i} - |\int_{x_{L,i}} f_{L,i}dx|) + a(N_{R,i}, y_{R,i})(N_{R,i}y_{R,i} - |\int_{x_{R,i}} f_{R,i}dx|)] \quad (3.17)$$

Since this force acts in the x direction, the x position and velocity of each joint are defined below

$$x_i = \sum_{j=1}^{i} l_j \cos(q_j)$$

$$\dot{x}_i = -\sum_{j=1}^{i} l_j \dot{q}_j \sin(q_j)$$

In equation 2.20, the integral is defined as the force integrated over the total distance traveled, which can also be parameterized in time, making the upcoming partials more clear. Additionally, the relationship to the normal force is made more clear, such that there is only one force variable.

$$V_{\mathrm{f}} = -\sum_{i=1}^{n} \begin{cases} N_i y_i - |\int_{t_o}^{t_f} \mu N_i(t)\dot{x}_i \mathrm{d}t|, & y_i \leq 0, \ \& \ N_i > 0 \\ 0, & \text{else} \end{cases}$$

To find the generalized force, the partial is taken with respect to the state, as with the above two forces. This results in the generalized force as a function of the normal force shown below

$$Q_{f_s} = l_s \sum_{i=\mathbf{i}_c \geq s} \left[\big(\cos(q_s) - sign(\dot{x})\mu \sin(q_s)\big)N_i\right] \quad (3.18)$$

$$Q_{x_{\mathrm{f}}} = -\mu \sum_{i=\mathbf{i}_c} sign(\dot{x}_i)N_i$$

$$Q_{y_{\mathrm{f}}} = \sum_{i=\mathbf{i}_c} N_i$$

$$Q_{h_{\mathrm{f}}} = \sum_{i=\mathbf{i}_c \geq s} (d_L(\cos(\theta_h + \phi_L) - \mu \mathrm{sign}(\dot{x}_i)\sin(\theta_h + \phi_L)) - d_R(\cos(\theta_h - \phi_R) - \mu \mathrm{sign}(\dot{x}_i)\sin(\theta_h - \phi_R)))N_i$$

$$Q_{L,s_{\mathrm{f}}} = l_{L,s} \sum_{i=\mathbf{i}_c \geq s} (\cos(\theta_{L,s}) - \mu \mathrm{sign}(\dot{x}_i)\sin(\theta_{L,s}))N_i$$

$$Q_{R,s_{\mathrm{f}}} = l_{R,s} \sum_{i=\mathbf{i}_c \geq s} (\cos(\theta_{R,s}) - \mu \mathrm{sign}(\dot{x}_i)\sin(\theta_{R,s}))N_i$$

Now that the equation for the generalized friction force has been found, and repeating a similar process for the combined normal and friction forces as normal alone in the previous section to find the Jacobian. Conveniently, the only change is to the partial of the force vector $\mathbf{p}$ with respect to the normal, which now becomes

$$\frac{\partial \mathbf{p}_{\mathrm{f}}}{\partial N_{i_{c,b}}} = \Big[\frac{\partial Q_{L,n_{\mathrm{f}}}}{\partial N_{i_{c,b}}}, \ ..., \ \frac{\partial Q_{L,1_{\mathrm{f}}}}{\partial N_{i_{c,b}}}, \frac{\partial Q_{x_{\mathrm{f}}}}{\partial N_{i_{c,b}}}, \ \frac{\partial Q_{y_{\mathrm{f}}}}{\partial N_{i_{c,b}}}, \ \frac{\partial Q_{h_{\mathrm{f}}}}{\partial N_{i_{c,b}}}, \ \frac{\partial Q_{R,1_{\mathrm{f}}}}{\partial N_{i_{c,b}}}, \ ..., \ \frac{\partial Q_{R,n_{\mathrm{f}}}}{\partial N_{i_{c,b}}}\Big]^T$$

$$\frac{\partial Q_{x_{\mathrm{f}}}}{\partial N_{i_{c,b}}} = -\mu$$

$$\frac{\partial Q_{y_{\mathrm{f}}}}{\partial N_{i_{c,b}}} = 1$$

$$\frac{\partial Q_{h_{\mathrm{f}}}}{\partial N_{i_{c,b}}} = \begin{cases} d_L(\cos(\theta_h + \phi_L) - \mu \mathrm{sign}(\dot{x}_{i_{c,b}}) \sin(\theta_h + \phi_L)) & \text{if } i_{c,b} \text{ refers to a left hand joint} \\ d_R(\cos(\theta_h - \phi_R) - \mu \mathrm{sign}(\dot{x}_{i_{c,b}}) \sin(\theta_h - \phi_R)) & \text{if } i_{c,b} \text{ refers to a right hand joint} \end{cases}$$

$$\frac{\partial Q_{L,s_{\mathrm{f}}}}{\partial N_{i_{c,b}}} = \begin{cases} l_{L,s}(\cos(\theta_{L,s}) + \mu \mathrm{sign}(\dot{x}_{i_{c,b}}) \sin(\theta_{L,s})), & \text{if } i_{c,b} \text{ refers to a left hand joint} \\ 0, & \text{if } i_{c,b} \text{ refers to a right hand joint or is closer to the hub than } s \end{cases}$$

$$\frac{\partial Q_{R,s_{\mathrm{f}}}}{\partial N_{i_{c,b}}} = \begin{cases} 0, & \text{if } i_{c,b} \text{ refers to a left hand joint or is closer to the hub than } s \\ l_{R,s}(\cos(\theta_{R,s}) - \mu \mathrm{sign}(\dot{x}_{i_{c,b}}) \sin(\theta_{R,s})), & \text{if } i_{c,b} \text{ refers to a right hand joint} \end{cases}$$

3.1.5 Control

As with the limb model, the last force added to the full AoES model is actuator torques. The total potential function from all possible actuators in a model is shown in the eqn below.

$$V_{\mathrm{ctrl}} = -M_{L,1}(\theta_{L,1} + \theta_h) - M_{R,1}(\theta_{R,1} - \theta_h) - \sum_{i=1}^{n}[M_{L,i}(\theta_{L,i} - \theta_{L,i-1}) + M_{R,i}(\theta_{R,i} - \theta_{R,i-1})] \quad (3.19)$$

In the same way that the positive angle definition is mirrored between the left and right limbs, the actuator torque definition is also mirrored. This creates a system where a positive torque at a joint

causes a positive acceleration in that joint angle, all else constant.

$$\frac{\partial V_{\text{ctrl}}}{\partial \theta_h} = -M_{L,1} + MR, 1$$
$$\frac{\partial V_{\text{ctrl}}}{\partial \theta_{L,s}} = -M_{L,i} + ML, i+1$$
$$\frac{\partial V_{\text{ctrl}}}{\partial \theta_{R,s}} = -M_{R,i} + MR, i+1$$
$$Q_{ctrl_h} = M_{L,1} - MR, 1$$
$$Q_{ctrl_{L,s}} = M_{L,i} - ML, i+1$$
$$Q_{ctrl_{R,s}} = M_{R,i} - MR, i+1$$

3.2 Results

The results procedure is extremely similar to the limb model, in that the energy of the links is calculated for each time step of the simulation, along with the energy dissipated by the dampers, to be sure conservation of energy is observed. With contact forces, since a perfectly inelastic collision is assumed, the total energy should have a step decrease upon each impact. Plots of the states and energies for a few test cases are shown below. Most plots are shown with 2 links per arm for simplicity. To decrease the number of variables, all limbs shown in results use the "petal" shape shown in the images of the AoES, have a total length of $1.8m$, thickness of $2.54x10^{-3}m$, an elastic modulus of $4.36Mpa$, and limb density of $1000\frac{kg}{m^3}$. Unless otherwise noted, the time step for these simulations is $0.01s$, with the simulation time varying depending on the phenomenon being observed. Unfortunately, unlike with the limb model, there is an unresolved dynamics bug in the code, which only produces reasonable results for cases where the parameters and states of the left and right limbs are the same, and some terms are manually set to zero. These preliminary results are shown below.

3.2.1 Unforced Dynamics

3.2.2 Unforced

To show that the model performs with only internal forces, the unforced dynamics case is shown here. Depending on the initial condition, the energy rate appears to be only numerical errors, but other initial conditions seem like the response is not reasonable. The symmetry of the Flapper case seems to eliminate errors, while the inverse symmetry of the Waver seems to cause it to break down.

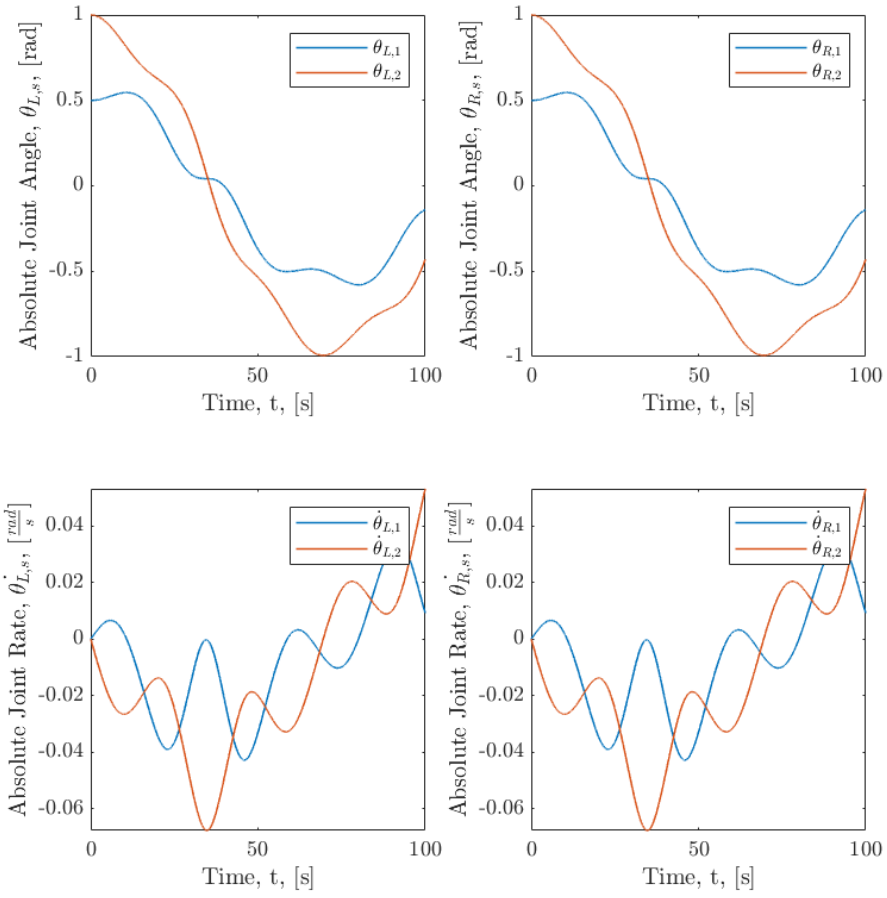

Figure 3.2: This plot of the system states, with angles on the upper subplot and angular rates on the lower, shows the system behavior over a 100 second simulation. the limb oscillates due to the restoring force from the springs

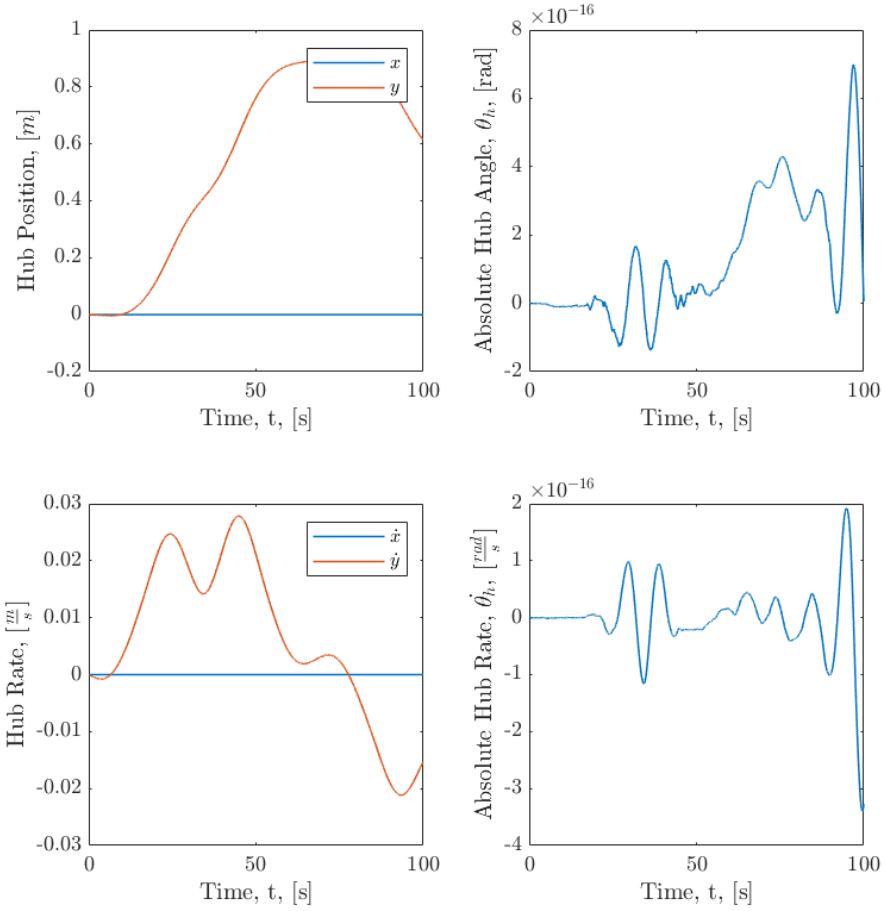

Figure 3.3: This plot of the system states, with angles on the upper subplot and angular rates on the lower, shows the system behavior over a 100 second simulation. The mass y position changes in opposition to the movement of the limbs

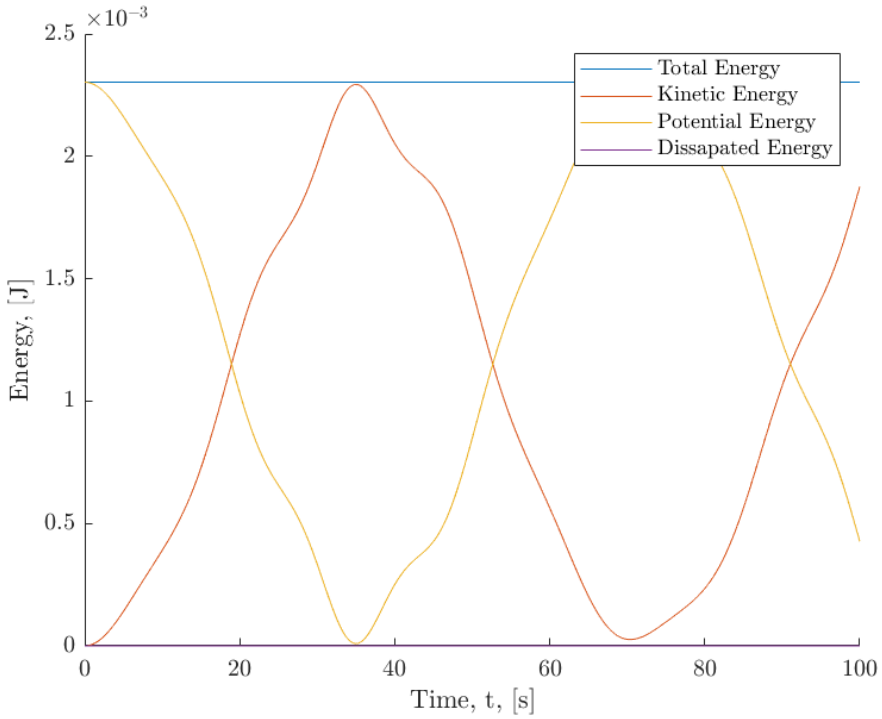

[H]

Figure 3.4: This plot of the system energies, shows the system behavior over a 100 second simulation. Over this period, energy passes between kinetic an potential, as expected, since these is no form of dissipation.

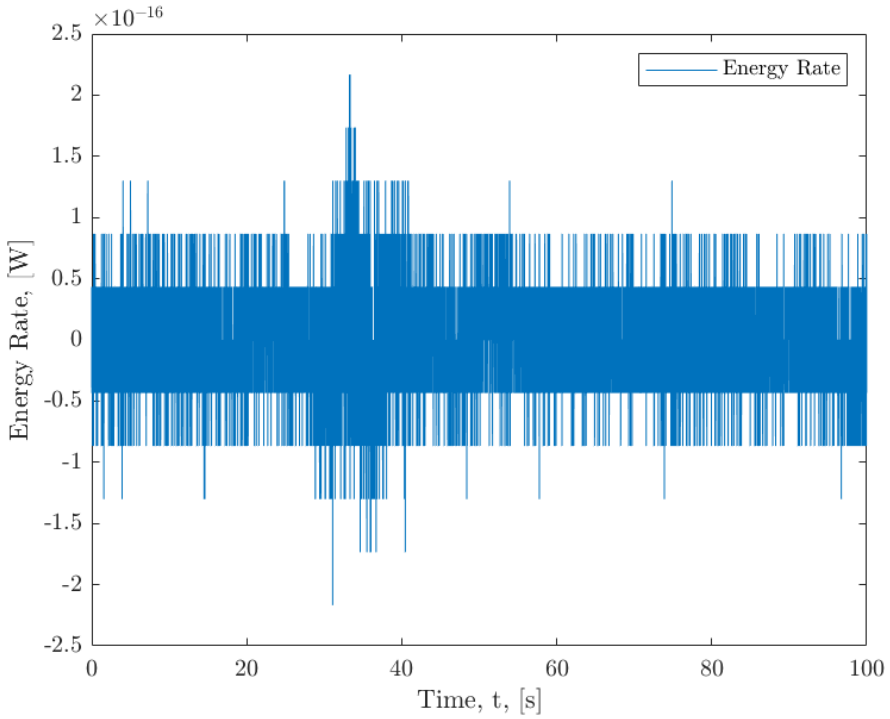

Figure 3.5: This plot of the system energy rate, shows the system behavior over a 100 second simulation. Over this period, energy rates appear to be numerical errors.

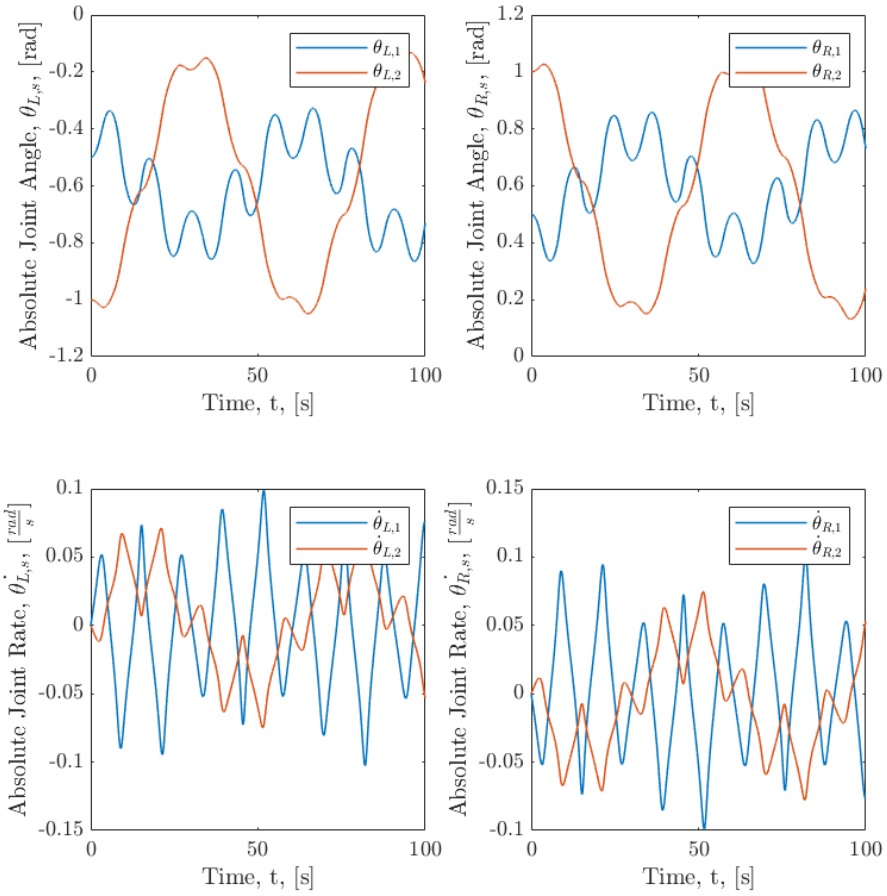

Figure 3.6: This plot of the system states, with angles on the upper subplot and angular rates on the lower, shows the system behavior over a 100 second simulation. The limb oscillates due to the restoring force from the springs.

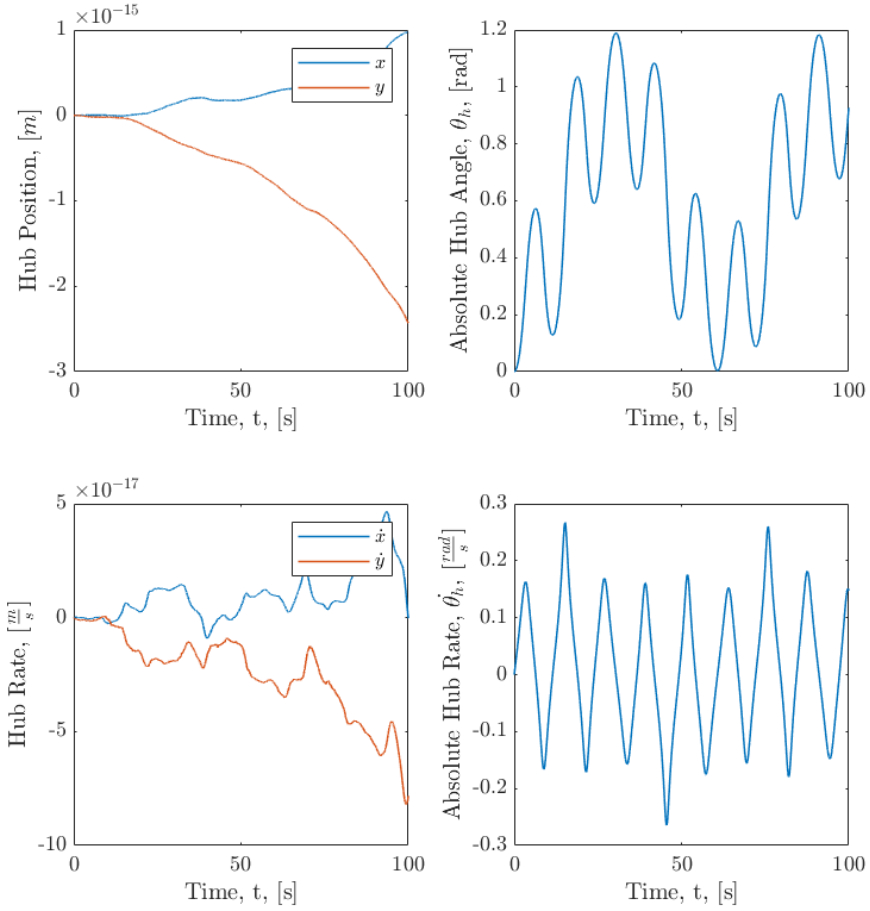

Figure 3.7: This plot of the system states, with angles on the upper subplot and angular rates on the lower, shows the system behavior over a 100 second simulation. The limb oscillates due to the restoring force from the springs. However, the model seems to accelerate the x and y positions continuously, which would be unexpected.

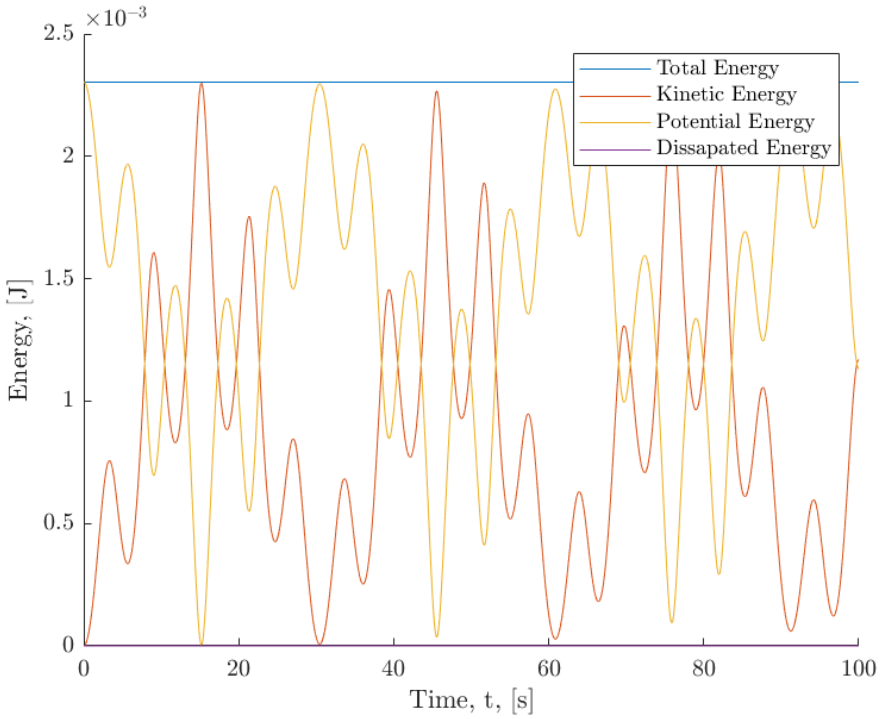

Figure 3.8: This plot of the system energies, shows the system behavior over a 100 second simulation. Over this period, energy passes between kinetic an potential, as expected, since these is no form of dissipation.

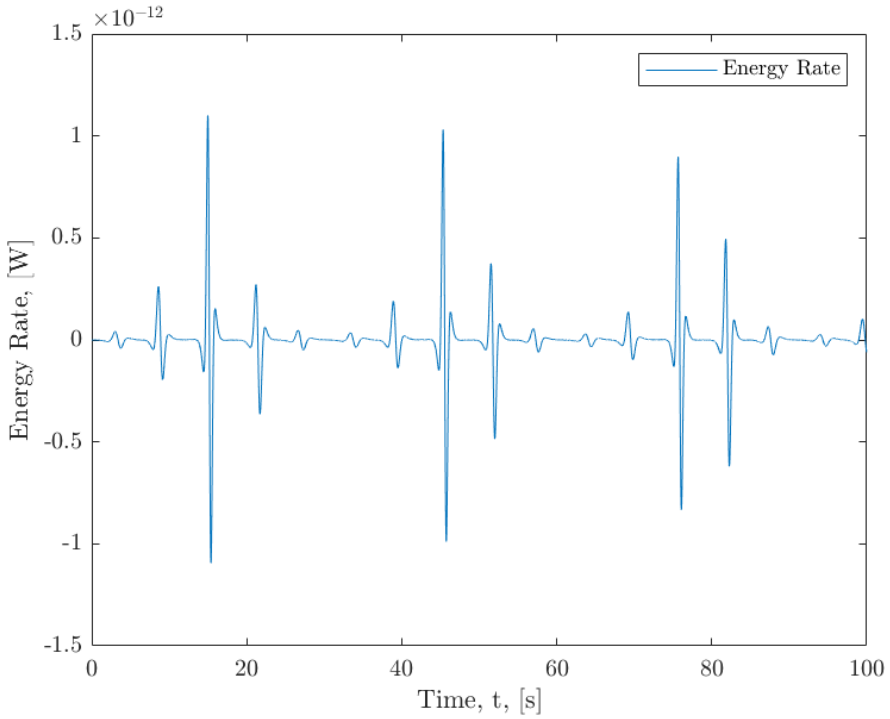

Figure 3.9: This plot of the system energy rate, shows the system behavior over a 100 second simulation. Over this period, energy rates may or may nor be numerical errors.

3.2.3 Gravity

For the gravity verification, the AoES started with a symmetric initial position, as not to exacerbate dynamics errors.

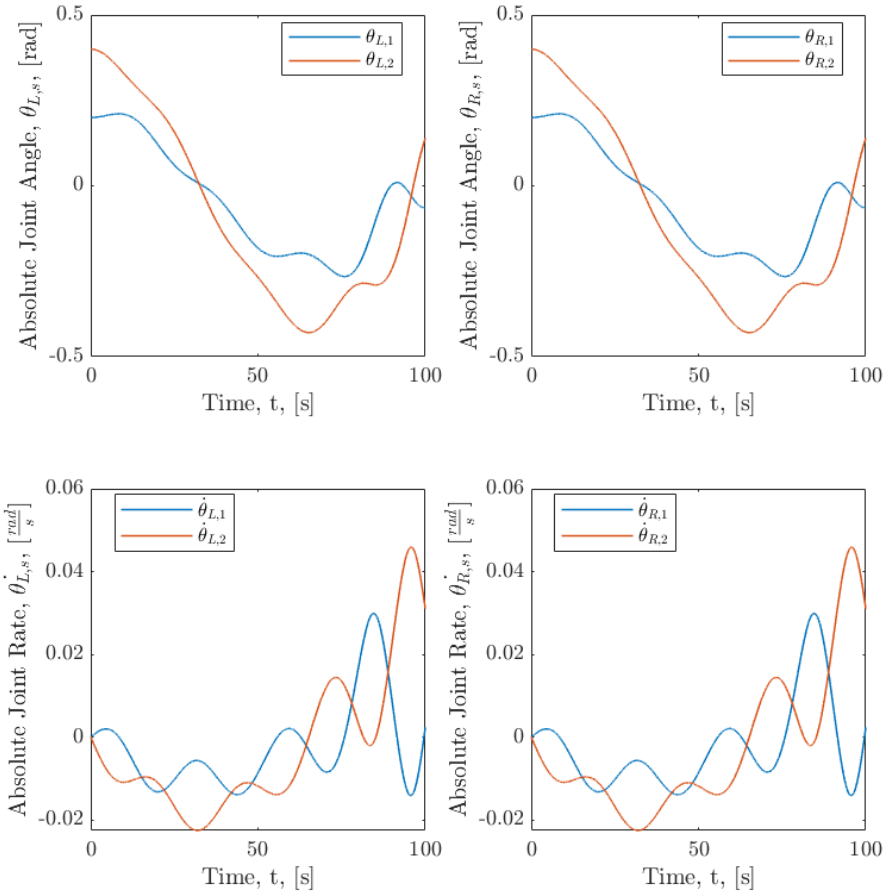

Figure 3.10: This plot of the system states, with angles on the upper subplot and angular rates on the lower, shows the system behavior over a 100 second simulation. The limb oscillates due to the restoring force from the springs in a similar manner to the flapper unforced case.

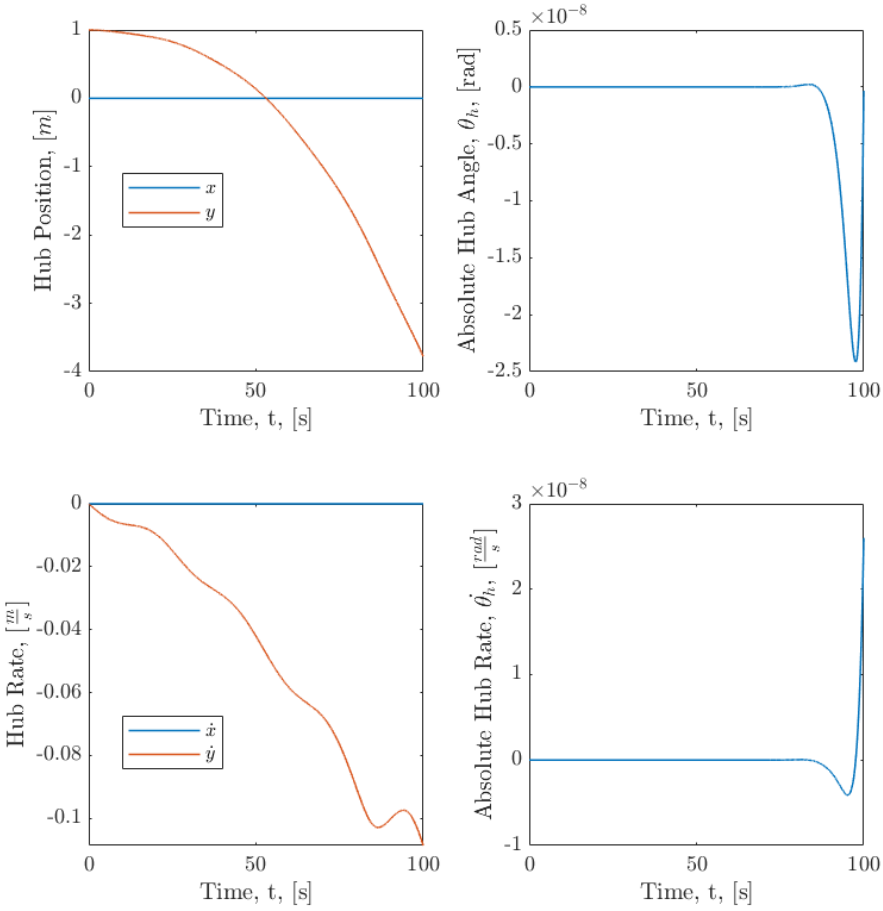

Figure 3.11: This plot of the system states, with angles on the upper subplot and angular rates on the lower, This the system behavior over a 100 second simulation. The y position is the only state that appreciably changes, as expected.

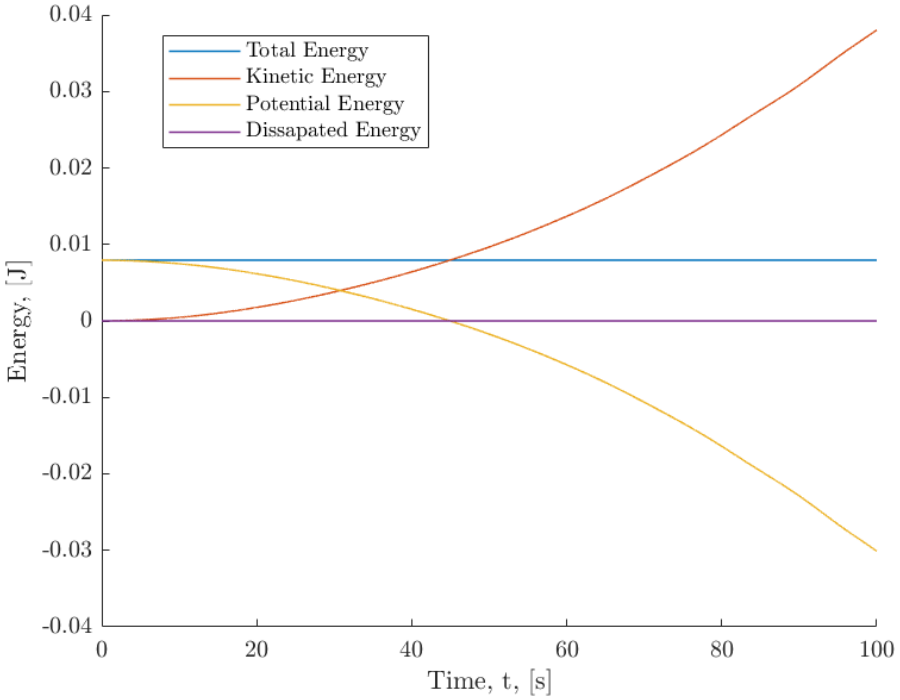

Figure 3.12: This plot of the system energies, shows the system behavior over a 100 second simulation. Over this period, energy passes between kinetic an potential, as expected, since these is no form of dissipation.

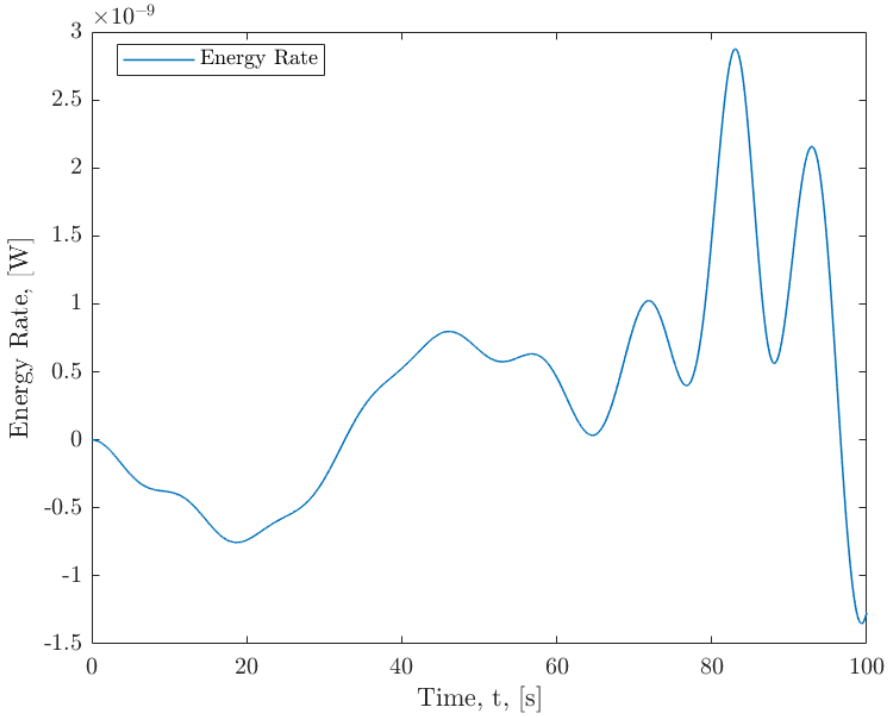

Figure 3.13: This plot of the system energy rate, shows the system behavior over a 100 second simulation. Over this period, energy rates appear similar to the smooth errors seen in the limb only model

3.2.4 Contact

Contact Forces appear to be working in terms of results, as the energy displays the expected step-wise behavior, though while running the simulation frequently reaches the maximum number of iterations when calculating the normal force.

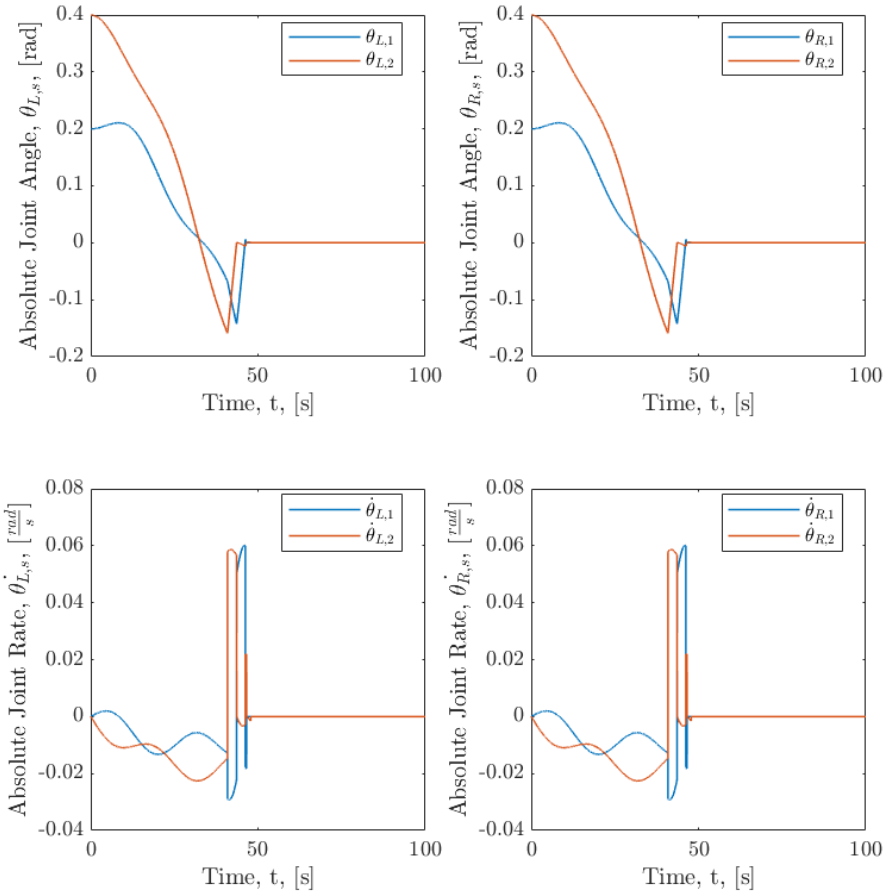

Figure 3.14: This plot of the system states, with angles on the upper subplot and angular rates on the lower, shows the system behavior over a 100 second simulation. The limb response has no real features of note.

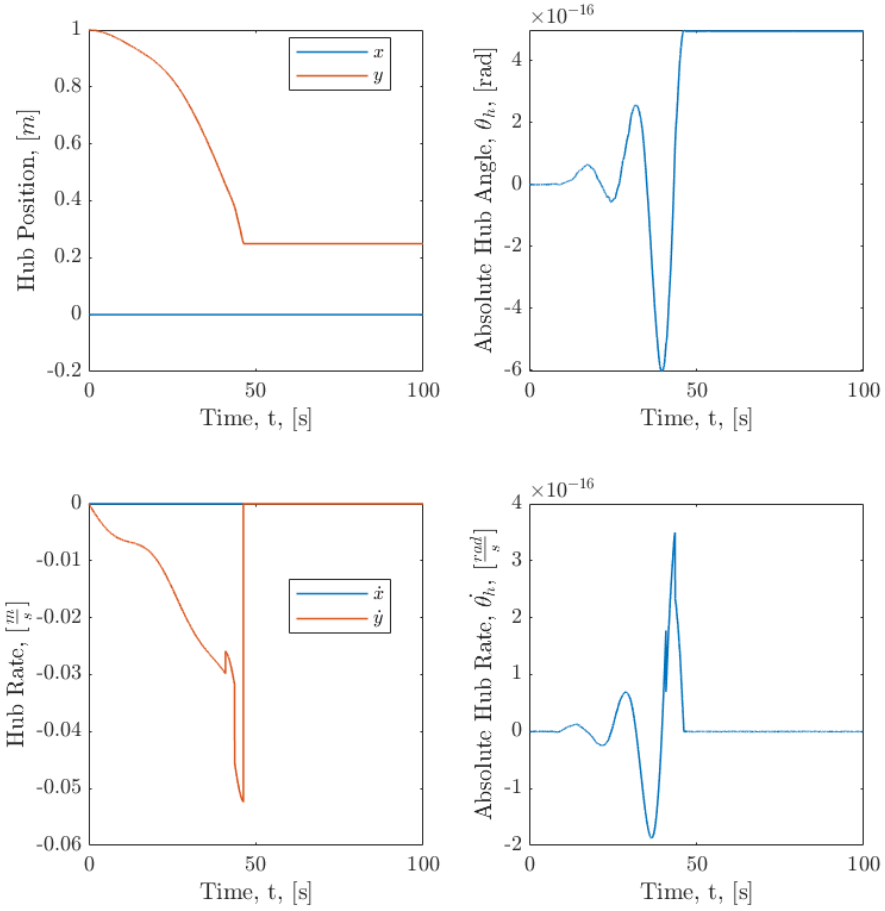

Figure 3.15: This plot of the system states, with angles on the upper subplot and angular rates on the lower, shows the system behavior over a 100 second simulation. The only hub state that meaningfully changes is the hub y position, which accelerates downward until the link beneath it hits the ground.

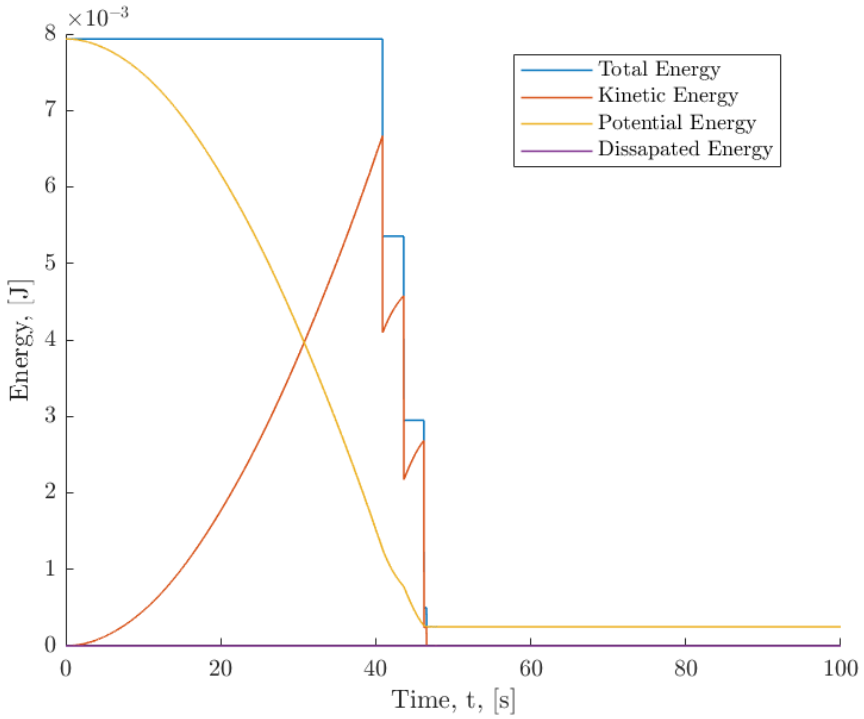

Figure 3.16: This plot of the system energies, shows the system behavior over a 100 second simulation. Each time a link strikes the ground, the system looses energy at that time step

Chapter 4

Electroadhesion

4.1 Overview

A key part of mining small bodies is being able to remain on the asteroid surface. Due to the micro-gravity environment, small disturbances could lead to the AoES escaping the asteroid system, or at least wasting days in orbit. While passive adhesive forces should be enough for static operations like digging and launching, as established in work by McMahon [20] mobile operations may require extra adhesive forces, especially those which cause a reduction in the area in contact with the body. Since the AoES will already need a high voltage system onboard for the HASEL actuators, electroadhesion is a natural choice for increasing our adhesion to the body. While electroadhesion is best suited to flat, monolithic surfaces, as long as it creates forces on the order of the natural adhesion of the body, the potential maximum adhesion would be achieved, since higher attractive forces would only result in peeling off the top layer of material. To this end, experimental work was carried out to begin to characterize the adhesive forces of electroadhesion on granular surfaces. The first part of this work was designing a test fixture capable of determining adhesion forces in shear, normal, and peel. The fixture was then used to characterize electroadhesive pads on relatively flat, monolithic materials; rough, monolithic materials, and granular materials. The flat, monolithic tested for this thesis were PMMA, glass, wood, slate, Metalized PET, and cardboard. The rough, monolithic material tested was cork bark, tested in both with the primary roughness direction aligned with the direction of force, and perpendicular to it. The granular materials tested were regolith simulant made by the CLASS Exolith lab at UCF, sand, gravel, and leaf litter.

Due to time constraints, only shear forces were gathered for this thesis. The results of the tests separate the materials into three clear force groups which align with the categories shown above. The flat, monolithic materials tested had average force values of 3 to 16 newtons, while the cork had an average of about 0.6, and the granular materials varied between 0.1 N and forces which were too small to measure. Some of this is due to the inherently stochastic nature of these tests, especially for the granular materials. More work needs to be done to better understand the effects of electroadhesion on these materials.

4.2 Test Procedure

To test the adhesive forces, a test fixture was designed to be able to test shear, normal, and peel forces in order to fully characterize the force profile of the pads. This was achieved with a pulley and rail system, which allows a string attached to a collar on the pad to be pulled in a consistent direction. Applying the force is an Aurora 310C muscle tester, which is capable of measuring torque and displacement while providing either force or length control through a motor and lever arm. The test bed is removable to allow for the easy swapping of materials, and has enough depth to fit test beds of granular materials. Additionally, the test fixture has guards on the front and rear of the test bed to ensure the operator is protected from high voltage when the pad slips. A picture of the finished test fixture can be seen in figure 4.1.

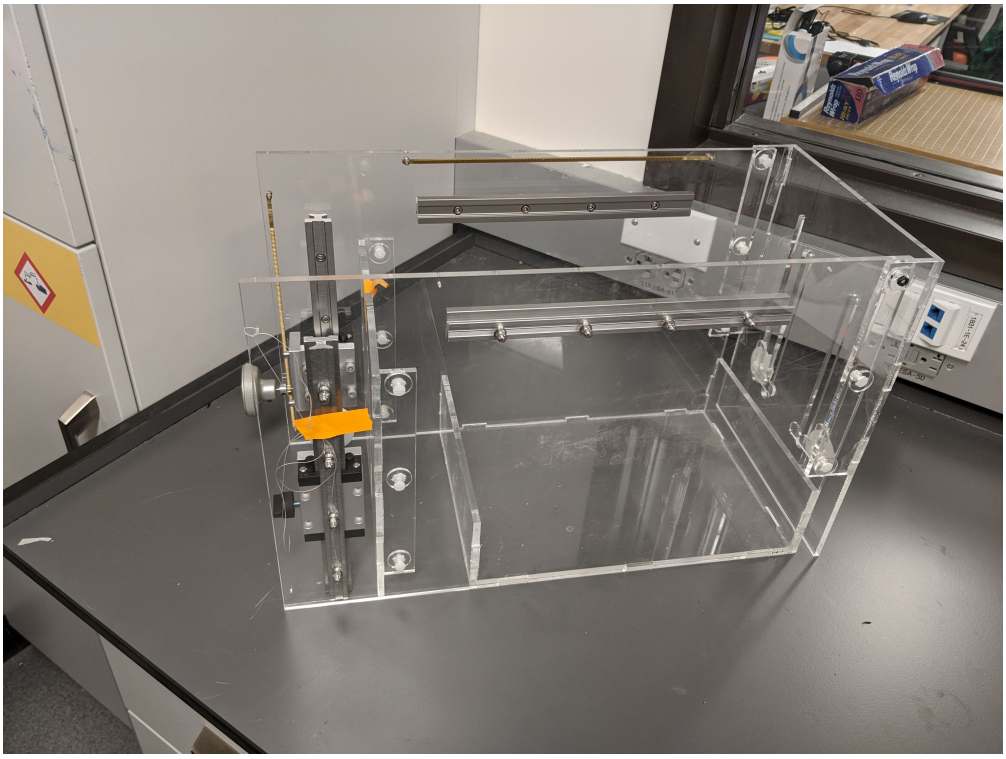

Figure 4.1: Picture of the completed Test Fixture

Test materials were mounted such that they could not slip under shear, but were easily removable, by having a close fit with the side walls of the test bed, and bars underneath to prevent movement along the test direction. Most materials were mounted to acrylic sheets, with the exception of wood and the granular materials. Mounting was achieved with spray glue, double-sided tape, or Gorilla Glue, depending on the material. The cork bark was made from a piece of reptile terrarium wall decoration, cut to size an mounted to an acrylic sheet with Gorilla Glue. The test piece includes two test sides, one where the electroadhesive pad is pulled across the predominant bark fissure direction,and the other where it is pulled parallel to them. The acrylic test piece was simply an acrylic sheet cut to size with two bars to prevent forward movement in the test fixture. The wood test piece was a board cut to size, with two pieces of wood attached in a similar arrangement to the acrylic using Gorilla Glue. The cardboard test piece was adhered with double-sided tape to a piece of acrylic. The slate was adhered to an acrylic base plate with Gorilla glue in a similar manner to the cork, though there is no alternate direction since the material is relatively

flat. The glass test piece was double-sides taped to an acrylic base plate, like the cardboard. The metalized PET had two prepared samples, one with the metalized layer in contact with the pad, and the other with the PET layer in contact with the pad. Both were attached to an acrylic base plate with Elmer's Spray glue. Images of all the test pieces can be found in the appendix. To conduct the test, the force threshold was set to zero while the pad was charging, and the desired length output was set to its maximum value. Since the force threshold was below the shear force of the pad, it remained in place until the test began. The force was then increased at a constant rate until failure occurred and the test data was saved. Due to the range of failure values and the maximum data point limitations of the Data Acquisition System (DAQ) used, the ramp rate was not constant for all tests, but was always constant for a given material. For the monolithic materials, this test method provided a clear peak in the force time history plot, which is the failure point for the material. The reported failure force value is the maximum value in the recorded force data. A link to a drive repository with videos of example tests can be found through the following link, Video Drive Folder . For granular materials, the test procedure had to be modified in order to accurately measure the smaller forces. First, in order to increase the resolution of the machine, the lever arm was doubled in length to halve the applied force for a given torque. Additionally, because of the low failure forces, the force threshold had to be decreased, which, in conjunction with the increased length and mass of the arm, cause the muscle tester to vibrate the arm when it was close to either of its angular displacement limits. This vibration made it difficult for manual or automated data processing for the runs, so a plastic rod was used just before the limit to prevent this adverse reaction. The downside to this, however, is that the force output no longer peaked with the failure force, since the motor was still pushing against this rod. For these test, the length output became critical in determining the failure force. Based on test results from the monolithic materials, the failure point could be expected on the length plot where the material transitions from a stretching behavior to a slipping behavior around a "knee" in the plot. This knee was not easily determined from the maxima of the rate, acceleration, or jerk; however, it seemed to have a consistent lag from the maximum acceleration. This criteria was then used, with an average

centered about the selected point to reduce the effects of noise, which is a much larger factor for these materials. For these materials, the failure point was also plotted on the position curve, for the assessment of whether the criteria was producing the correct point of failure.

4.3 Experimental Results

For the experimental results below, an example of the force and length plots produced from a test are shown, with a red circle highlighting the point of failure.

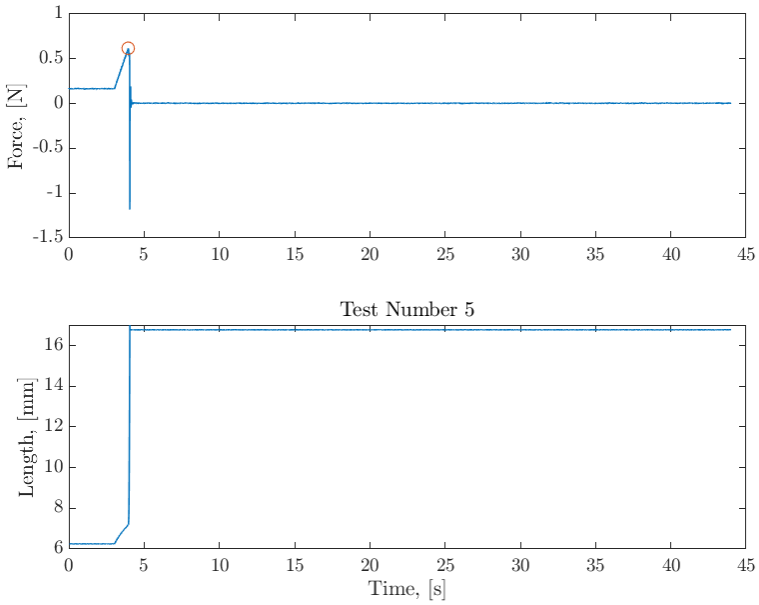

Figure 4.2: Cork shear force and arm position over the course of test 5 for the across ridge pull direction.

[H]

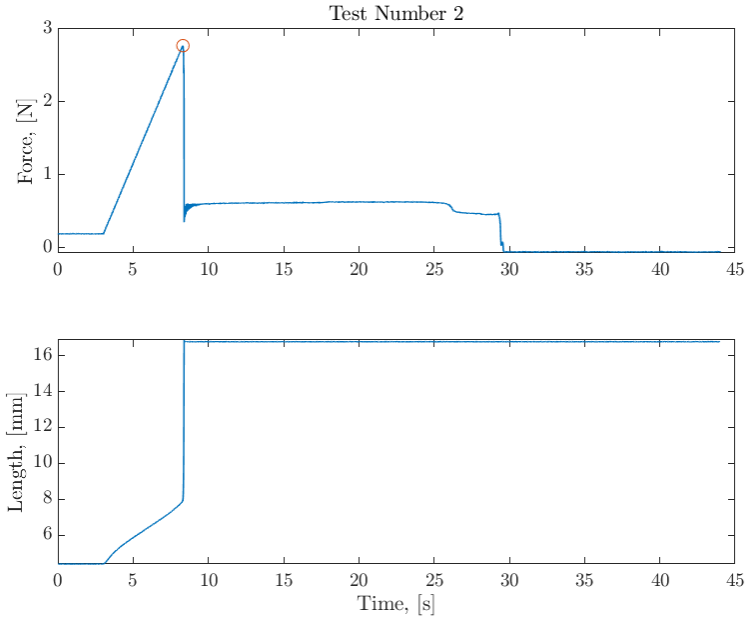

Figure 4.3: PMMA force and position over the course of test 2.

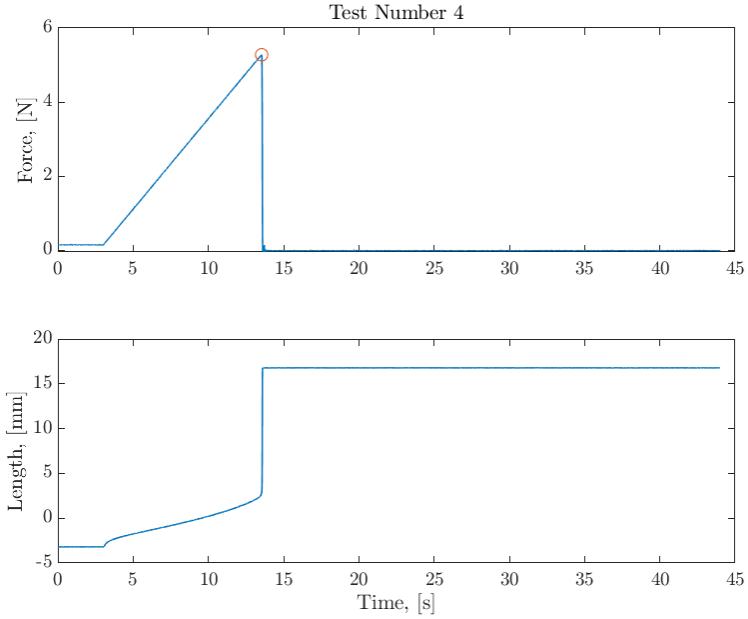

Figure 4.4: Wood shear force and arm position over the course of test 4.

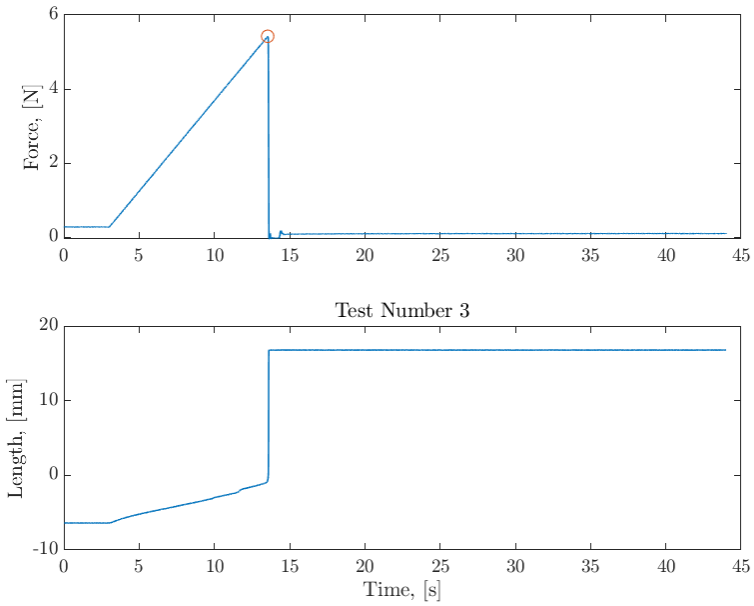

Figure 4.5: Cardboard shear force and arm position over the course of test 3.

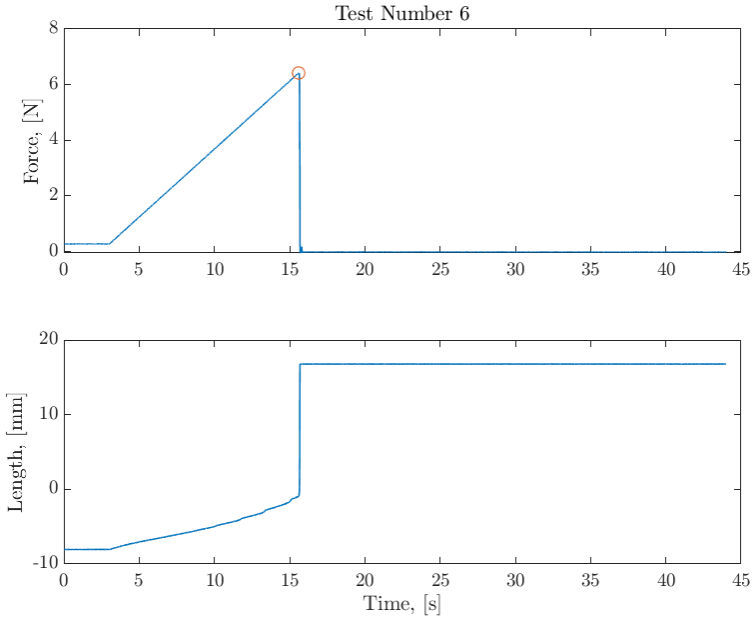

Figure 4.6: Slate shear force and arm position over the course of test 6.

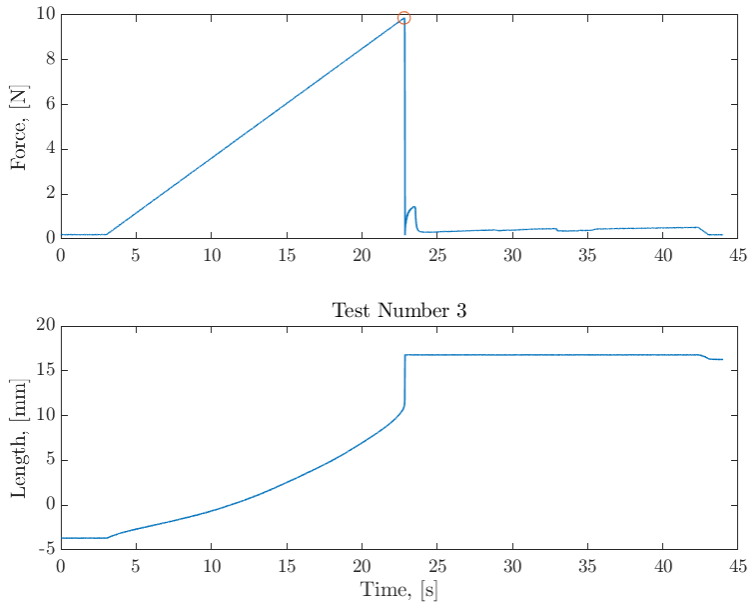

Figure 4.7: Glass shear force and arm position over the course of test 3.

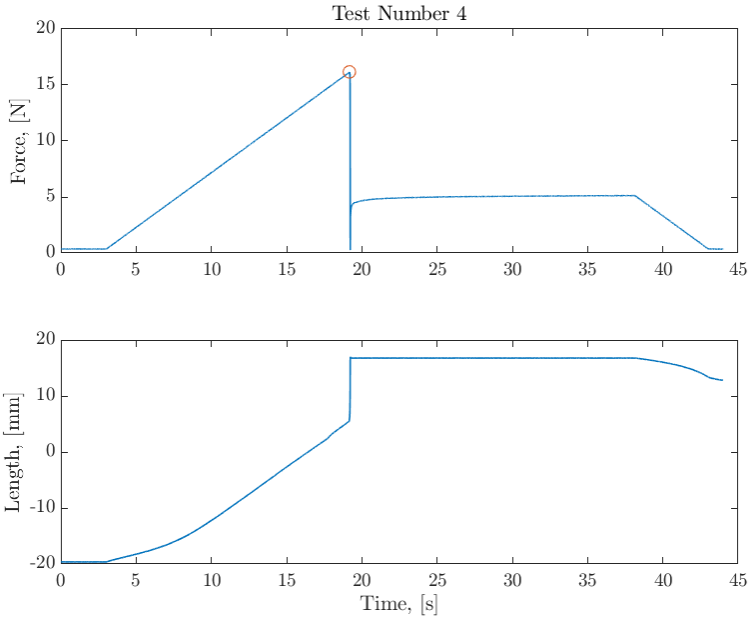

Figure 4.8: Metalized PET applied shear force and arm position over the course of test 4.

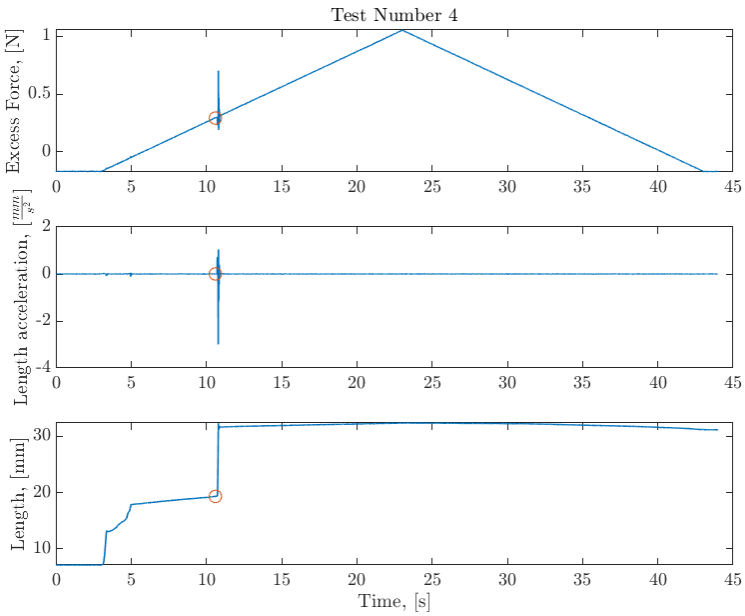

Figure 4.9: Gravel applied shear force and arm position over the course of test 4.

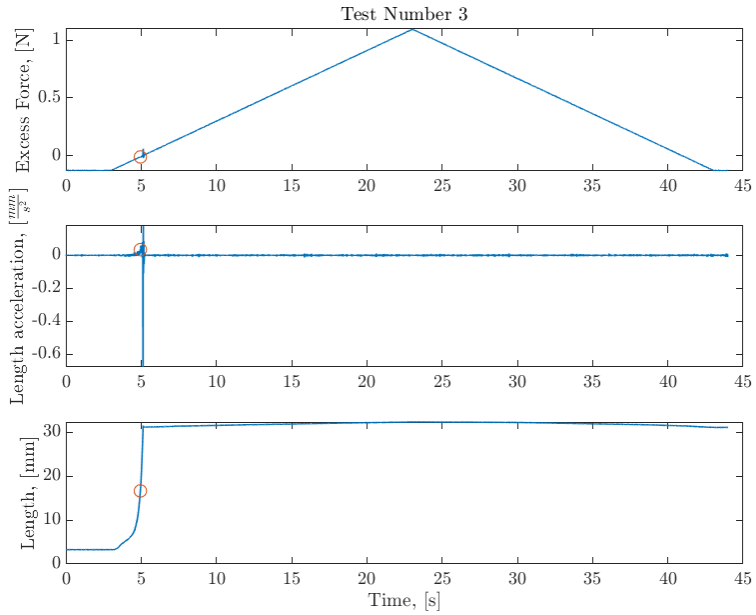

Figure 4.10: Leaf Litter applied shear force and arm position over the course of test 3.

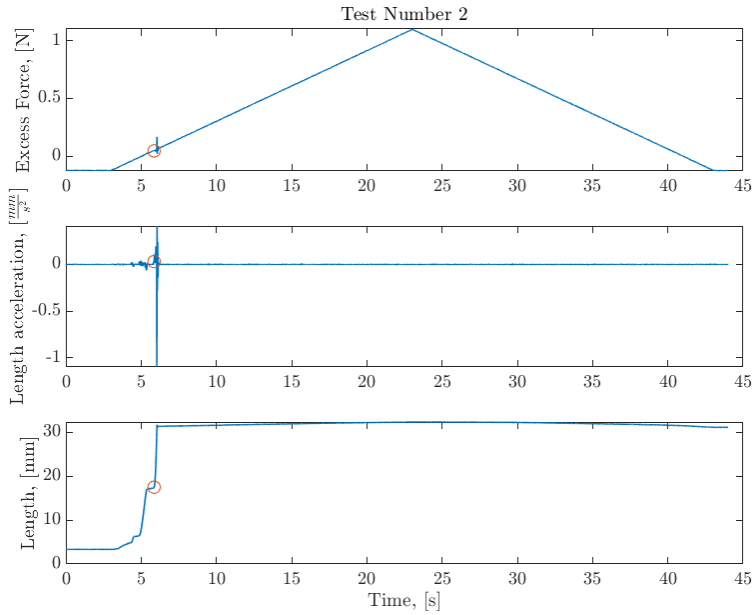

Figure 4.11: Sand applied shear force and arm position over the course of test 4.

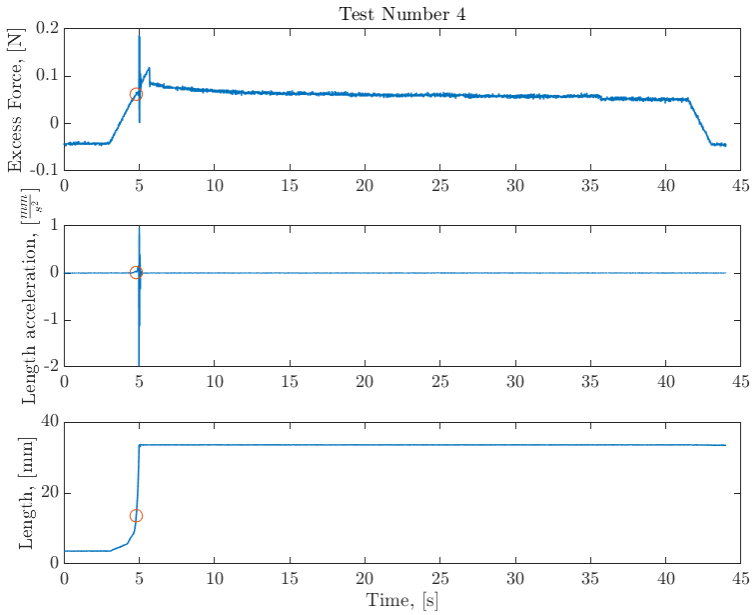

Figure 4.12: Regolith Simulant applied shear force and arm position over the course of test 4.

The results from these individual tests is summarized in the box plots for all monolithic materials in figure 4.13, and for the granular materials in fig. 4.14.

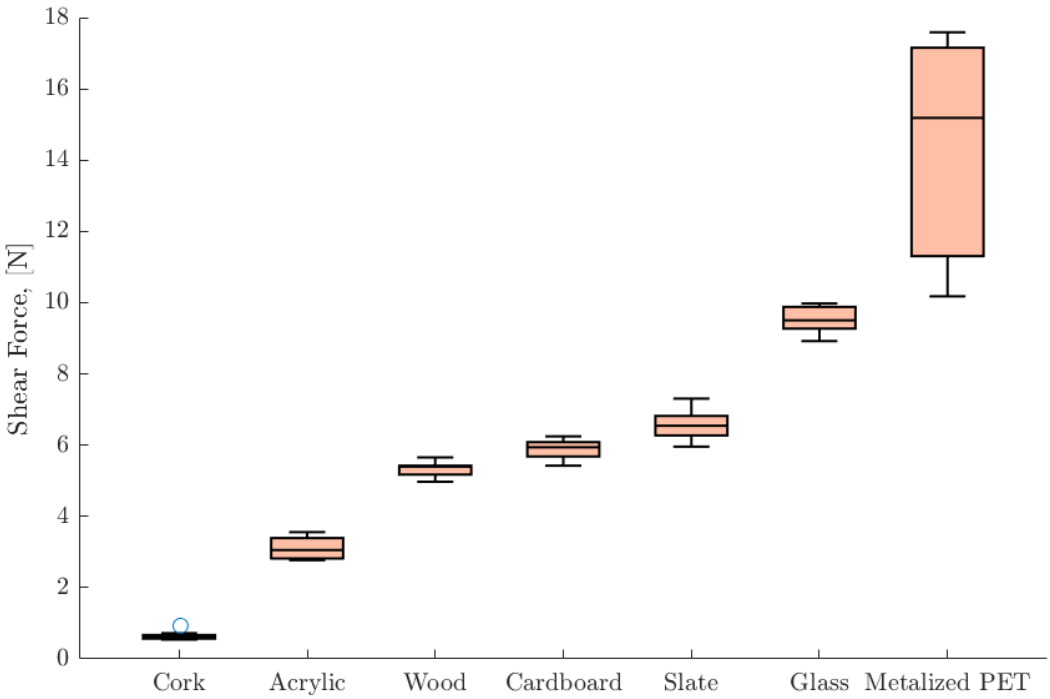

Figure 4.13: Summary plot of the solid materials. Cork is included here since the forces are closer to the other solid materials than to the granular ones.

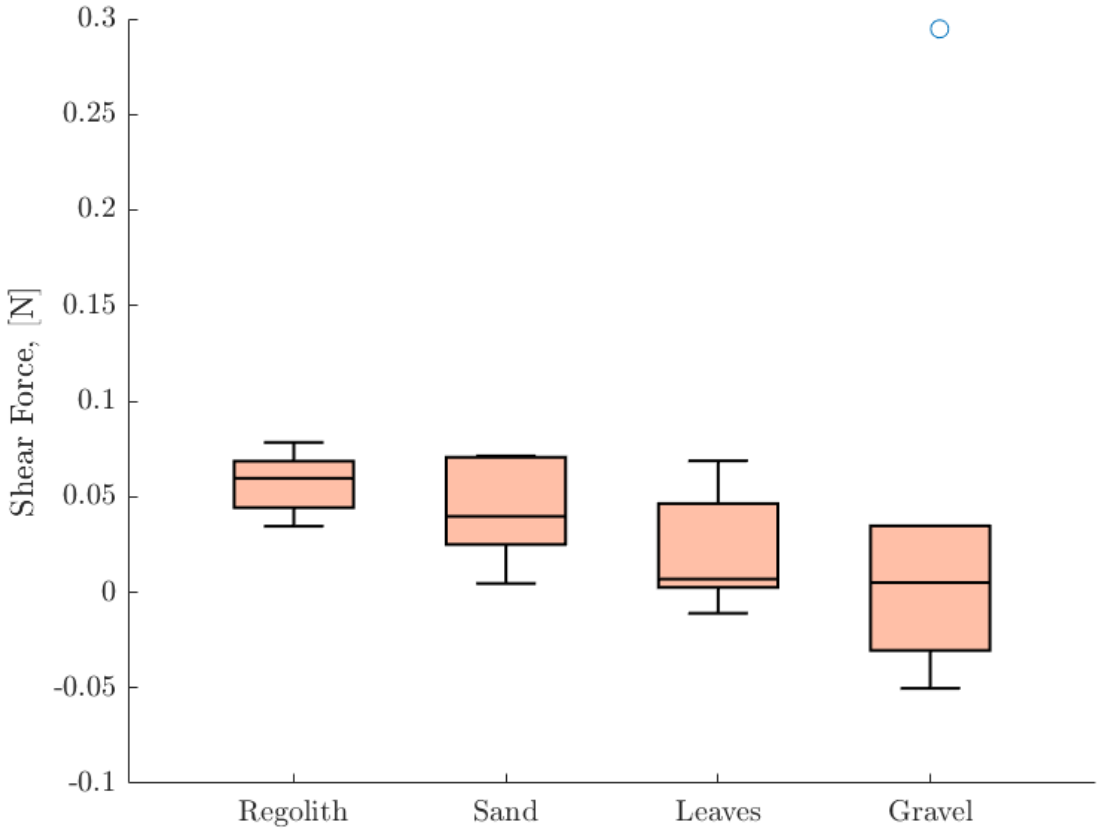

Figure 4.14: Summary plot of the granular materials. Negative forces are relative to the reference tests with no electroadhesion.

For each of the materials, the results in the form of lowest force tested, highest force tested, and mean, are summarized in the table below

Material	Lowest Force	Average Force	Maximum Force
Gravel	-0.050	-0.012	0.011
Leaves	-0.011	0.020	0.069
Sand	0.004	0.042	0.071
Regolith Simulant	0.035	0.058	0.078
Cork Bark	0.54	0.64	0.93
PMMA	2.77	3.10	3.56
Wood	4.97	5.33	5.66
Cardboard	5.43	5.88	6.25
Slate	5.96	6.01	7.31
Glass	8.92	9.51	9.97
Metalized PET	10.18	14.44	17.59

Table 4.1: Below is a list of the high, low, and average value for each material over the tests. Results were generally unsurprising, with conductive materials adhering very well and granular or rough media performing the worst.

4.4 Discussion

The results from the shear tests show three clear categories of materials when it comes to attractive forces. The flat, monolithic materials tested had the highest shear forces in the test, ranging from approximately 3 Newtons for PMMA, to 15 Newtons for metalized PET. The results for all materials of this type can be seen in figure 4.13, which shows the range of forces over 6 tests per material. The wide range in the metalized PET values is potentially due to damage of the pad, as the failure force showed a marked decrease for the last two tests, as compared to the previous four. The granular materials constitute a separate group, with extremely small forces compared to any of the monolithic materials. The results from this group can be seen summarized in the figure 4.14. The highest shear force for this group was the regolith simulant, which, similarly to the strongest material in the monolith materials, is slightly conductive. The other materials all show a

range of forces, all of which are much smaller than the frictional forces of dragging the pad across the material. The randomness in this friction force means more needs to be done to characterize the baseline for these materials before the true effects of electroadhesion can be ascertained.

Chapter 5

Future Work

5.1 Robot Modeling

The work to be done on both models is relatively similar, so the two are evaluated together here. The primary thing to further both models would be the incorporation of robust under actuated control. This would be the start of true soft robotics control design for the project, and would help asses the viability of the crawling mobility proposed for the AoES thus far. Additionally, both models need verification against real data, as currently there are linearity assumptions present in some aspects of the dynamics, which will likely be inaccurate upon comparison to experimental data. Creating a test limb and collecting experimental comparison data will be a necessary next step, as current vales for the spring rate and damping constants at the joints are largely placeholders until the true nonlinear functions for their values are found.

For the Full AoES model, the error that is currently present in the dynamics simulation needs to be found so that the model is completely functional, rather than just somewhat functional depending on the initial condition.

After these models begin to allow the AoES concept to narrow in on a solution for limb shape and control architecture, a more complex model, like the SOFA modeling toolkit [8], should be used to obtain higher accuracy simulation results, as well as capture out of plane effects ignored in the limited model proposed in this work. This more accurate modeling should provide more confidence that the control algorithms will work when tested in low gravity and in unknown terrain.

5.2 Electroadhesion

There are still a number of variables to test before granular electroadhesion can be fully characterized. For these tests, ramp rate was held constant for each material, but due to the large range of failure shear forces, different ramp rates were used for different materials. Running the same material under a range of force rates would help determine if the force ramp rate affects the failure force. In addition to the shear tests performed, it would also be useful to characterize the normal and peel forces of the electroadhesive pad on each material.

While the pads used were thin for conformance to rough materials, this did not provide enough impedance to avoid dielectric failure on highly conductive materials. The pad failed on metalized PET when in direct contact with the metal coating, as well as with ice. Using a thicker base material for the pad would help with improving its dielectric strength, which should allow electroadhesion with these materials to be tested.

Creating pads which optimize the attraction to granular substrates would be interesting to investigate. The current pads show a low degree of attraction to granular materials, so testing if different pad patterns and textures improve this performance.

Creating test pads which mimic those in other electroadhesion characterization work, and testing those pads on the same materials to provide a baseline and level of confidence in the test fixture and procedure would be useful, as well as improving confidence in the forces expected from electroadhesion for practical applications. In addition, the creation and comparison of different pad materials and spacing will help provide additional data for the characterization of how these parameters affect the force output of the pad.

5.3 Conclusion

In conclusion, this work set out to provide a fast model for the prototype design stage of the AoES limb, and begin to characterize granular electroadhesion, which will further inform potential control strategies for the AoES. As shown by the work above, this thesis accomplished these tasks

through the creation of rigid link approximation models for the AoES limb and planar AoES, with simulations of the interactions between the AoES and the surface, along with other external forces. The preliminary stages of electroadhesion were also examined, with a test fixture constructed, test procedure developed, and some data taken for a variety of materials, including four granular ones. With these two contributions, this work should help advance the progress of soft robotic modeling, granular electroadhesion, and the AoES mission concept.

Bibliography

[1] E. Acome, S. K. Mitchell, T. G. Morrissey, M. B. Emmett, C. Benjamin, M. King, M. Radakovitz, and C. Keplinger. Hydraulically amplified self-healing electrostatic actuators with muscle-like performance. Science, 359(6371):61–65, 2018.

[2] Daniel N. Brack. Investigations into the Relationship Between Surface Activity and the Dynamical State of Asteroids. PhD thesis, University of Colorado, 2020. Copyright - Database copyright ProQuest LLC; ProQuest does not claim copyright in the individual underlying works; Last updated - 2020-07-22.

[3] J.C. Butcher. Numerical Methods for Ordinary Differential Equations. Wiley, 2016.

[4] V. Cacucciolo, J. Shintake, and H. Shea. Delicate yet strong: Characterizing the electroadhesion lifting force with a soft gripper. In 2019 2nd IEEE International Conference on Soft Robotics (RoboSoft), pages 108–113, April 2019.

[5] Jean Chenevier, David González, J. Vicente Aguado, Francisco Chinesta, and Elías Cueto. Reduced-order modeling of soft robots. PLOS ONE, 13(2):1–15, 02 2018.

[6] ASTM D 1894-14. Standard test method for static and kinetic coefficients of friction of plastic film and sheeting. Technical report, ASTM International, 2014.

[7] Sébastien D. de Rivaz, Benjamin Goldberg, Neel Doshi, Kaushik Jayaram, Jack Zhou, and Robert J. Wood. Inverted and vertical climbing of a quadrupedal microrobot using electroadhesion. Science Robotics, 3(25), 2018.

[8] Christian Duriez. Control of elastic soft robots based on real-time finite element method. ICRA, 2013.

[9] Francois Faure, Christian Duriez, Herve Delingette, Jeremie Allard, Benjamin Gilles, Stephanie Marchesseau, Hugo Talbot, Hadrien Courtecuisse, Guillaume Bousquet, Igor Peterlik, and Stephane Cotin. Sofa: A multi-model framework for interactive physical simulation. Studies in Mechanobiology, Tissue Engineering and Biomaterials, 2012.

[10] Xing Gao, Chongjing Cao, Jianglong Guo, and Andrew Conn. Elastic electroadhesion with rapid release by integrated resonant vibration. Advanced Materials Technologies, 4(1):1800378, 2019.

[11] M. Géradin and D. Rixen. Mechanical Vibrations: Theory and Application to Structural Dynamics. Wiley, 1997.

[12] J. Germann, B. Schubert, and D. Floreano. Stretchable electroadhesion for soft robots. In 2014 IEEE/RSJ International Conference on Intelligent Robots and Systems, pages 3933–3938, Sep. 2014.

[13] Guoying Gu, Jiang Zou, Ruike Zhao, Xuanhe Zhao, and Xiangyang Zhu. Soft wall-climbing robots. Science Robotics, 3(25), 2018.

[14] J Guo, T Bamber, M Chamberlain, L Justham, and M Jackson. Optimization and experimental verification of coplanar interdigital electroadhesives. Journal of Physics D: Applied Physics, 49(41):415304, sep 2016.

[15] J. Guo, T. Bamber, J. Petzing, L. Justham, and M. Jackson. Experimental study of relationship between interfacial electroadhesive force and applied voltage for different substrate materials. Applied Physics Letters, 110(5):051602, 2017.

[16] J. Guo, J. Leng, and J. Rossiter. Electroadhesion technologies for robotics: A comprehensive review. IEEE Transactions on Robotics, 36(2):313–327, 2020.

[17] Weicheng Huang, Xiaonan Huang, Carmel Majidi, and M. Khalid Jawed. Dynamic simulation of articulated soft robots. Nature Communications, 11(1):2233, May 2020.

[18] Frederick Largilliere, Valerian Verona, Eulalie Coevoet, Mario Sanz-Lopez, Jeremie Dequidt, and Christian Duriez. Real-time control of soft-robots using asynchronous finite element modeling. ICRA, 2015.

[19] Cecilia Laschi, Matteo Cianchetti, Barbara Mazzolai, Laura Margheri, Maurizio Follador, and Paolo Dario. Soft robot arm inspired by the octopus. Advanced Robotics, 26:709–727, 2012.

[20] J. McMahon, S. K. Mitchell, K. Oguri, N. Kellaris, D. Kuettel, C. Keplinger, and B. Bercovici. Area-of-effect softbots (aoes) for asteroid proximity operations. In 2019 IEEE Aerospace Conference, pages 1–16, 2019.

[21] Kenshiro Oguri and Jay W. McMahon. Srp-based orbit control with application to orbit stationkeeping at small bodies. In AAS/AIAA Space Flight Mechanics Meeting. AIAA, 2019.

[22] Jun Shintake, Samuel Rosset, Bryan Schubert, Dario Floreano, and Herbert Shea. Versatile soft grippers with intrinsic electroadhesion based on multifunctional polymer actuators. Advanced Materials, 28(2):231–238, 2016.

[23] J. P. D. Téllez, J. Krahn, and C. Menon. Characterization of electro-adhesives for robotic applications. In 2011 IEEE International Conference on Robotics and Biomimetics, pages 1867–1872, Dec 2011.

[24] Hongqiang Wang, Akio Yamamoto, and Toshiro Higuchi. A crawler climbing robot integrating electroadhesion and electrostatic actuation. International Journal of Advanced Robotic Systems, 11(12):191, 2014.

Appendix A

Electroadhesion Test Plates

Figure A.1: Picture of the test plate for Cork

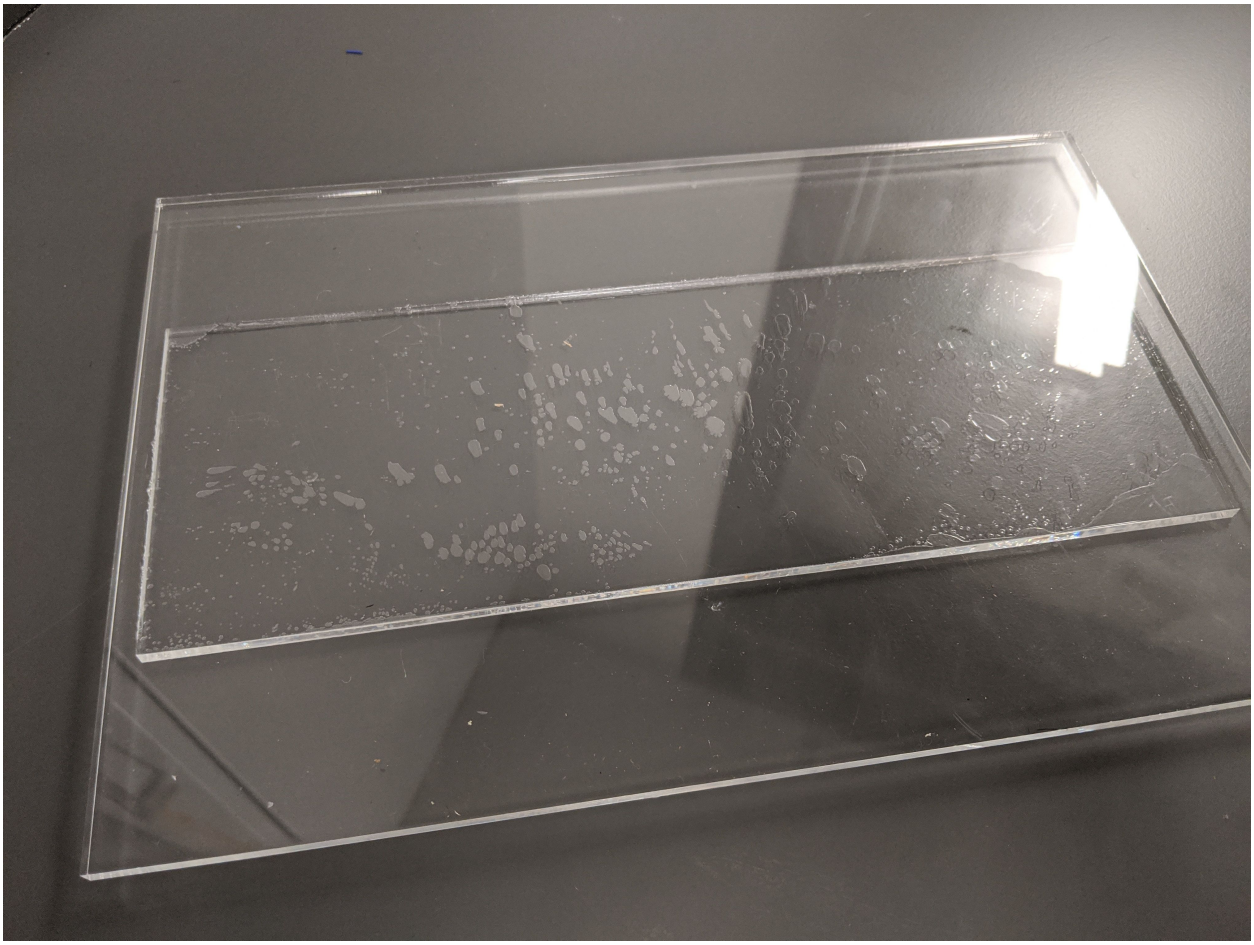

Figure A.2: Picture of the test plate for PMMA

Figure A.3: Picture of the test plate for Wood

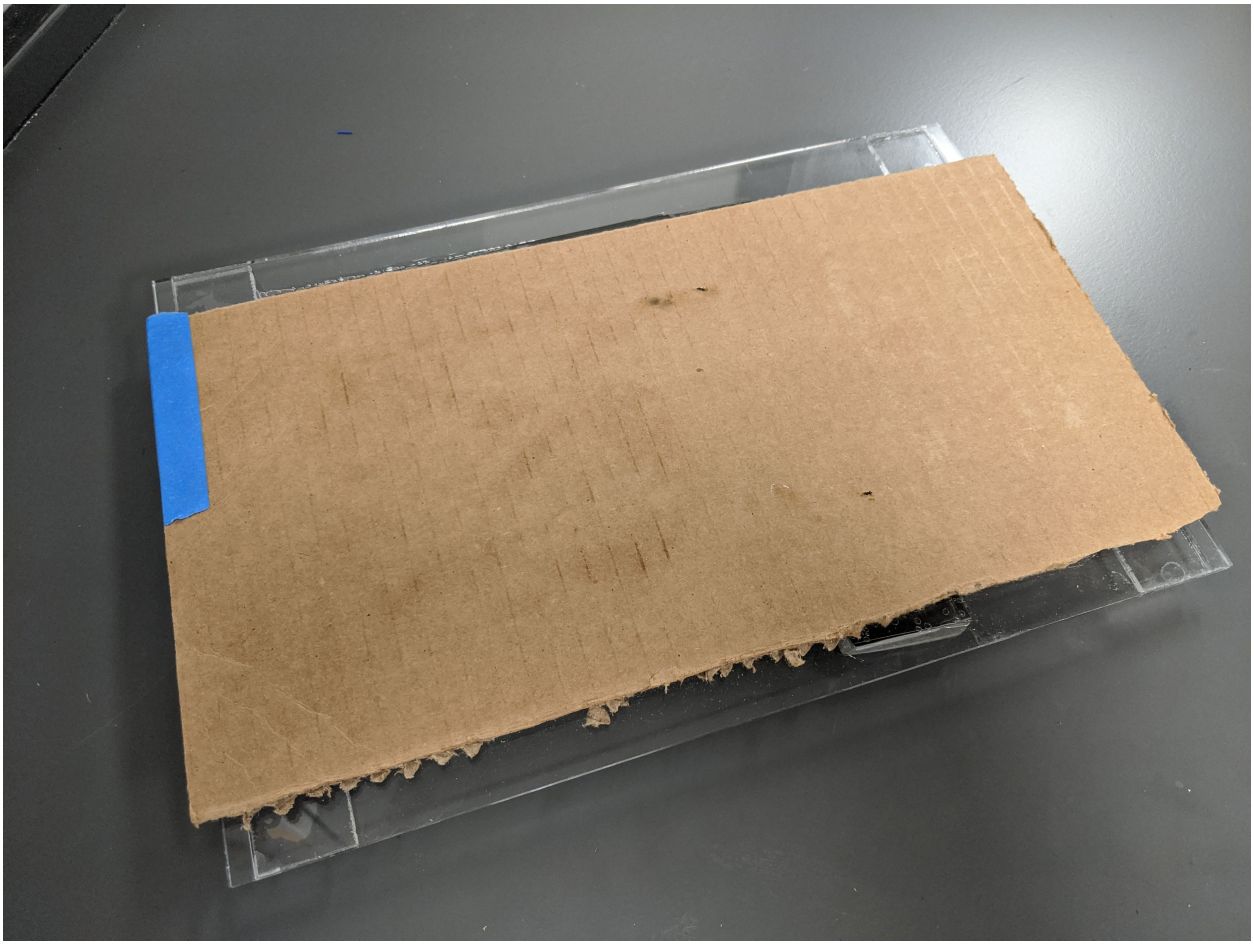

Figure A.4: Picture of the test plate for Cardboard

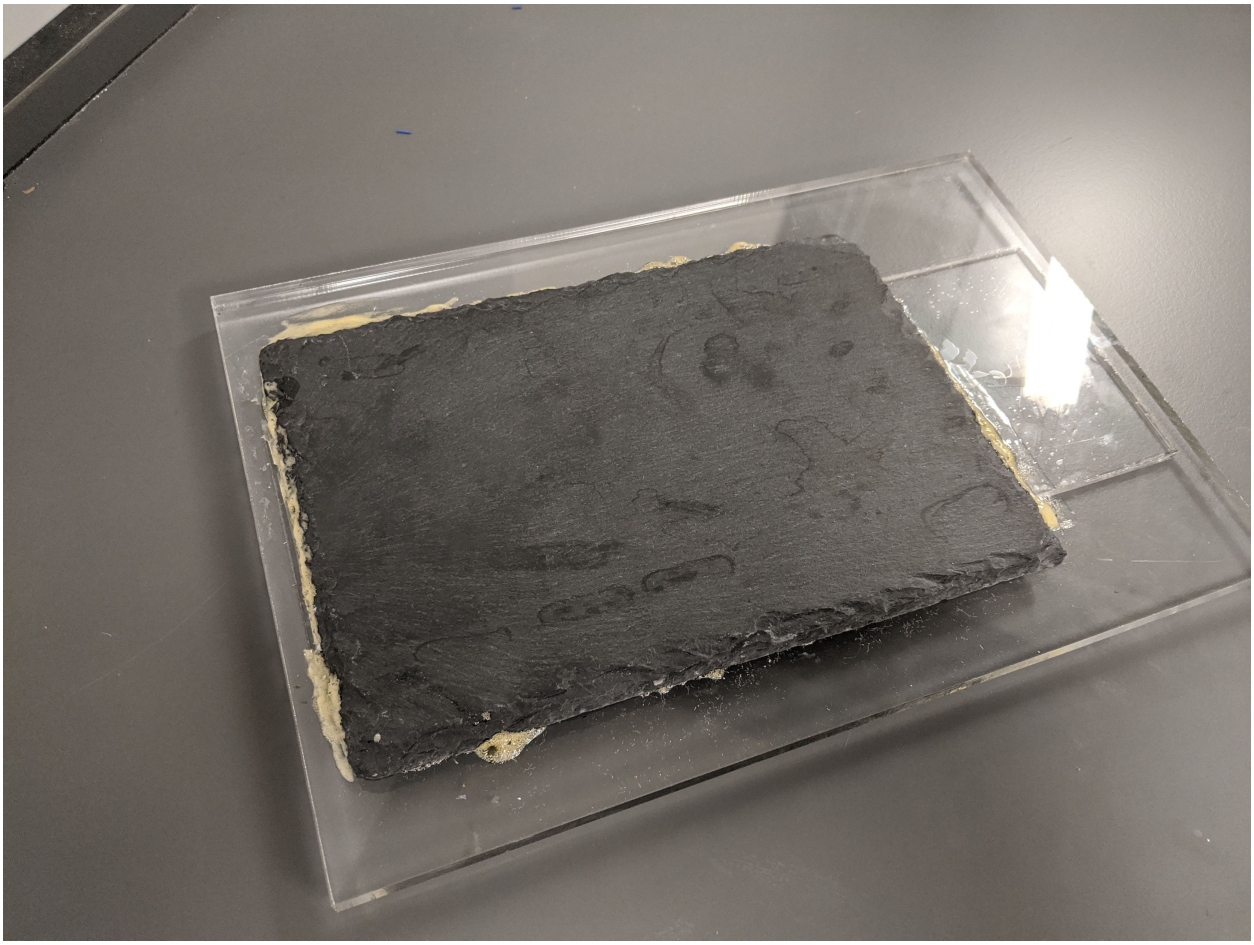

Figure A.5: Picture of the test plate for Slate

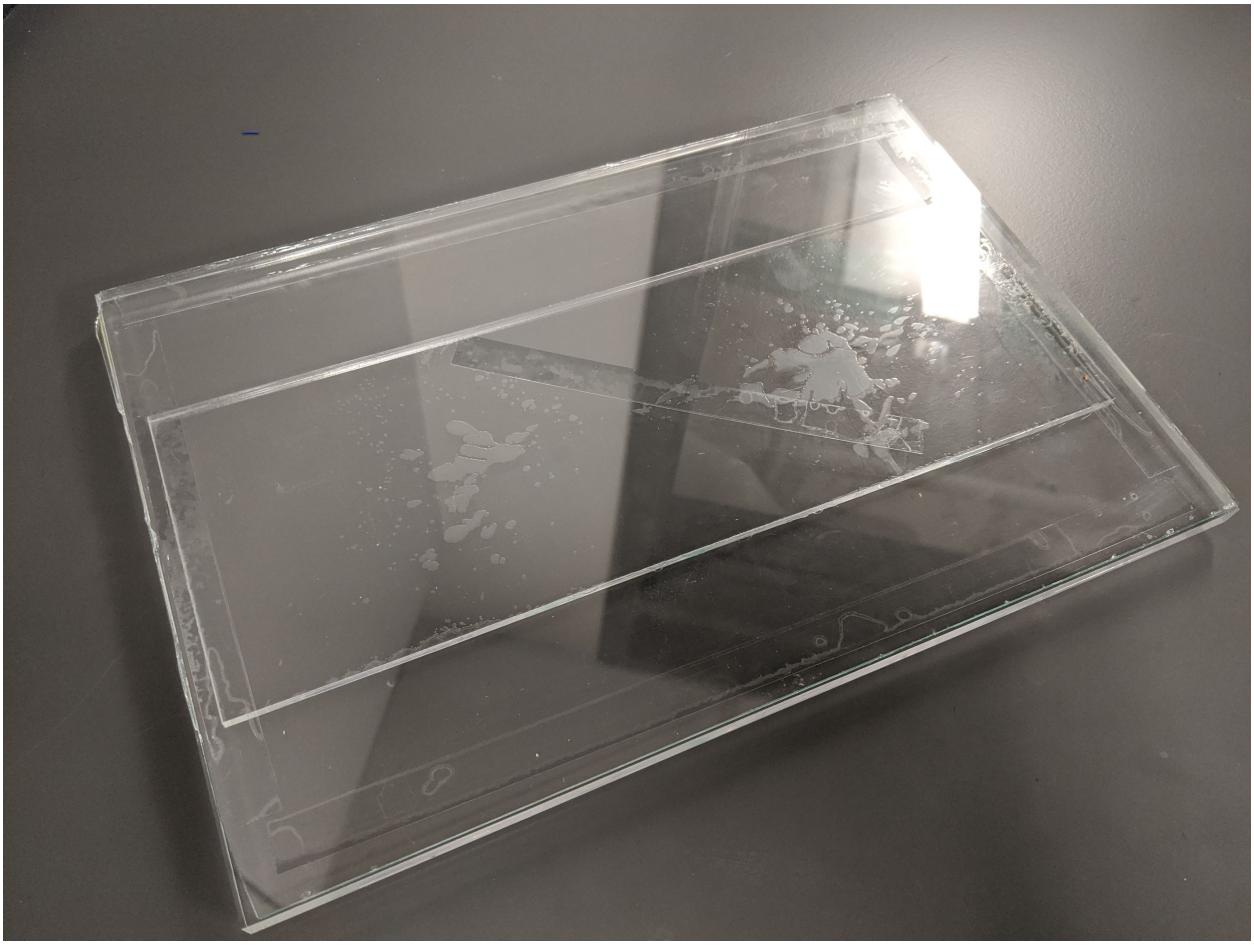

Figure A.6: Picture of the test plate for Glass

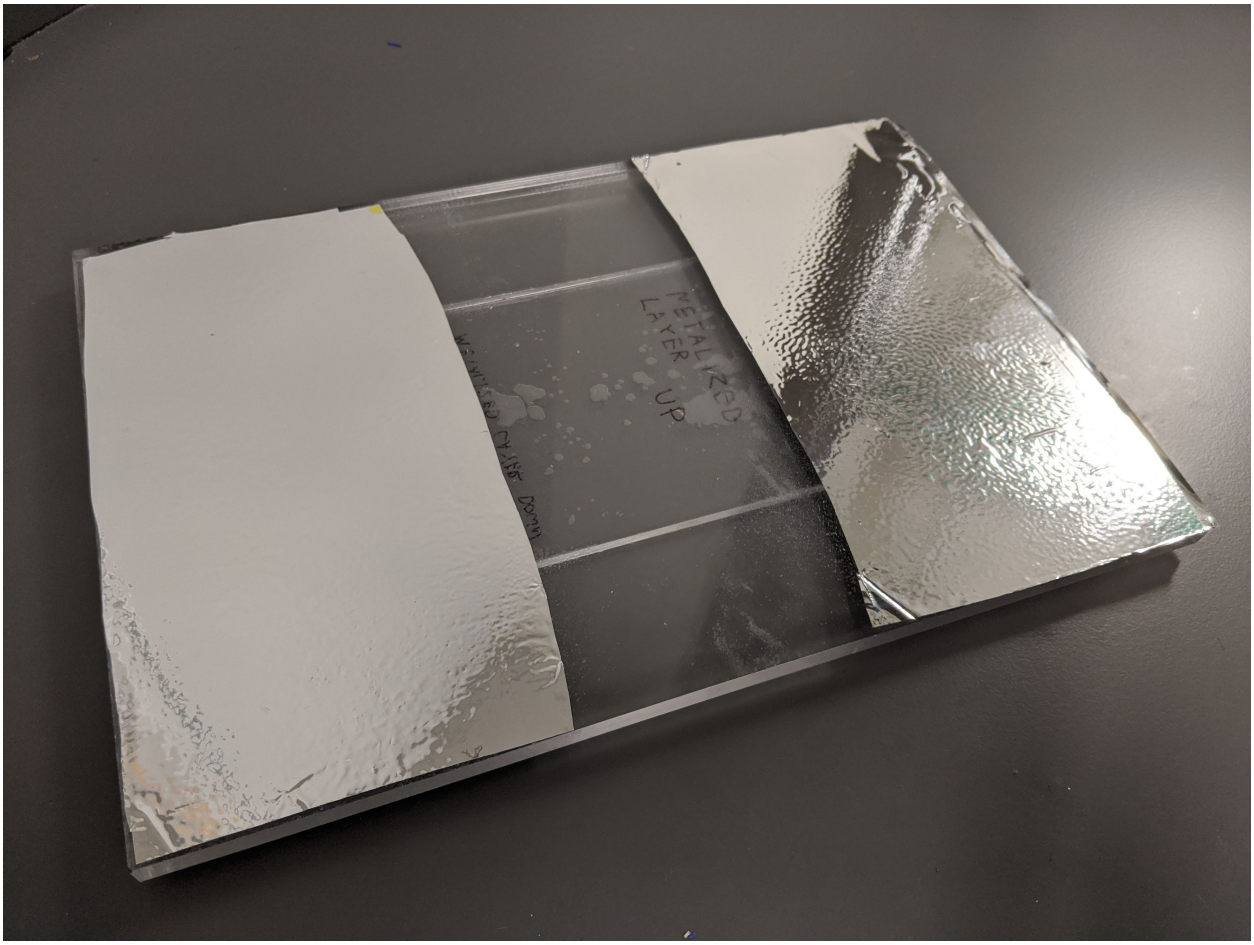

Figure A.7: Picture of the test plate for Metalized PET

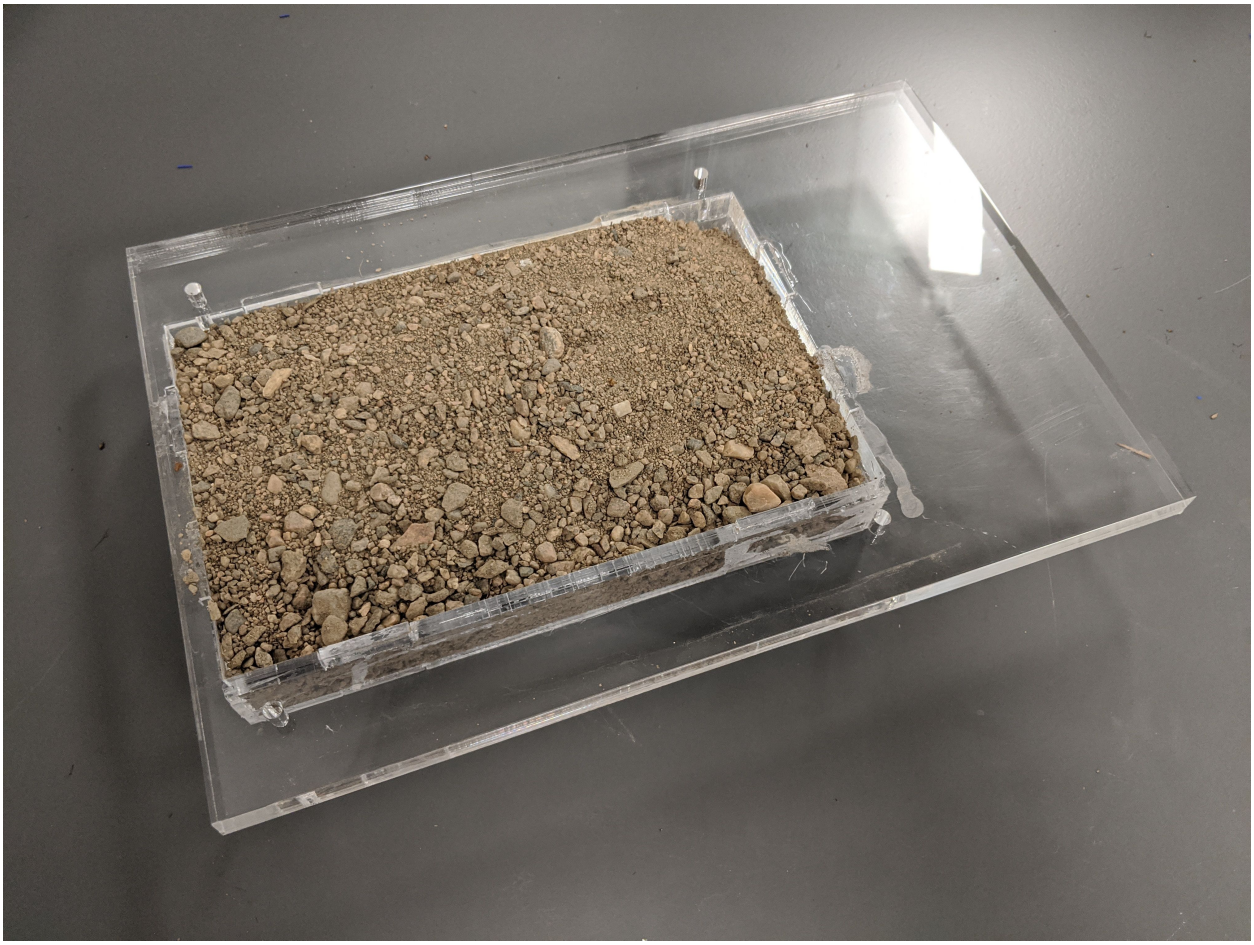

Figure A.8: Picture of the test plate for Sand

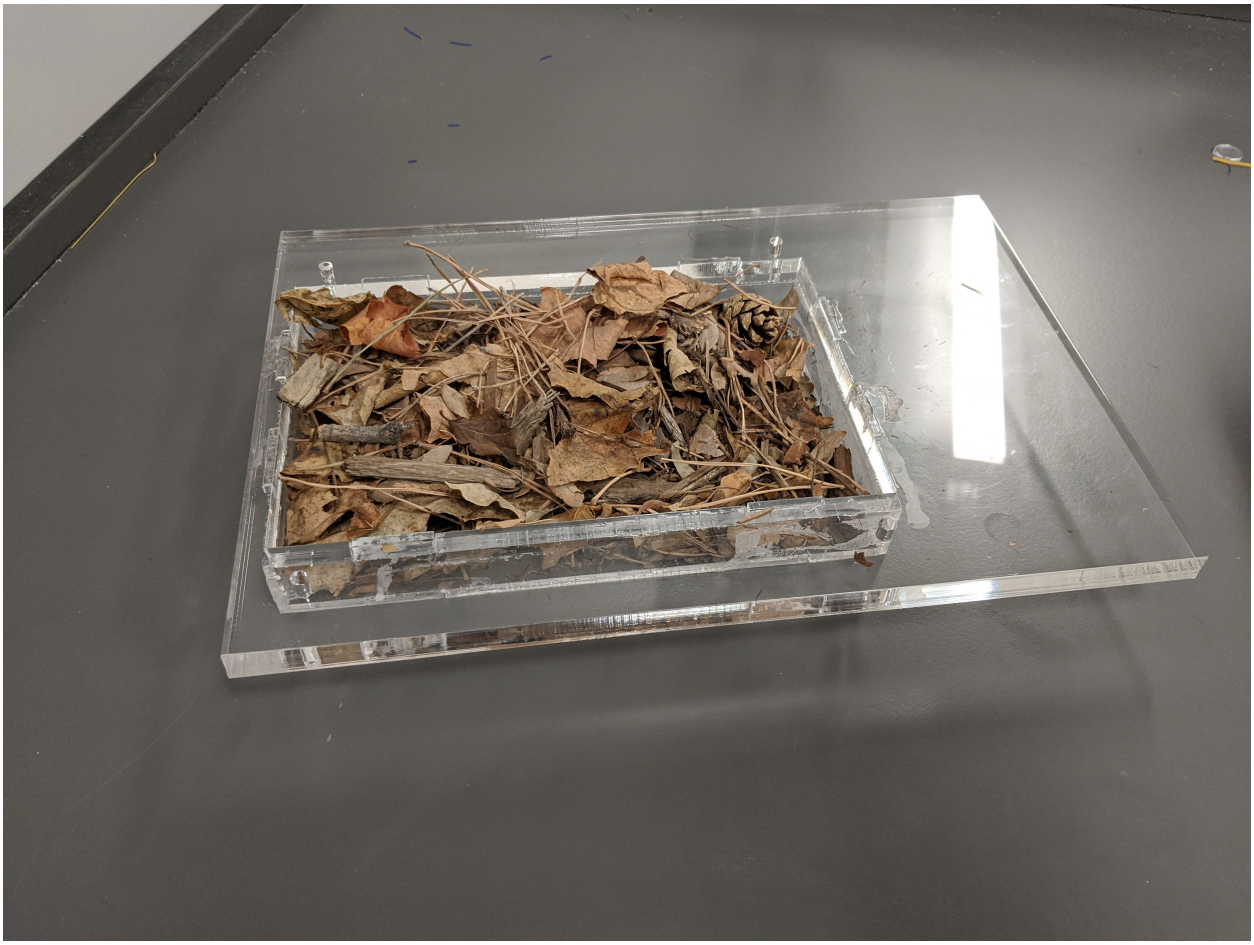

Figure A.9: Picture of the test plate for Leaf Litter